Transmission Electron Microscopy Study of Domains in Ferroelectrics

Queen's University Belfast

Thesis submitted for the degree of
Doctor of Philosophy
in the
Faculty of Engineering and Physical Sciences
by

Kristina Mary Holsgrove MSci (Hons)

School of Mathematics and Physics

Queen's University Belfast

March 2017

Acknowledgments

I would like to sincerely thank my supervisor Dr. Miryam Arredondo who has not only helped and guided me throughout the course of my PhD, but has inspired me with her enthusiasm for science and teaching of TEM. I am very grateful for all of the many collaborations and opportunities to travel that she has given me, all while believing in me and pushing me to achieve my best.

A special thanks to the collaborators who I feel lucky to have carried out TEM experiments with over the past three and a half years: Prof. Quentin Ramasse and Dr. Demie Kepaptsoglou at SuperSTEM (UK), Dr. Eric Prestat and Dr. Sarah Haigh at the University of Manchester (UK) and Dr. Martial Duchamp at ER-C Juelich (Germany). I have learnt so much from all of you, thank you for your time and for making each set of experiments enjoyable! Many thanks also to the collaborators who I have worked with on different aspects of the research analysis, some of you I have yet to meet in person but I thank you all for the many skype calls and email conversations (and speedy replies!): Dr. Sergio Moreno from the Atomic Centre Bariloche (Argentina), Dr. Nicolas Bernier from the University of Grenoble Alpes (France) and Prof. John Huber from the University of Oxford.

I would like to thank others from QUB who have helped me along the way, Prof. Marty Gregg (my second supervisor) and Dr. Amit Kumar (who I like to call my third supervisor). Thank you for the lengthy discussions and help with manuscript drafts, I really appreciate it. Thanks to all the guys in the ferroelectrics group for helpful discussions and a special thanks to Dr. A. Douglas, N. Browne

Abstract

This thesis investigates domain dynamics in one of the most well-known ferroelectric materials – polycrystalline $BaTiO_3$ ceramics, and one of today's most promising ferroelectric materials for future device applications – mixed-phase $BiFeO_3$ thin films. The investigations use primarily TEM techniques accompanied by relevant theory and AFM techniques.

The study on polycrystalline $BaTiO_3$ (FIB lamellae) aims to further understand the link between domains coupling across adjacent grains and to explore the domains' re-ordering as a function of heating through T_C. Two cases were explored: domains coupling across a single grain boundary, and a more complex case of domains within adjacent grains meeting around a junction (or pore). Analysis using martensite crystallography theory demonstrated that domains sharing a single grain boundary do on average arrange themselves in a compatible and stress-free manner. For the example of grains arranged around a junction, a computational example was created, given the complexity of the case. It was demonstrated that the relaxation of the out-of-plane constraint gives rise to an undetermined set of linear equations which can be solved for compatible domain wall orientations and volume fractions of domains, indicating that groups of adjacent grains can form stress-free domain patterns. STEM in-situ heating cycle experiments, heating and cooling through T_C, showed that the re-configuration of the domain structure (domain density, favourable domain orientations and presence of domain bundles) was directly influenced by the rate and continuous/dis-continuous nature of the performed heating cycles.

Furthermore, this material was explored with focus on the functionality of its positive temperature coefficient of resistivity (PTCR) effect. Aberration-corrected STEM and EELS revealed a grain boundary $PbTiO_3$-like region (~10-15 nm), which was associated with an increased local polarisation in that region. The chemical and electronic heterogeneity of the ceramic was linked to the changes in potential barrier at the grain boundary, theorised by the Heywang-Jonker model. It was inferred that the confined $PbTiO_3$ rich grain boundary region would have a higher spontaneous polarisation (than $BaTiO_3$), thus reducing the grain boundary barrier potential further below T_C, augmenting electronic transport and enhancing the magnitude of resistivity jump at T_C, and so justifying the optimised PTCR effect exhibited by this ceramic.

For the study on phase reversibility in $BiFeO_3$ thin films, the native polymorphs, known as T and R, were initially identified. The thermal activation phase transformation was investigated by STEM in-situ heating cycle experiments; showing a lateral growth of the highly-strained T phase above 400°C. Additionally, an AFM tip was used to locally apply electric field and stress, demonstrating reversible switching between the native mixed-phase and a pure T phase state. Energy-based effective Hamiltonian simulations verified phase competition under the application of electric field and stress, comparable to experimental data. The stress-written phase boundaries (R'/T') were investigated via c-AFM showing enhanced conductivity. TEM analysis of cross-sectional lamellae from pre-written AFM regions revealed that the stress-written R' and T' polymorphs differ in structure from the native polymorphs and, the R'/T' boundaries have higher in-plane strain gradients compared to the native R/T boundaries, rationalising the enhanced conductivity as a strain mediated effect.

Publications

The work presented in this thesis has resulted in the following manuscripts for publication:

"Mapping grain boundary heterogeneity at the nanoscale in a positive temperature coefficient of resistivity ceramic"

K. M. Holsgrove, D. M. Kepaptsoglou, A. M. Douglas, Q. M. Ramasse, E. Prestat, S. J. Haigh, M. B. Ward, A. Kumar, J. M. Gregg and M. Arredondo

APL Materials, **2017**, *5*(6), 066105.

"Deterministic reversible control over symmetry states in mixed-phase $BiFO_3$ using electrical bias and uniaxial stress towards piezoresistive applications"

D. Edwards, N. Browne, **K. M. Holsgrove**, A. Naden, S. O. Sayedaghaee, B. Xu, S. Prosandeev, D. Wang, D. Mazumdar, A. Gupta, S.V. Kalinin, M. Arredondo, R. G. P. McQuaid, L. Bellaiche, J. M. Gregg, A. Kumar

(Manuscript in preparation)

"Atomic structure of native and stress-written phases in mixed-phase $BiFO_3$ thin films"

K. M. Holsgrove, M. Duchamp, M.S. Moreno, N. Bernier, N. Browne, D. Mazumdar, J. M. Gregg, A. Kumar, and M. Arredondo

(Manuscript in preparation)

Publications resulting from work not within this thesis:

"Plasmon enhanced fluorescence studies from aligned gold nanorods arrays modified with SiO_2 spacer layers"

S. Damm, S. Fedele, A. Murphy, **K. M. Holsgrove**, M. Arredondo, R. Pollard, J. N. Barry, D. P. Dowling and J. H. Rice

App. Phys. Lett. **2015,** 106(18), 183109

Conference Participation

"Grain Boundary domain dynamics investigated by Transmission Electron Microscopy in modified $BaTiO_3$ displaying PTCR effect"

K. M. Holsgrove, A. M. Douglas, E. Prestat, S. Haigh, A. Kumar, J. M. Gregg, M. Arredondo

IMC 2014, Prague, September 2014

Poster presentation

"Revealing polymorphs and domain evolution in mixed-phase $BiFeO_3$ thin films"

K. M. Holsgrove, M. Duchamp, D. Edwards, D. Mazumdar, J. M. Gregg, A. Kumar, M. Arredondo

CCEM Summer School on Aberration – corrected Electron Microscopy, Hamilton, McMaster University, Hamilton, Canada, June 2015

Poster presentation

"In-situ experiments of Nanostructured materials"

K. M. Holsgrove (on behalf of M. Arredondo)

ESTEEM 2 – European User Meeting

Gothenburg, Sweden, September 2015

Oral presentation (Invited)

"Atomic-scale study of grain boundaries in an optimised BaTiO$_3$-based PTCR ceramic"

K. M. Holsgrove, D. M. Kepaptsoglou, A. M. Douglas, Q. M. Ramasse, E. Prestat, S. Haigh, M. Ward, A. Kumar, J. M. Gregg, M. Arredondo

Domain walls as new 2D functional materials – Theo Murphy Meeting

Milton Keynes, UK, February 2016

Poster presentation

"Atomic-scale study of grain boundaries in an optimised BaTiO$_3$-based PTCR ceramic"

K. M. Holsgrove, D. M. Kepaptsoglou, A. M. Douglas, Q. M. Ramasse, E. Prestat, S. Haigh, M. Ward, A. Kumar, J. M. Gregg, M. Arredondo

QUB Research Poster Competition

Queen's University Belfast, N. Ireland, June 2016

Poster presentation

"A study of polymorph dynamics in mixed-phase BiFeO$_3$ thin films via AFM and in-situ TEM applications of external stimuli"

K. M. Holsgrove, M. Duchamp, N. Browne, D. Edwards, N. Bernier, D. Mazumdar, J. M. Gregg, A. Kumar, M. Arredondo

The 16th European Microscopy Congress, Lyon, France, September 2016

Oral presentation

"Atomic-scale study of grain boundaries in an optimised BaTiO$_3$-based PTCR ceramic"

K. M. Holsgrove, D. M. Kepaptsoglou, A. M. Douglas, Q. M. Ramasse, E. Prestat, S. Haigh, M. Ward, A. Kumar, J. M. Gregg, M. Arredondo

The 16th European Microscopy Congress, Lyon, France, September 2016.

Poster presentation

"A study of polymorph dynamics in mixed-phase BiFeO$_3$ thin films via AFM and in-situ TEM applications of external stimuli"

K. M. Holsgrove, M. Duchamp, N. Browne, D. Edwards, N. Bernier, D. Mazumdar, J. M. Gregg, A. Kumar, M. Arredondo

Materials Research Society, Fall meeting, Boston, USA, November 2016.

Poster presentation

"Mapping Grain Boundary Heterogeneity at the Nanoscale in a PTCR ceramic"

K. M. Holsgrove, D. M. Kepaptsoglou, A. M. Douglas, Q. M. Ramasse, E. Prestat, S. Haigh, M. Ward, A. Kumar, J. M. Gregg, M. Arredondo

Materials Research Society, Fall meeting, Boston, USA, November 2016.

Oral presentation

Courses attended

Royal Microscopical Society: Electron Microscopy Summer School, Leeds University, UK, April 2014

Canadian Centre for Electron Microscopy: Summer School on Aberration-corrected TEM, McMaster University, Canada, June 2015

Awards

- EMS Scholarship for poster presentation at IMC, Prague (September 2014)
- A place on the CCEM Electron Microscopy Summer School, places were limited to 15 participants world-wide and awarded based on individual essay-based applications (June 2015)
- IOP CR Barber Trust grant for oral and poster presentation at MRS Fall, Boston, USA (November 2016)
- Best Poster Award Nominee at MRS Fall, Boston, USA (November 2016)
- Post-graduate certificate in Innovation and Entrepreneurship from Trinity College Dublin, University College Dublin & Queen's University Belfast (June 2016)

Table of Contents

1. Introduction

1.1 Thesis motivation & overview

Ferroelectrics are both intriguing and intricate materials to study for their technological relevance. The presence of ferroelectricity was first discovered in Rochelle salt by J. Valasek in 1920 [1], but it was not until the 1940s that ferroelectric research began to flourish with the discovery of one of the most well-known ferroelectrics: Barium Titanate ($BaTiO_3$). Since then, ferroelectrics have been discovered and fabricated in many forms, ranging from solid solution ceramics to thin films of nanometre thicknesses. Ferroelectric materials, particularly polycrystalline ceramics, have attracted and been considerably implemented in electronic applications such as high dielectric capacitors, piezoelectric transducers and actuators. Progress in ferroelectric memories and data storage however, still has considerable room for growth to catch up with analogous ferromagnetic materials which are currently widely manufactured for

digital information storage devices. Current research in ferroelectrics for data storage relies on the configuration and manipulation of domains with an even more recent novelty regarding domain wall functionalities, in which the interfaces between domains could act as an active component of the device; some recent exciting discoveries include domain wall conductivity [2]. To fully exploit the potential of ferroelectrics for data storage applications, a deeper understanding of domain configurations and dynamics with applied external stimuli is necessary. In light of this, this thesis presents a study of domains in one of the most technologically used ferroelectric materials: polycrystalline $BaTiO_3$, and one of today's most promising ferroelectrics for device applications: mixed-phase $BiFeO_3$ thin films. The investigations primarily use transmission electron microscopy (TEM) techniques accompanied by relevant theory and atomic force microscopy (AFM) techniques.

In this chapter some concepts relevant to ferroelectric materials are discussed. Following this, Chapter 2 covers an overview of TEM including different imaging modes and spectroscopy techniques, as well as the sample preparation methods utilised in this thesis. Additional techniques such as AFM are briefly described. Chapters 3 and 4 describe the experimental investigations carried out on a $BaTiO_3$-based ceramic with emphasis on the coupling of domains across grain boundaries and the reconfiguration of domains during heat cycling (Chapter 3), and an investigation into how chemical heterogeneity and spontaneous polarisation affects the ceramic functionality (Chapter 4). In Chapter 5 mixed-phase $BiFeO_3$ thin films are investigated, exploring phase reversibility by application of external stimuli and characterisation of the $BiFeO_3$ polymorphs

before and after switching. The research presented in this thesis is summarised in Chapter 6 and additional ideas for future work are suggested.

1.2 Definition and properties of ferroelectrics

Ferroelectrics are materials that possess a spontaneous polarisation (or net dipole moment) in the absence of an applied electric field. The spontaneous polarisation can be reoriented (or 'switched') between (at least) two energetically degenerate states by the application of a sufficiently large electric field, which creates a typical ferroelectric hysteresis loop schematically displayed in Figure 1.1. The *polarisation* subject to *electric* field cycling (*P-E* hysteresis) is generally thought to be indicative of ferroelectricity, and bears a likeness to the magnetisation hysteresis (*M-H* hysteresis) which is characteristic of ferromagnetic materials.

If a positive electric field is applied to an un-poled ferroelectric the dipoles begin to align parallel to the electric field (see central region of Figure 1.1) until they become fully aligned and the polarisation is largely saturated ($+P_{sat}$). The extrapolation of this linear section to the polarisation axis (at *E*=0) denotes the value of the spontaneous polarisation (P_s). On decreasing the strength of the electric field, dipoles begin to back-switch to the opposite direction, however, the polarisation will not return to zero because some dipoles will remain aligned in the positive direction and the ferroelectric material will exhibit a remnant polarisation (P_r). When the electric field is reversed, the polarisation eventually becomes negatively saturated ($-P_{sat}$) with the dipoles fully aligned in the opposite direction. The turning point at which the polarisation is reduced to zero occurs at
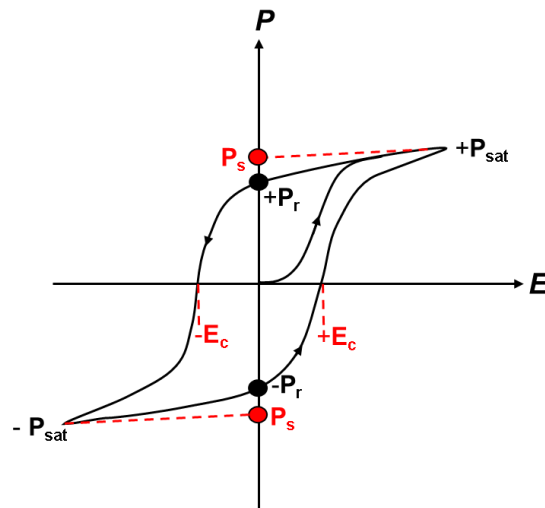
Figure 1.1: Schematic of a typical hysteresis loop measuring polarisation (*P)* whilst cycling electric-field (*E)*. The remnant polarisation (P_r), spontaneous polarisation (P_s), saturation polarisation (P_{sat}) and the coercive field (E_c) are labelled.

a value of applied electric field known as the coercive field (E_c). The ferroelectric hysteresis loop (Figure 1.1) demonstrates the ability of a ferroelectric to be switched from one state to another, forming the basis for ferroelectric non-volatile memory devices. Although indicative of ferroelectricity, caution is required when interpreting hysteresis loops as J. F. Scott pointed out that "a (distinctly non-ferroelectric) banana skin demonstrates a cigar-shaped hysteresis loop which could be mistaken for a ferroelectric hysteresis loop" [3]. Similar *P-E* loops have been misidentified when measuring materials exhibiting lossy (i.e. partially conductive) dielectric behaviour using a capacitor test-geometry.

For a material to be ferroelectric, it must firstly be crystalline and belong to a non-centrosymmetric crystal class (of which there are 21 crystallographic point groups) otherwise a net-dipole-moment cannot exist. Of the 21 non-centrosymmetric point groups, 20 of these exhibit 'piezoelectric' properties

(meaning they develop a polarisation with applied strain). Within the piezoelectrics, there are 10 point groups (1, 2, m, mm2, 3, 3m, 4, 4mm, 6, 6mm) which are polar (i.e. there is at least one direction along which no point group symmetry element forces both sides of the crystal to be the same [4]). These 10 polar point groups are also known as 'pyroelectric' meaning that they develop a spontaneous polarisation in response to a temperature change. Only if the spontaneous polarisation can be reversed by an electric field (as demonstrated in Figure 1.1) can a pyroelectric crystal be deemed as a 'ferroelectric'. Hence, ferroelectrics can be defined as a subset of pyroelectric crystals which exhibit reversible polarisation when subject to electric field cycling (P-E hysteresis). It is important to note that the temperature at which the ferroelectric material transitions from a non-ferroelectric (paraelectric) phase into a ferroelectric phase is known as the 'Curie temperature', denoted T_c. The classification of the crystallographic point groups capable of displaying ferroelectricity are summarised in Figure 1.2.
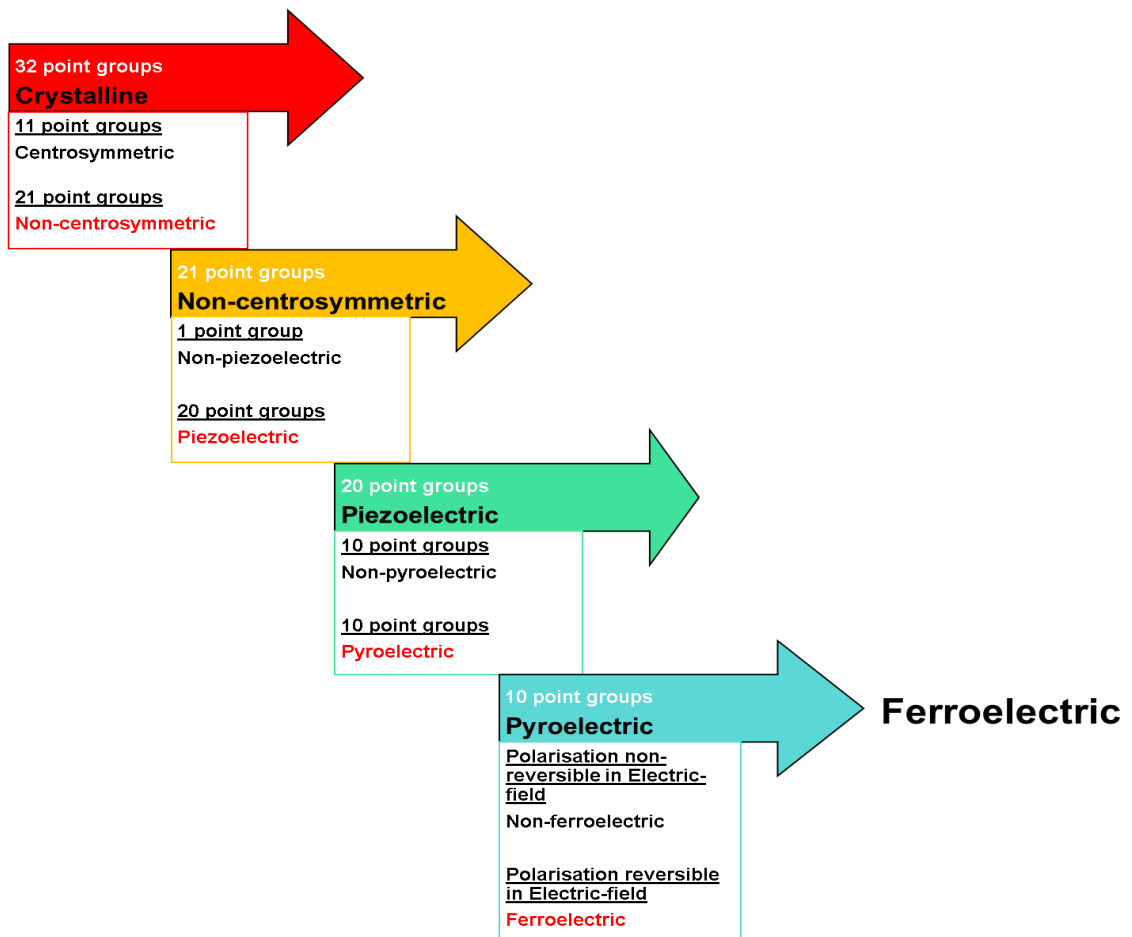
Figure 1.2: Classification by electric properties of the 32 crystalline point groups and their relationship leading to ferroelectricity.

1.3 Perovskite ferroelectrics

Several ferroelectrics including the two materials studied in this thesis ($BaTiO_3$ and $BiFeO_3$) belong to the perovskite family of oxides which have an ABO_3 structure, it is therefore vital to understand how polarisation is manifested in
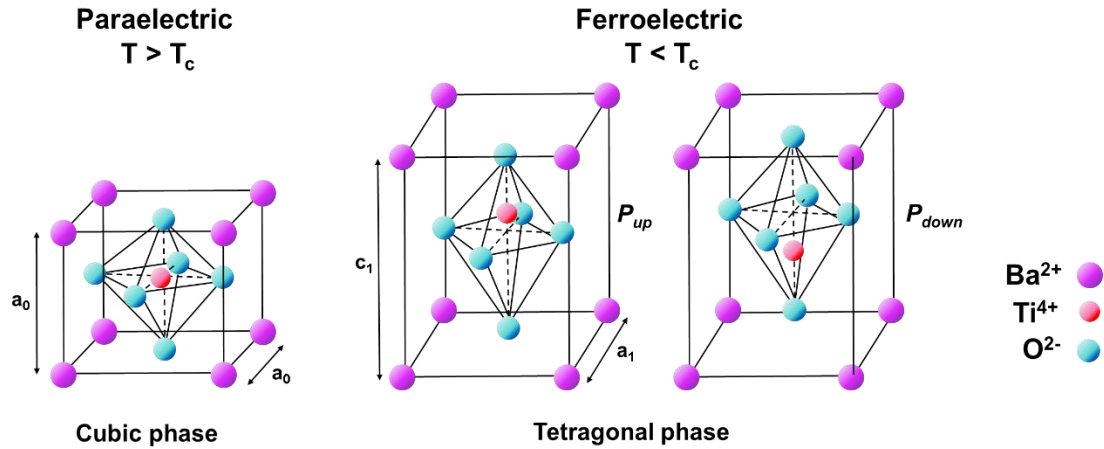
Figure 1.3: Perovskite structure ABO_3 displaying the high-temperature cubic and the low-temperature tetragonal ferroelectric phase in $BaTiO_3$ (tetragonality exaggerated). The direction of the net spontaneous polarisation in the tetragonal phase is denoted by the labels 'P_{up}' and 'P_{down}'. The in-plane (a_0 and a_1) and out-of-plane (a_0 and c_1) are labelled for the cubic and tetragonal unit cells respectively. Adapted from [5].

these crystals. The perovskite structure of $BaTiO_3$ (barium titanate) is shown in Figure 1.3, the paraelectric phase (above T_c) shows a centrosymmetric cubic m3m (point group symmetry) structure, this structure cannot support a net dipole moment due to the inversion centre of the unit cell and therefore shows no sign of ferroelectricity. When $BaTiO_3$ is cooled below T_c (~120 °C) the symmetry of the unit cell is reduced to a tetragonal 4mm structure and there are two energetically degenerate off-centre positions for the central Ti^{4+} cation (labelled as P_{up} and P_{down} in Figure 1.3). This is the origin of the net dipole moment i.e. spontaneous polarisation which is oriented along the polar c-axis. On cooling through T_c into the ferroelectric phase, the $BaTiO_3$ unit cell is spontaneously strained due to the structural transformation between crystal classes. This is illustrated in Figure 1.3

where the tetragonal polar axis length, labelled 'c_1', is larger than the two equivalent a-axes lengths, labelled 'a_1' and 'a_0' in the tetragonal and cubic phases respectively.

As the temperature is reduced even further in $BaTiO_3$ more phase transitions occur; the unit cell structure changes to orthorhombic and then to rhombohedral. With each change in structure the polar direction changes as displayed in Figure 1.4. In the tetragonal phase the polar direction is along the $[001]_{pseudocubic\ (pc)}$ direction, i.e. the displacement of the Ti^{4+} cation is along this direction. Similar to this, the polar direction for the orthorhombic phase is along $[011]_{pc}$ and for the rhombohedral phase it is along the $[111]_{pc}$ direction. In the first half of this thesis studies are carried out on room-temperature tetragonal $BaTiO_3$, with an additional study focusing on cycling between the paraelectric-ferroelectric phases (cubic-tetragonal), therefore the tetragonal polar directions are of particular interest (illustrated in Figure 1.4). The three principal tetragonal axes display the six energetically equivalent polar directions where the central Ti^{4+} cation can be displaced [6]. It is worth noting that an alternative model has been proposed which suggests that the spontaneous polarisation is not simply due to a displacement of the Ti^{4+} cation along one of the polar directions. Instead, it has been suggested that a time-averaging of spontaneous displacements along the <111> corner directions provides a measure of polarisation in the [001] direction for the tetragonal phase [7, 8]. In a similar manner, in the high temperature cubic phase, the Ti^{4+} cation moves rapidly between all eight corners such that the time-averaged polarisation is zero in this model [9-11].
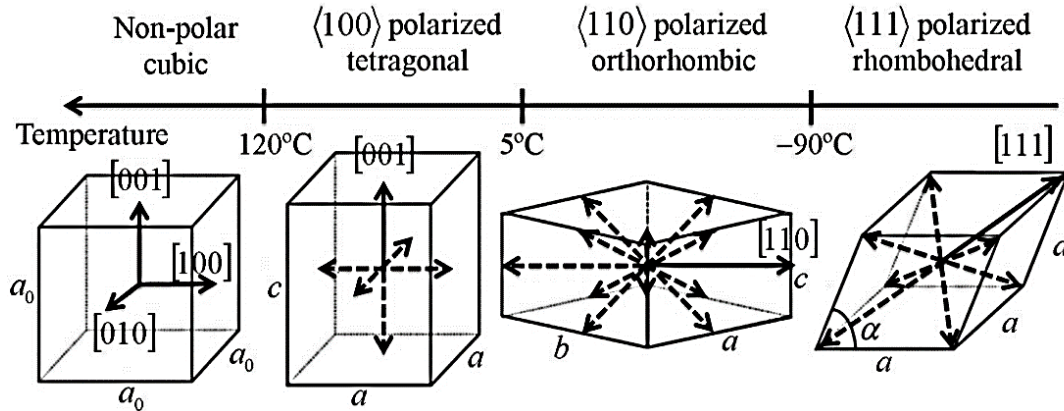
Figure 1.4: The polar directions for the (left-to-right) cubic, tetragonal, orthorhombic and rhombohedral unit cells of BaTiO₃. From [12].

As a convention, a useful measure of the crystal distortion in tetragonal unit cells is the tetragonality, which is described as the percentage ratio of lattice parameters c and a; for the example of tetragonal BaTiO₃ where a = 3.99Å and c = 4.04Å (shown in Figure 1.5), the c/a = 1%. Lead titanate (PbTiO₃) possessed the largest known tetragonality of 6% until recent years, when research began to flourish on epitaxially strained BiFeO₃ thin-films displaying an enormous tetragonality of up to 27% within its tetragonal phase. BiFeO₃ thin-films will be discussed in more detail in Chapter 5 of this thesis.
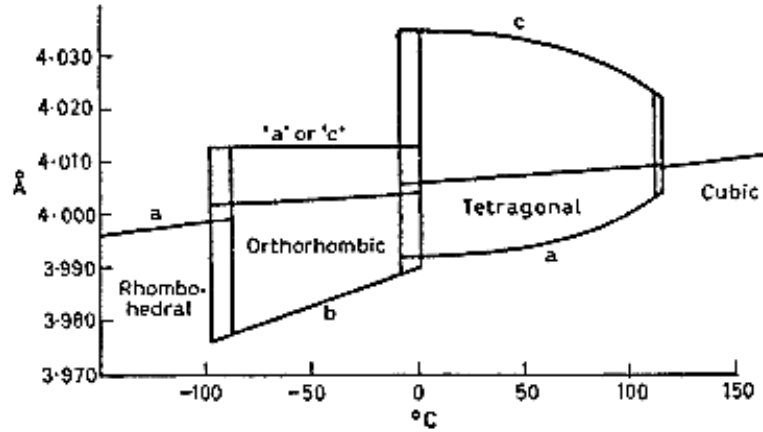
Figure 1.5: Lattice parameters for the different phases of BaTiO$_3$. Labels a, b and c correspond to the respective unit cell axes. From [13].

1.4 Phase transitions in Ferroelectrics

To understand the conditions in which a high-symmetry paraelectric to low-symmetry ferroelectric phase transition takes place, it is of high importance to consult the associated thermodynamics of Landau theory [14-16] which was later applied to BaTiO$_3$ by Devonshire [17, 18]. Landau proposed that the excess free energy due to a phase transition can be described as a polynomial expansion of the order parameter Q, given by [19]:

$$F(Q) = aQ + \frac{1}{2}AQ^2 + \frac{1}{3}bQ^3 + \frac{1}{4}BQ^4 + \cdots \qquad (1.1)$$

If we consider the free energy of a ferroelectric crystal where the order parameter is polarisation (P), and expanding in Taylor series, we obtain:

$$F(P) = \frac{1}{2}AP^2 + \frac{1}{4}BP^4 + \frac{1}{6}CP^6 + \cdots \qquad (1.2)$$

where odd-order terms have been excluded. The free energy of ferroelectrics is an even function of polarisation (because it does not depend on the sign of polarisation) without any exception, if there is no external force acting on the crystal [20]. The equilibrium behaviour of the polarisation through the phase transition is determined by minimising the free energy $F(P)$ with respect to polarisation P, and therefore [19, 21]:

$$\frac{dF(P)}{dP} = 0 \qquad \text{and} \qquad \frac{d^2F(P)}{dP^2} > 0$$

In the high symmetry paraelectric state which is stable above T_c, the polarisation equals zero and the equilibrium conditions above can only be satisfied if A (in Equation 1.2) is positive. If A is negative, the polarisation must be larger than zero and the low temperature ferroelectric state becomes stable. Therefore, the sign of A must change from positive to negative at a temperature $T=T_0$. This temperature dependence of A describes the 'Curie-Weiss' behaviour expressed linearly as a function of temperature, where T_0 is the so-called 'Curie-Weiss' temperature [16]:

$$A = \alpha(T - T_0) \tag{1.3}$$

Inserting Equation 1.3 into the free energy expansion yields:

$$F(P) = \frac{1}{2}\alpha(T - T_0)P^2 + \frac{1}{4}BP^4 + \frac{1}{6}CP^6 + \cdots \tag{1.4}$$

Since α and C are positive for ferroelectrics [16], the sign of B determines the 'order' of phase transition which occurs when transitioning from the paraelectric state through T_c, to the ferroelectric state. A phase transition can either demonstrate a continuous (2nd order) or discontinuous (1st-order) development of polarisation when transitioning through T_c. Furthermore, an expression for the

electric field can be obtained from Landau theory, considering an electric field E is applied parallel to P, and finding the energy minimum, it follows that [20, 21]:

$$\frac{dF(P)}{dP} = E \tag{1.5}$$

By differentiating the free energy expansion in Equation 1.4 we obtain an expression for the electric field in terms of polarisation:

$$E = \alpha(T - T_0)P + BP^3 + CP^5 \tag{1.6}$$

The electric susceptibility (χ) indicates the degree of polarisation of a dielectric material in response to an applied electric field, and is defined by [16]:

$$\chi = \lim_{E \to 0} \left[\frac{dP}{dE}\right] \tag{1.7}$$

Applying Equation 1.7 to Equation 1.6 and neglecting the fifth-order term since it is negligibly small, we obtain an expression which describes electric susceptibility for 'Curie-Weiss' behaviour:

$$\chi = \frac{1}{\alpha(T-T_0)+3BP_s^2} \tag{1.8}$$

where P_s is the equilibrium value of the spontaneous polarisation at zero field.

Equation 1.8 can therefore be solved for electric susceptibility in relation to the spontaneous polarisation above and below the phase transition temperature which develops continuously or discontinuously depending on the order of the transition.

1.4.1 Second-order (continuous) phase transition

When B is positive and sixth-order terms are negligibly small in the free energy expansion (Equation 1.4), a thermodynamically second-order phase transition is described. In this case, the spontaneous polarisation develops continuously in zero-field ($E=0$) below the transition temperature T_c, which in this case equals the Curie-Weiss temperature T_0. The spontaneous polarisation for $T<T_c$ can be determined from Equation 1.6, to obtain:

$$P_S = \pm \sqrt{\frac{\alpha}{B}(T_c - T)} \qquad (1.9)$$

From Equation 1.9 two solutions with equal magnitude but different signs ($\pm P_S$) exist in the ferroelectric state. Two minima corresponding to the same value of free energy exist for $\pm P_S$ as can be seen for $T<T_c$ in Figure 1.6a; these minima correspond to oppositely orientated polarisations. The spontaneous polarisation develops continuously up to T_c as can be seen in Figure 1.6b. Above T_c, were the spontaneous polarisation equals zero, the minimum in free energy is indicated by one single well as shown in Figure 1.6a. The electric susceptibility is also displayed in Figure 1.6b, determined by Equation 1.8, demonstrating that χ is expected to diverge towards infinity at the transition temperature, T_c [15]. One example of a ferroelectric which exhibits a second-order (continuous) phase transition is triglycine sulphate [22].
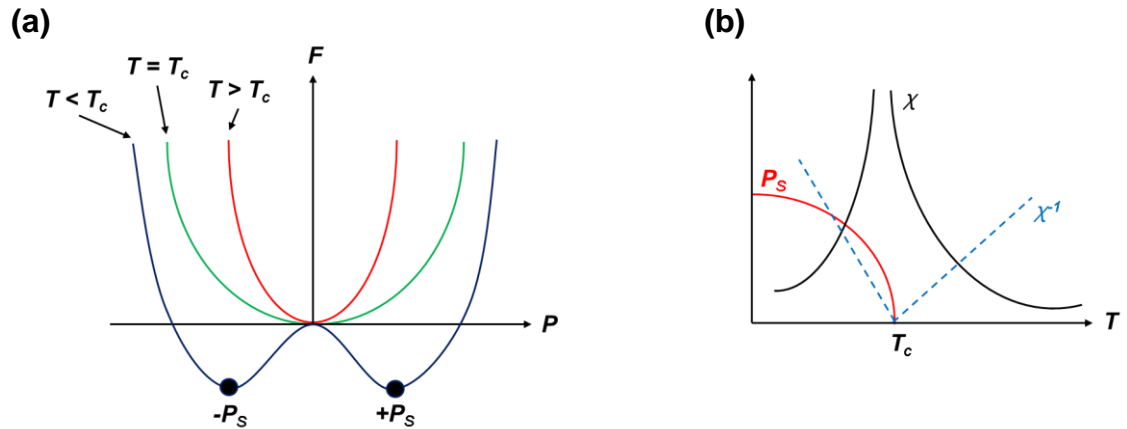
Figure 1.6: Free energy (F) as a function of polarisation (P) of a ferroelectric displaying a second-order phase transition (a). The continuous development of spontaneous polarisation (P_S) (red line), the Curie-Weiss behaviour of electric susceptibility (χ) (black line) and inverse electric susceptibility (χ^{-1}) (blue dashed line) transitioning through the Curie temperature (T_c) (b).

1.4.2 First-order (discontinuous) phase transitions

When B is negative and the sixth-order term is included in the free energy expansion (Equation 1.4), a thermodynamically first-order phase transition is described. In the high temperature paraelectric state ($T \gg T_c$ and $P_s=0$) the free energy minimum is indicated by a single well similar to the second-order free energy diagram in Figure 1.6. In the case of a first-order phase transition however, T_0 is less than T_c leading to some non-zero metastable polarisation states around the transition temperature as shown in Figure 1.7a. At these temperatures paraelectricity is stable and ferroelectricity is metastable giving three minima in free energy [21]. Once T_c is reached, all three minima are degenerate and equally stable [13]. However, on cooling below T_c the ferroelectricity becomes more

energetically favoured and is stabilised below T_0. The spontaneous polarisation, determined from Equation 1.4 (including the sixth-order term), for the low temperature ferroelectric phase ($P_s>0$), gives:

$$P_S{}^2 = \frac{-B \pm \sqrt{B^2 - 4\alpha C(T-T_0)}}{2C} \tag{1.10}$$

Due to the metastability of ferroelectricity in the vicinity of the phase transition temperature, the spontaneous polarisation develops discontinuously as can be seen in Figure 1.7b. This discontinuous jump in polarisation is further demonstrated by the development of the electric susceptibility (determined by Equation 1.8) through the phase transition temperature [21]. An example of a ferroelectric displaying a first-order phase transition is BaTiO$_3$ [23] which is one of the materials studied in this thesis.
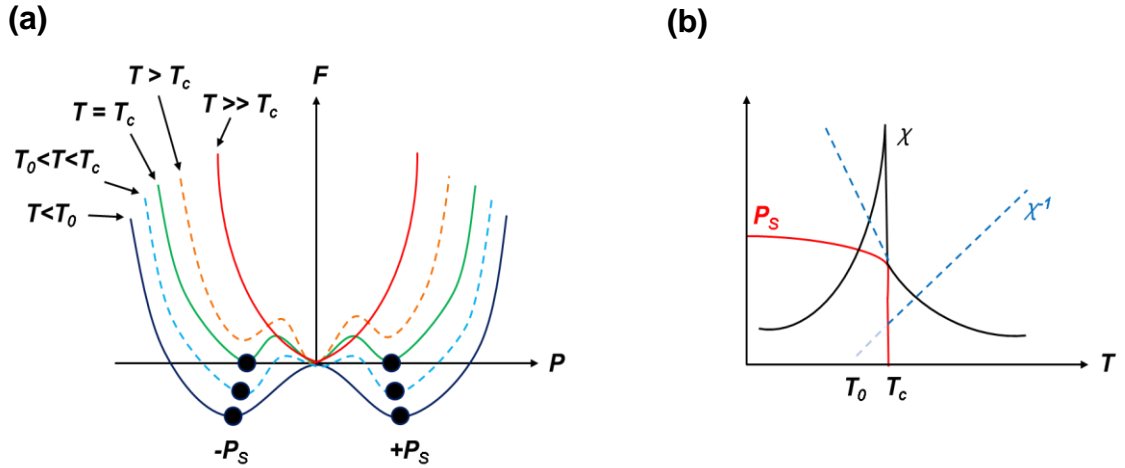
Figure 1.7: Free energy (F) as a function of polarisation (P) of a ferroelectric displaying a first-order phase transition (a). The discontinuous development of spontaneous polarisation (P_s) (red line), the Curie-Weiss behaviour of electric susceptibility (χ) (black line) and inverse electric susceptibility (χ^{-1}) (blue dashed line) transitioning through the Curie temperature (T_c) (b).

1.5 Ferroelectric Domains

In general, the spontaneous polarisation in a ferroelectric crystal is not uniformly aligned throughout the whole crystal [24]. Regions which have uniform dipole alignment are called domains. Ferroelectric domains form to minimise the electrostatic energy of depolarisation fields ('E_{dep}' in Figure 1.8) created by surface charges which form at the onset of the spontaneous polarisation, at the paraelectric-ferroelectric transition temperature. The depolarising field is orientated oppositely to the spontaneous polarisation and may be very strong (MVm^{-1}) rendering the single-domain state in Figure 1.8a energetically
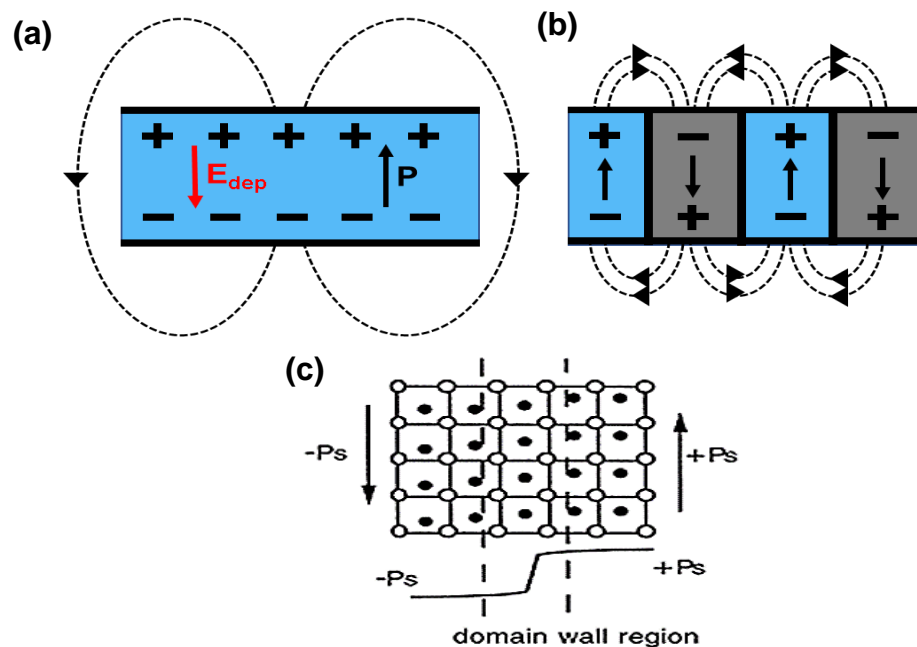
Figure 1.8: Ferroelectric single-domain state produces surfaces charges creating a depolarising field (*Edep)* (a). The formation of 180° domains reduces *Edep* (b), a larger number of domains would further reduce *Edep*. Schematic of a 180° domain wall (c). Adapted from [21, 24].

unfavourable [24]. The electrostatic energy of the depolarising field may be minimised if the ferroelectric crystal splits into domains with oppositely oriented polarisation. The ferroelectric domains seen in Figure 1.8b have anti-aligned spontaneous polarisation and are known as '180° domains', the interfaces which separate 180° domains are known as '180° domain walls' (Figure 1.8c) and are generally considered to be sharp interfaces i.e. ~1 nm, in direct contrast to ferromagnets which have a domain wall width of ~100 nm [25]. This highlights the high values of anisotropy and low exchange energy in ferroelectrics compared to that of ferromagnets [26]. Domain walls in ferromagnets are generally Néel- or Bloch-type walls and have continuous rotation of magnetisation (Figures 1.9a and 1.9b), whereas ferroelectric domain walls are typically Ising-type where the magnitude of the polarisation reduces to zero through the boundary without significant rotation (Figure 1.9c) [27].
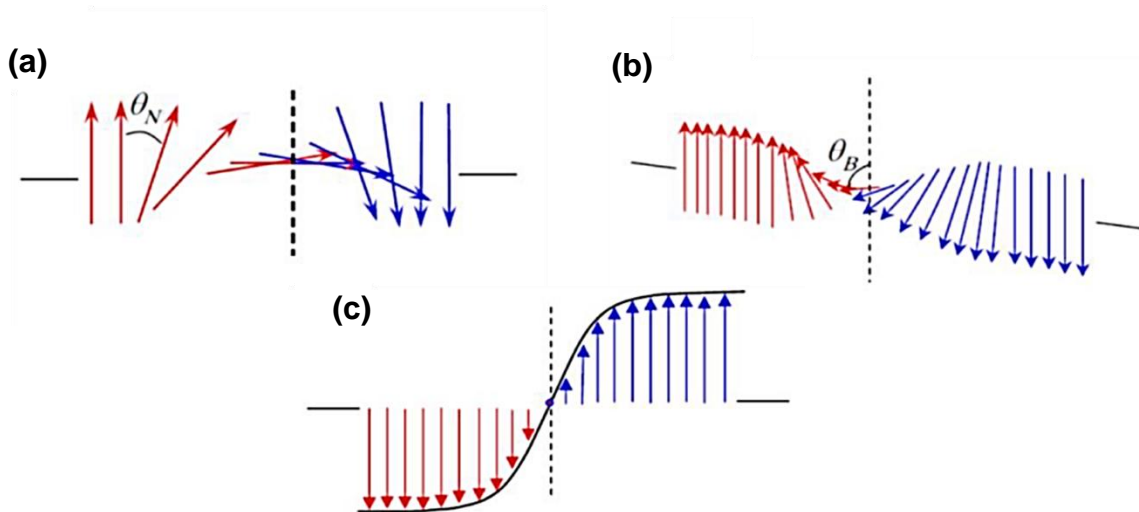
Figure 1.9: Néel- (a) and Bloch- (b) type domain walls seen in ferromagnets, magnetisation rotates through the angles θ_N and θ_B respectively. Ising-type domain wall (c) seen in ferroelectrics, polarisation has zero rotation in an ideal case. Adapted from [27].

1.6 Ferroelastic Domains

As well as offsetting depolarising fields, domains can form in response to the strain imposed on a crystal by a mechanical stress, and these domains are known as 'ferroelastic' domains [24]. For example, when cooling through the paraelectric-ferroelectric transition temperature, in an attempt to maintain the paraelastic initial shape (represented by the dashed box in Figure 1.10a) a ferroelectric tetragonal crystal will split into orthogonal polar orientation, leading to regions known as '90° domains' shown in Figure 1.10b. Since the direction of the spontaneous polarisation varies by 90° from domain to domain, the depolarising fields are offset in a manner analogous to 180° domains. Whilst both 180° and 90° domains can reduce electrostatic energy, only 90° domains can alleviate spontaneous strains [24]. The interfaces which separate ferroelastic domain walls are known as 'ferroelastic domain walls', a schematic of a 90°
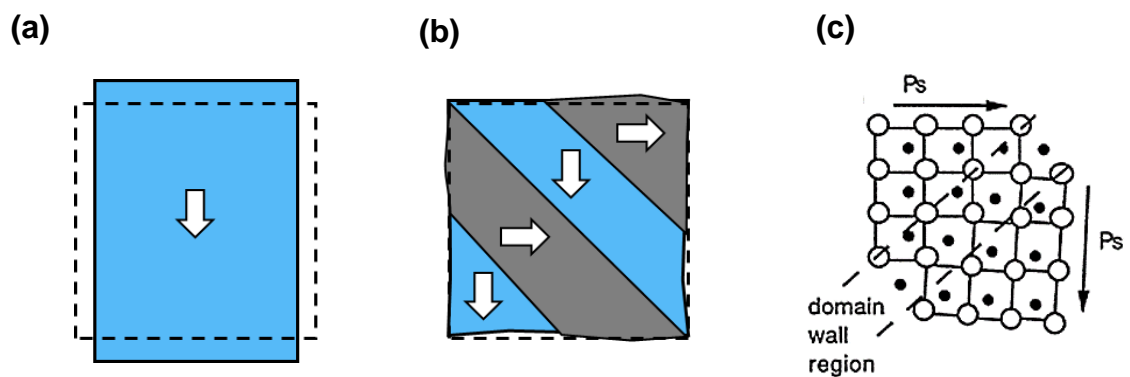
Figure 1.10: Tetragonal phase associated with cooling through T_c, the high temperature paraelectric phase is illustrated by a dashed box (a). The formation of ferroelastic domains reduces the elastic energy by forming a combined shape closer to the original (b). Schematic of a 90° ferroelastic domain wall (c). Adapted from [16, 24, 28].

ferroelastic domain wall is shown in Figure 1.10c. Increasing the density of ferroelastic 90° domains leads to a more complete compensation of strains and the domain period can be estimated using Kittel's domain scaling relation [29, 30], given by:

$$G(w,d) = Uw + \frac{\gamma d}{w} \qquad (1.1)$$

where G is the elastic free energy (replacing the analogous surface energy term in ferroelectric domains), which depends on the domain width (w) and thickness of material (d). U and γ are constants (the areal energy density associated with charged surfaces and the domain wall energy density respectively) for a given system [11].

It is worth noting, as a large part of this thesis is based on imaging ferroelastic domains, that ferroelastic domains can appear differently depending on which orientation they are observed (or 'viewed') from. To illustrate this, a schematic of a cubed section of ferroelectric material containing ferroelastic domains has been drawn in Figure 1.11. When the front-face of the cube (labelled '1') is viewed, a pattern of in-plane ferroelastic domains displaying orthogonal polarisation from one domain to the next is observed. These domains are called 'a-a domains' (because the polarisation is entirely in-the-plane of the cube face 1 for each domain) having domain walls which are orientated along {110}$_{pc}$ planes. To observe how these a-a domains are projected through the thickness of the cube, we turn to the face labelled '2'. Here, the same set of domains appear with walls projected along <100>$_{pc}$ directions, the domains still vary in polar direction by 90° however, this time one set of domains has polarisation directed out-of-plane of the cube face 2, owing to a combination of in-plane and out-of-plane domains

known as 'a-c domains'. The same situation is present when viewing the ferroelastic domains from the face labelled '3'.
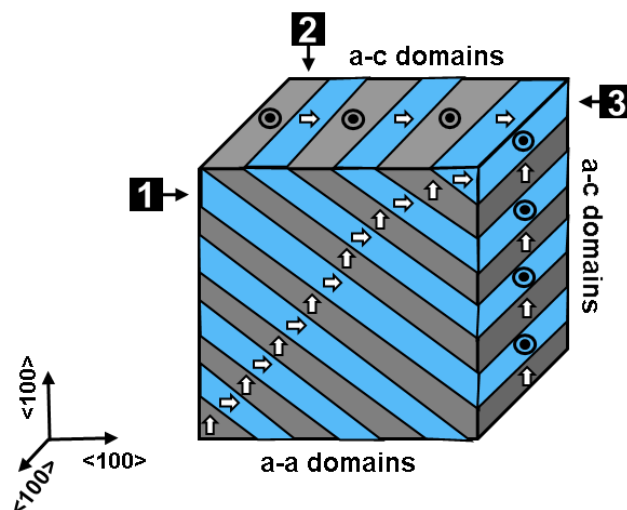
Figure 1.11: A cubed section of ferroelectric material made up of ferroelastic 90° domains. The domains appear as 'a-a domains' when viewed from face 1 but as 'a-c domains' when viewed from faces 2 and 3. Adapted from [28].

1.7 Domains in polycrystalline ferroelectrics

In polycrystalline ferroelectrics (bulk ceramics), the overall domain pattern can look quite different compared to a single crystal because the domain structure of each grain is formed under elastic clamped conditions by its surrounding neighbour grains, whereas a single crystal is free [31]. A grain in a ceramic is

clamped by its neighbouring grains in all three dimensions and can deform only by a cooperative motion of the adjacent grains. Maintaining the grain shape when transitioning from the paraelectric to ferroelectric state generates high internal stresses which can be alleviated by the formation of an intricate pattern of ferroelastic domains to preserve the gross shape of the grains. Arlt et al. studied in detail the domain structure in ferroelectric ceramics, and revealed that the domain pattern depends on the grain size [32], for example fine-grained ceramics (<~3 μm diameter) will favour a simple laminar structure (shown in Figure 1.12a) whereas coarse-grained ceramics (>~3 μm diameter) tend to favour a banded laminar structure to allow stress relief (Figure 1.12b). Figure 1.12c shows a scanning electron microscope (SEM) image of a $BaTiO_3$ ceramic which has an average grain size of 5μm, in which the ferroelastic domain pattern, which is banded laminar, is visible.
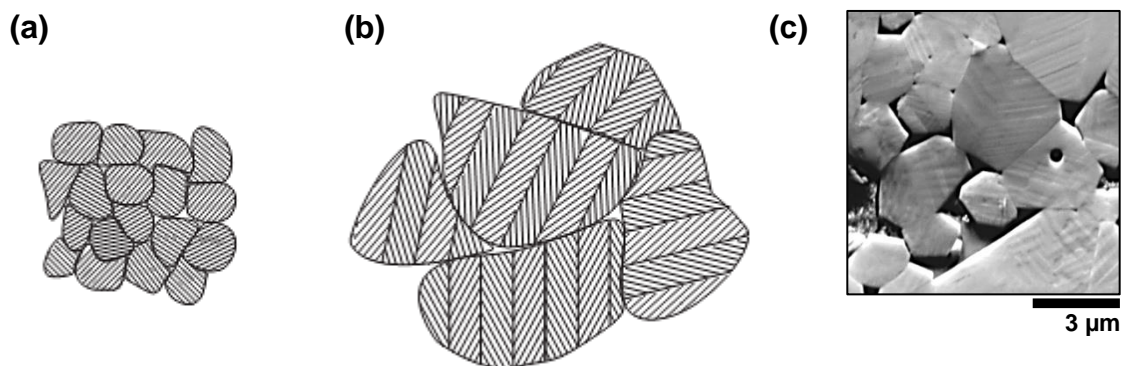
Figure 1.12: Ferroelastic domain pattern in ferroelectric ceramics. (a) Schematic of a fine-grained ceramic. (b) Schematic of a coarse-grained ceramic. (c) SEM image of a $BaTiO_3$ ceramic containing a banded laminar domain pattern. Schematics (a)-(b) from [21].

1.8 Domains in epitaxially strained thin-films

In thin films, epitaxial strain can be used as an additional degree of freedom to tune ferroelastic domain configuration [33, 34]. By growing thin films on substrates which have an in-plane lattice mismatch, ferroelectricity can be greatly enhanced [35] or even created [36] within a thin-film. In this thesis, the ferroelectric thin film of interest is bismuth ferrite ($BiFeO_3$) which in its bulk form has a room-temperature rhombohedral structure (a=3.97 Å). When $BiFeO_3$ is epitaxially grown onto lanthanum aluminate ($LaAlO_3$) which is also rhombohedral at room temperature (a=3.79 Å) a compressive strain of -4.4% is created due to the lattice mismatch. The $BiFeO_3$ thin-film accommodates this huge strain by forming a mixture of polymorphs which correspond to different phases. It should be noted that $BiFeO_3$ polymorphs are analogous to ferroelastic 'domains' in terms of the spontaneous polarisation varying from polymorph to polymorph; in addition to the fact that the polymorphs are formed due to strain. However, for consistency with literature only the term 'polymorph' will be used from here on throughout this thesis, and the boundaries which separate the $BiFeO_3$ polymorphs will be referred to as 'morphotropic phase boundaries (MPB)'. A scanning transmission electron microscope (STEM) image of the polymorphs (labelled R and T) in mixed-phase $BiFeO_3$ is shown in Figure 1.13. The highly-strained tetragonal-like T polymorphs demonstrate a strikingly high spontaneous polarisation, around 1.5 times that of bulk $BiFeO_3$ [35]. Specific details on polymorph structure and the ability to reorganise (or switch between) phase mixtures will be expanded upon in Chapter 5 of this thesis.
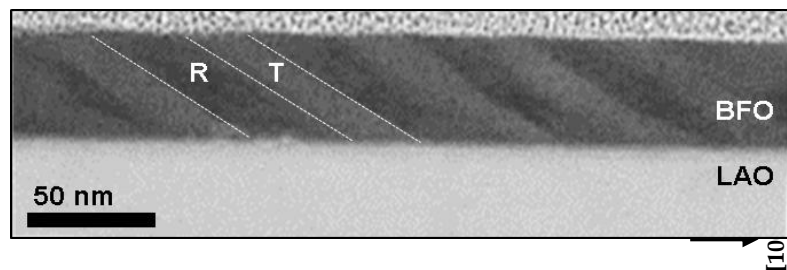
Figure 1.13: STEM image of T and R polymorphs formed in epitaxially strained BiFeO$_3$ grown on a LaAlO$_3$ substrate.

1.9 References

[1] J. Valasek, *Phys. Rev.* **1920**, *(15)*, 537.

[2] J. Seidel, L. W. Martin, Q. He, Q. Zhan, Y. -. Chu, A. Rother, M. E. Hawkridge, P. Maksymovych, P. Yu, M. Gajek, N. Balke, S. V. Kalinin, S. Gemming, F. Wang, G. Catalan, J. F. Scott, N. A. Spaldin, J. Orenstein, R. Ramesh, *Nature Materials.* **2009**, *8*(3), 229-234.

[3] J. F. Scott, *Journal of Physics-Condensed Matter.* **2008**, *20*(2), 021001.

[4] R. E. Newnham, "*Structure-Property Relations*", Springer-Verlag, **1975**.

[5] C. Ahn, K. Rabe, J. Triscone, *Science.* **2004**, *303*(5657), 488-491.

[6] M. E. Lines, A. M. Glass, "*Principles and Applications of Ferroelectrics and Related Materials*", Oxford University Press, New York **1977**.

[7] R. Comes, M. Lambert, A. Guinier, *Solid State Commun.* **1968**, *(6)*, 715-719.

[8] A. S. Chaves, F. C. Barreto, R. A. Nogueira, *Phys. Rev. B*, **1976**, *(13)*, 207-212.

[9] B. Ravel, E. A. Stern, R. I. Vedrinskii, V. Kraizman, *Ferroelectrics*, **1998**, *(206)*, 407-430.

[10] B. Zalar, V. V. Laguta, R. Blinc, *Phys. Rev. Lett.* **2003**, *(90)*,037601.

[11] R. G. P. McQuaid, *QUB PhD Thesis, "Domain Patterns and Domain Wall Dynamics in Small-Scale Ferroelectrics"*, **2012.**

[12] P. R. Potnis, N. Tsou, J. E. Huber, *Materials.* **2011**, *4*(2), 417-447.

[13] H. D. Megaw, "*Feroelectricity in Crystals*", Butler & Tanner, U.K. **1957**.

[14] L. D. Landau, *Phys. Z. Sowjun*, **1937**, *(11)*, 545.

[15] P. Chandra, P. B. Littlewood, *"A Landau Primer for Ferroelectrics" in 'Physics of Ferroelectrics: A Modern Perspective'*, Springer-Verlag, Berlin **2007**, pp. 69.

[16] J. Toledano, P. Toledano, *"The Landau Theory of Phase Transitions"*, World Scientific, Singapore **1987**.

[17] A. F. Devonshire, *Phil. Mag.* **1949**, *(40)*, 1040.

[18] A. F. Devonshire, *Phil. Mag.* **1951**, *(42)*, 1065.

[19] A. Putnis, *"Introduction to Mineral Sciences"*, Cambridge University Press, Hampshire, U.K. **1995**.

[20] T. Mitsui, I. Tatsuzaki, E. Nakamura, *"An Introduction to the physics of ferroelectrics"*, Gordon and Breach Science, London **1976**.

[21] R. Waser, U. Bottger, S. Tiedke, Eds, *"Polar Oxides: Properties, Characterisation, and Imaging"*, WILEY-VCH, Germany **2005**.

[22] K. Uchino, *"Ferroelectric Devices"*, Marcel Dekker, New York, U.S.A **2000**.

[23] W. J. Merz, *Phys. Rev.* **1949**, *(76)*, 1221.

[24] D. Damjanovic, *Reports on Progress in Physics.* **1998**, *61*(9), 1267-1324.

[25] M. Klaeui, *Journal of Physics-Condensed Matter.* **2008**, *20*(31), 313001.

[26] N. A. Spaldin, *Physics of Ferroelectrics: a Modern Perspective.* **2007**, *105*, 175-217.

[27] D. Lee, R. K. Behera, P. Wu, H. Xu, S. B. Sinnott, S. R. Phillpot, L. Q. Chen, V. Gopalan, *Physical Review B.* **2009**, *80*(6), 060102.

[28] L. J. McGilly, *QUB PhD Thesis, "*Domain Topologies in Nanoscale Single-Crystal Ferroelectrics", **2011***.

[29] C. Kittel, *Phys. Rev.* **1946**, *(70)*, 965-971.

[30] A. Schilling, R. M. Bowman, G. Catalan, J. F. Scott, J. M. Gregg, *Nano Letters.* **2007**, *7*(12), 3787-3791.

[31] G. Arlt, D. Hennings, G. de-With, *J. Appl. Phys.* **1985**, *(58)*, 1619.

[32] G. Arlt, *J. Mat. Sci.* **1990**, *(25)*, 2655.

[33] M. Dawber, K. Rabe, J. Scott, *Reviews of Modern Physics,* **2005**, *77*(4), 1083-1130.

[34] V. Nagarajan, I. Jenkins, S. Alpay, H. Li, S. Aggarwal, L. Salamanca-Riba, A. Roytburd, R. Ramesh, *J. Appl. Phys.* **1999**, *86*(1), 595-602.

[35] D. Sando, B. Xu, L. Bellaiche, V. Nagarajan, *Applied Physics Reviews.* **2016**, *3*(1), 011106.

[36] S. Venkatesan, A. Vlooswijk, B. J. Kooi, A. Morelli, G. Palasantzas, J. T. M. De Hosson, B. Noheda, *Physical Review B.* **2008**, *78*(10), 104112.

2. Microscopy Techniques

This chapter describes the microscopy techniques involved in studying the ferroelectric samples in this thesis. An overview of the transmission electron microscope is described, with emphasis on the various imaging modes and spectroscopy techniques carried out. The focused ion beam sample preparation method is also described, a necessary step in creating electron transparent samples suitable for transmission electron microscopy. Additional atomic force microscopy techniques used to accompany the transmission electron microscopy within this thesis are also described.

2.1 Overview of Transmission Electron Microscopy

A transmission electron microscope (TEM) operates by accelerating a beam of electrons to sufficient energy so that when incident on a very thin sample (<100 nm), electrons are transmitted through it. Conventional TEMs work on the same principle as light microscopes but utilise a beam of electrons which travel in vacuum and originate from an electron gun source, rather than using a light source (see TEM optics in Figure 2.1). The first TEM was built by Ernst Ruska and Max Knoll in 1931 [1], with the first commercial TEM developed only four years later. The invention of the TEM came about due to the limitations of using light for imaging objects, as optical microscopes are constrained by the resolution and diffraction limits of the wavelengths of visible light.

For any optical system, the theoretical diffraction resolution limit, d_0, is given by Rayleigh's criterion (equation 2.1). This criterion describes the smallest resolvable distance between two points, where λ is the wavelength of the illuminating source and NA is the objective numerical aperture ($NA = n\sin\theta$ where n is the refractive index of the medium and θ is the aperture angle).

$$d_0 = \frac{0.61\lambda}{NA} \qquad\qquad (2.1)$$

From equation 2.1, it is apparent that d_0 is proportional to wavelength and therefore a straightforward approach to improve the resolution would be to use an illumination source with a shorter wavelength, such as electrons. It is known

from Louis de Broglie's work that electrons, while considered as particles, can also have wave-like properties such that:

$$\lambda = \frac{h}{p} = \frac{h}{mv} \tag{2.2}$$

where λ is the de Broglie wavelength, h is Planck's constant and p is the electron's momentum. Therefore, increasing the momentum of an electron beam will decrease its wavelength, and as a result greatly increase the resolution limit over that attainable by visible light.

In the TEM, when an electron (with charge e) passes through a potential difference V, its kinetic energy will be equal to the energy of the field i.e. eV (energy in electron volts):

$$\frac{mv^2}{2} = eV \tag{2.3}$$

Substituting a rearranged version of equation 2.2 into equation 2.3, gives:

$$\frac{1}{2}m\left(\frac{h}{m\lambda}\right)^2 = eV \tag{2.4}$$

And rearranging equation 2.4 gives the non-relativistic electron wavelength:

$$\lambda = \frac{h}{(2meV)^{\frac{1}{2}}} \tag{2.5}$$

However, relativistic effects cannot be ignored because the velocity of electrons increases with the square root of the accelerating voltage (equation 2.5), meaning that at an accelerating voltage of 100 kV, the velocity of electrons is already greater than half the speed of light. To account for this, we consider the relativistic form of the kinetic energy, E_k:

$$E_k = mc^2 - m_0 c^2 \tag{2.6}$$

where m_0 is the rest mass of an electron and c is the speed of light. Noting again that the kinetic energy is determined by the accelerating voltage ($E_k = eV$) then rearranging for m gives:

$$m = \frac{eV + m_0 c^2}{c^2} \tag{2.7}$$

which can be substituted into equation 2.5 to give the relativistic electron wavelength:

$$\lambda = \frac{h}{\left[2m_0 eV \left(1 + \frac{eV}{2m_0 c^2} \right) \right]^{\frac{1}{2}}} \tag{2.8}$$

For a TEM operating with an accelerating voltage of 200 kV, the theoretical wavelength of the electrons will be ~2.51 pm (much smaller than the wavelength of visible light (550 nm for green light). Hence, the electron beam can reach a theoretical resolution limit smaller than atoms themselves. However, this theoretical resolution does not consider the aberrations which are present in the optics of a TEM; the aberrations limit the resolution in TEM beyond this theoretical limit. More detail on aberrations will be given in section 2.1.3.

The main components of the TEM are shown schematically, along with the corresponding ray diagram, in Figure 2.1. The main components consist of: the electron gun (source of electrons); gun alignment controls; condenser lenses (magnetic lenses to collimate the beam); objective lens (to focus and initially magnify the image); apertures (to limit the diameter of the electron beam); intermediate lens; projective lens; sample holder; viewing screen and detectors to

pick up the main and secondary signals. There are four main parameters which determine the nature and the quality of the image or spectrum obtained with a TEM, these are the probe size, convergent angle, electron energy and the electron probe current [2].
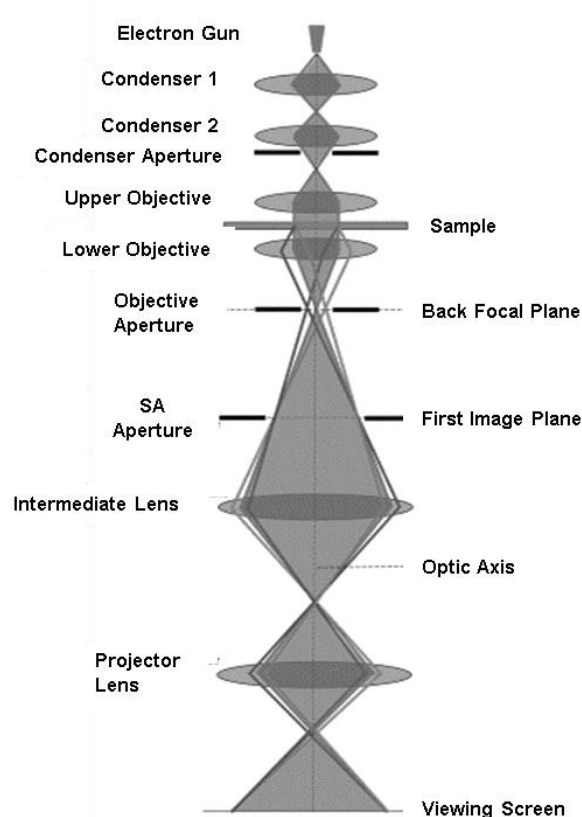
Figure 2.1: Schematic ray diagram of a conventional TEM microscope. Adapted from [3].

2.1.1 Electron Sources

For TEM, electron beams may be generated from two main types of sources: thermionic and field emission guns. Thermionic guns operate by heating a source (LaB_6 being the only thermionic source in modern TEMs [2]) which is used as the

cathode. In addition to the cathode there is a grid called a Wehnelt cylinder (which acts like a simple electrostatic lens, the first lens the electrons pass through in the TEM) and an anode at earth potential with a hole in its center. The cathode is connected to the high-voltage supply while a metal wire, such as rhenium, is attached to the LaB_6 crystal which is resistively heated to cause thermionic emission of electrons. The thermionic emission can be summarised by Richardson's law which relates the current density from the source, J, to the operating temperature, T in Kelvin:

$$J = AT^2 e^{-\frac{\Phi}{kT}} \tag{2.9}$$

When leaving the cathode, the electrons have a negative potential of the chosen acceleration voltage (e.g. 200 kV) with respect to the anode so they accelerate through this potential difference acquiring an energy of 200 keV. Due to the self-biasing design of the gun, a small negative bias is applied to the Wehnelt cylinder meaning that as the electrons come off the cathode they are converged into a point called a crossover leading to a controllable beam of electrons ready to pass through the next set of lenses in the TEM.

A field emission gun (FEG) works in a different way, emitting electrons due to an applied electric field. The principle of a FEG is that the strength of an electric field E is increased at sharp points if a voltage V is applied to a tip (sharp point) of radius r, then:

$$E = \frac{V}{r} \tag{2.10}$$

The tip is most commonly made from tungsten (W) wire which can readily be given a tip radius of <0.1 μm (Figure 2.2a). For a FEG to operate, the W tip is made

to be the cathode with respect to two anodes (see Figure 2.2b). When the first anode is positively charged by a few kV with respect to the tip, this charge generates an extraction voltage because the electric field created is large enough to pull electrons out of the W tip. The electrons are then accelerated to the chosen voltage by the second anode. The combination of the two anodes acts like an electrostatic lens to produce a crossover. For field emission to occur the surface must be free of contaminants and therefore an ultra-high vacuum ($<10^{-9}$ Pa) is necessary [2].

Although FEGs have a higher cost than thermionic guns, they are superior in terms of the quality of the electron beam produced having a smaller energy spread and a smaller spot size [4]. FEGs can be further distinguished by two different designs: a Schottky (or warm) FEG and a cold FEG. To achieve an energy spread of below 0.5 eV with a high beam coherence, a cold FEG is required. The increased energy resolution does however come with a drawback, namely the cold FEGs emission decreases with time due to changes in the tip and the arrival of impurity atoms on the surface. Therefore, the tip needs to be flash heated periodically to remove any impurities and to restore the emission level [4].

(a)   **(b)**
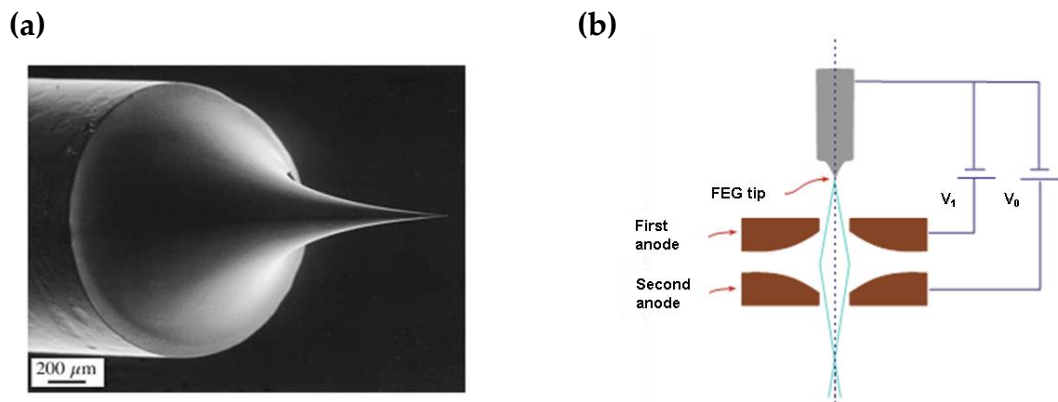
Figure 2.2: Scanning electron microscope (SEM) image of a Field emission gun (FEG) W tip (a). Electron paths from a FEG tip showing how the electron beam crossover is formed (b). From [2].

2.1.2 Electron Optics in the TEM

Lenses in the TEM are the electromagnetic equivalent of the glass lenses in a light microscope. A typical electromagnetic lens (see schematic in Figure 2.3) is rotationally symmetric and consists of a copper coil wound around a soft iron pole piece which has a hole drilled through it. The hole in the pole piece is known as the *bore* of the pole piece. When a current is passed through the coil, a magnetic field is created in the bore. Electrons passing through the bore undergo a focusing effect which is dependent on the coil current and can be increased in doing so increasing the strength of the resultant magnetic field. The small gap in the pole piece concentrates the field and shortens the focal length of the lens [4]. It is the strength of the magnetic field that controls the electron path trajectories, the force *F* on an electron (charge, *e*) travelling with velocity v in a magnetic field *B* is given by the Lorentz force equation:

$$F = -e(v \times B) \tag{2.11}$$
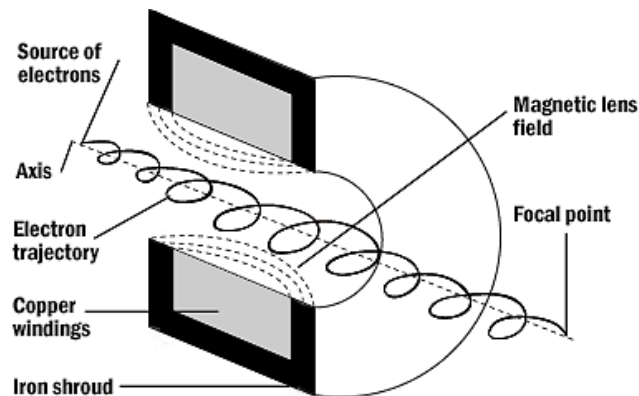
Figure 2.3: A schematic diagram of an electromagnetic lens in the TEM. From [5].

F is the magnitude of the force where $|F| = |B|e|v|\sin\theta$ and θ is the angle between B and v. If the lens has a homogeneous field then electrons which pass exactly through the centre having a component of v parallel to B, will experience no force. But, the electrons which pass some distance off the main axis (having a perpendicular component) will spiral towards the centre and then out again, leading to a focusing action. The magnitude of the magnetic field (which is determined by the current applied to the lens coil) governs the focal length of the lens; using a combination of lenses gives a range of image magnifications while correcting for image rotations which would occur in the use of a single lens [4]. In addition, the resistive heating of the coil means that the lenses must be cooled by a water recirculating system in the TEM.

In a TEM, the first set of electromagnetic lenses that the electrons pass through after emission from the gun are the *condenser* lenses, C1 and C2. The C1 lens controls the spot size of the beam, creating a crossover of the electrons from the gun lens. The C2 lens controls the convergence angle of the beam and can be used to create a parallel or a convergent beam depending on the mode desired by the user operating the TEM.

The next (and arguably the most important) set of electromagnetic lenses that the electrons pass through in the TEM are the objective lenses. The sample is located in between these two lenses, their purpose being to focus the beam onto the sample and to form an initial inverted image of the sample.

The intermediate lens further down the TEM column is used to magnify the initial image formed by the objective lens onto the viewing screen (imaging mode) shown schematically in Figure 2.4a, or, by changing the excitation of the

intermediate lens project the diffraction pattern which is brought to focus on the back focal plane (BFP) of the objective lens onto the viewing screen (diffraction mode), shown schematically in Figure 2.4b.
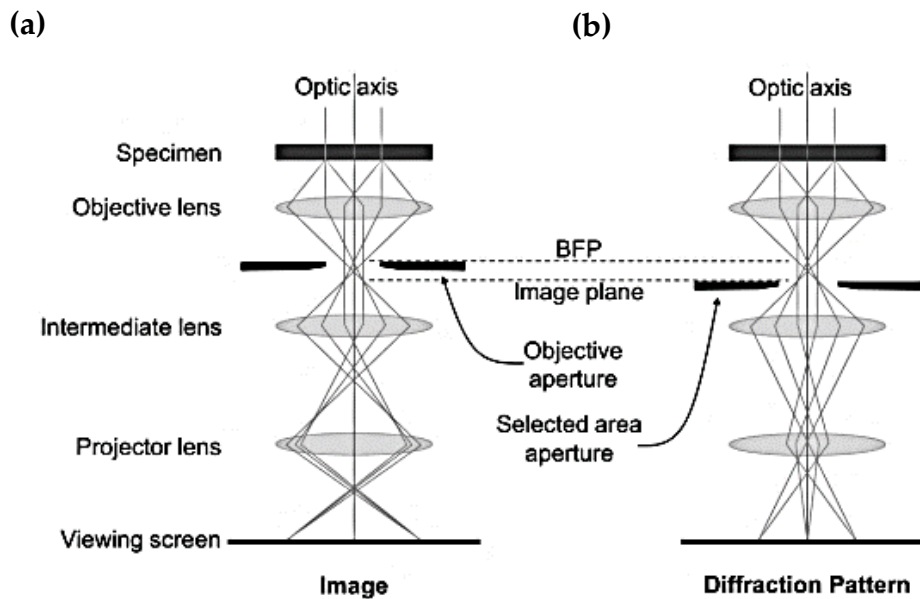
Figure 2.4: Varying the strength of the intermediate lens moves its object plane to, either the image plane forming an image on the screen (a) or, the back focal plane (BFP) forming a diffraction pattern on the viewing screen (b).

2.1.3 Aberrations

In an *ideal* TEM (or any optical system) every point on the object will be reproduced in the image, but in reality, this is not the case as electrons which are closer to the optical axis are not focused to the same point as electrons further from the optical axis. This defect within the electromagnetic lenses is known as *spherical aberration (C_s)*. A schematic of positive spherical aberration within a lens

is shown in Figure 2.5a, where we can express the diameter of the spherically distorted disk of intensity d_{sph} in terms of the collection semiangle of the lens, β, and the spherical aberration coefficient, C_s, of the lens [2]:

$$d_{sph} = \frac{1}{2} C_s \beta^3 \qquad (2.12)$$

Another common type of aberration is known as *chromatic aberration C_c*, which arises due to the electron beam not being monochromatic. This spread of energies (E_1, E_2 etc.) in the electrons may be due to fluctuations in the gun accelerating voltage causing an energy spread in the electrons leaving the source, or, different energy losses due to interactions with the sample. Like spherical aberration, the diameter of the chromatic disc of least confusion, d_{chr}, can be expressed by:

$$d_{chr} = C_c \frac{\Delta E}{E_0} \beta \qquad (2.13)$$

Where ΔE is the energy loss, E_0 the incident energy and C_c is the chromatic aberration coefficient of the lens[2]. A schematic of chromatic aberrations in a lens resulting in electrons of different energies being brought to focus at different points along the optic axis is shown in Figure 2.5b.

Astigmatism is another type of aberration in the TEM which occurs when electrons sense a non-uniform magnetic field as they spiral down the electron column. Astigmatism arises due to defects in the soft-iron pole pieces (it is practically impossible to machine them to be perfectly cylindrically symmetrical) or if the apertures are not clean, contamination can charge up and deflect the beam[2]. Astigmatism can distort the image by an amount d_{ast} given by:

$$d_{ast} = \beta \Delta f \qquad\qquad (2.14)$$

Where Δf is the maximum difference in focus induced by the astigmatism. Luckily, astigmatism is easily corrected by using stigmators, which are small octupoles that introduce a compensating field to balance out the in homogeneities in the magnetic field.

Fortunately, the effect of C_s and C_c aberrations can be overcome by using aberration correctors. Spherical aberration correction was first theorised by Scherzer in 1947 and made possible in the TEM, after many years of practical problems based on design, in 1997 [6]. A C_s corrector can compensate for the
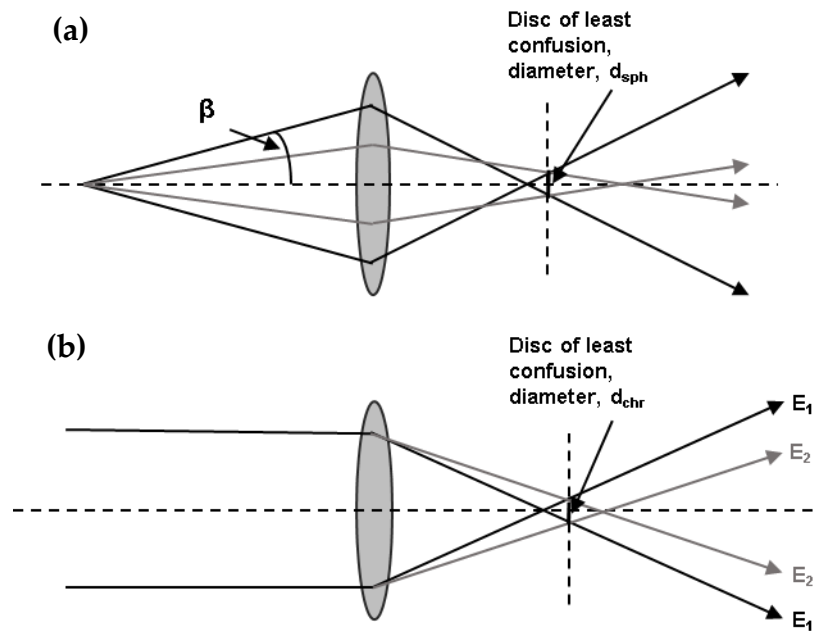
Figure 2.5: Spherical (a) and chromatic (b) aberrations in the lens. The disc of least confusion marks the plane where the effects of the aberration are minimised. Adapted from [4].

natural distortion in the lens by using multi-pole lenses in series with the objective lens. There are two types of C_s correctors: the quadrupole-octupole and the hexapole corrector. By producing a negative C_s, the corrector compensates for the positive C_s in the objective lens, resulting in zero C_s. Before C_s correction was available, a high-quality system delivered about 1 nA of current into a picture element 1 nm in size; this amounts to about 5000 million electrons per second. With C_s correction, the system delivers about the same current into a picture element 0.1 nm or 1 Å in size [4]. The ability to correct C_c has also been made possible within the last decade with the design of C_c correctors [7], however, unfortunately C_c correction was not available on the TEMs used for this thesis.

2.2 Beam – Sample Interactions

As the accelerated electrons become incident on the sample various interactions can occur. Firstly, an electron may pass through the sample directly with no interactions at all. However, most likely the electrons will be scattered by the Coulomb forces generated by the nuclei and orbiting electrons of the sample. These electrons can either be scattered elastically (implying that the energy lost by the primary electron is either zero or too small to be detected) or inelastically (implying an energy loss of the primary electron which is big enough to be detected in the microscope). Elastic scattering occurs mainly from interactions with atomic nuclei (or the whole electrostatic field of the atom) and is responsible for diffraction from crystalline samples, used to reveal structure. Meanwhile, inelastic scattering mainly involves electron-electron interactions and can be

exploited for chemical analysis, for example by electron energy loss spectroscopy (EELS), or for analysing Kikuchi patterns, these are bands of alternating dark and light bands in diffraction mode. Kikuchi patterns are formed by electrons which have been previously inelastically scattered, they are related to atomic spacing and can be followed like "road maps" to the elastically scattered electron diffraction pattern (by tilting the sample). The inelastic scattering of a primary electron also leads to the generation of X-rays which can be detected and analysed using energy dispersive X-ray (EDX) spectroscopy.

2.3 Electron Diffraction

Electron diffraction is the result of Bragg scattering as the electron beam passes through a crystalline sample. Crystals act as three-dimensional gratings allowing the waves (electrons) to be scattered from the lattice planes separated by lattice constant, d. When the scattered waves interfere constructively, they remain in phase and the path difference between the two waves undergoing interference is given by Bragg's law:

$$2d_{hkl} \sin \theta \approx n\lambda \qquad (2.15)$$

where θ is the scattering angle of the wave and n is the integer multiple of the wavelength (or order of reflection). The collective effect of scattering from successive crystallographic planes of the crystal lattice (described by Miller notation, hkl) increases the amount of constructive interference and intensifies the resultant reflections in the diffraction pattern (DP). In TEM, an aperture (metal

strip with holes to limit the beam size) can be inserted to generate a DP from a selected area of the sample (called selected area electron diffraction, SAED). For a single crystal, the distance in reciprocal space, r_{hkl}, between a particular reflection and the reflection from the direct beam (000) is related to the interplanar distance. Using the relation:

$$\frac{r_{hkl}}{L} = \tan 2\theta \qquad (2.16)$$

where L is the camera length of the TEM. By applying the small angle approximation (i.e. $tan2\theta = 2\theta$) and substitution with equations 2.15, gives us:

$$d_{hkl} = \frac{L}{r_{hkl}} \qquad (2.17)$$

The analysis of SAED can indicate structural information such as ferroelastic domains, exemplified by Figure 2.6. A DP for $BaTiO_3$ oriented along the [100] zone axis (determined by the Weiss Zone Law: hU+kV+lW=0) is shown in Figure 2.6. Evidence of ferroelastic domains can be seen due to the splitting of reflection spots [8, 9].
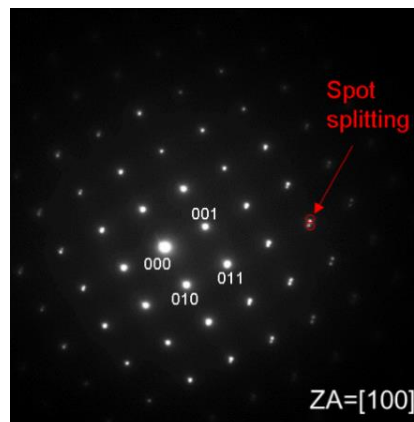
Figure 2.6: Electron diffraction pattern from $BaTiO_3$, oriented along [100].

2.4 Bright- and dark-field TEM

In conventional TEM operation mode, the electron beam is parallel (with respect to the column) when incident on the sample, such that both the diffracted and transmitted electrons contribute to the final image. However, by placing an objective aperture into the back focal plane it is possible to select the information in the image to the transmitted or specific diffracted beams. In bright-field (BF) imaging the objective aperature selects only the transmitted beam and all strongly diffracted regions in the sample appear dark (Figure 2.7a). In dark-field (DF) imaging, an objective aperture selects only one (or a few) diffracted beam without the contribution of the direct beam and this diffracted beam of electrons then appears bright in the DF image (Figure 2.7b). The contrast change due to bending or strain can also be interpreted in BF/ DF images since bending of atomic planes changes the Bragg condition. In BF imaging the intensity drops in regions with strain or bending and increases in the corresponding areas of the DF image.
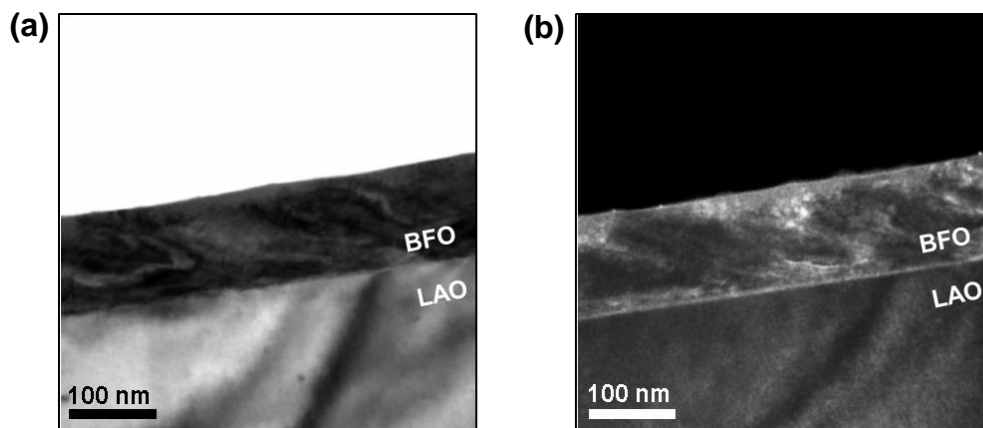
Figure 2.7: BF (a) and DF (b) image of a BFO thin-film on an LAO substrate. The DF image was acquired from the (002) reflection whilst the sample was oriented along $[100]_{pc}$ zone axis.

2.5 High Resolution TEM (HRTEM)

High resolution TEM (HRTEM) or phase contrast imaging is useful for visualising the crystallinity of samples in real space rather than reciprocal space (diffraction mode). For HRTEM a large objective aperture is used to select many beams, including the direct and diffracted beams to form the image. As electron waves interact with the sample, their phase may change relative to the unscattered wave; the resulting interference of these waves gives rise to contrast in the image with periodicity of the crystal lattice, known as *lattice fringes* (see example in Figure 2.8). The sample must be oriented along a zone axis so that the crystal lattice can be visualised from the lattice fringe spacing. Although this provides useful information, caution is necessary when interpreting HRTEM images as the image will reproduce the periodicity of the crystal structure but the atom positions do not necessarily correlate with regions of high or low intensity. In addition, the image resolution is heavily influenced by the thickness of the sample (the thinner the better!) and aberrations in the objective lens, defocus and astigmatism. Due to these reasons, phase contrast images are not used in this thesis to gain quantitative information about crystal structure (diffraction is used instead) but are rather used as a preliminary indication of interface effects (existence of dislocations or phase changes) and for initial strain analysis.

Geometrical Phase Analysis (GPA) can give a quantitative local measurement of strain from a HRTEM image (although caution must also be applied if thickness variations are present in the sample). Using an area of non-strained crystal lattice in the image as a reference, the image FFT will display sharp bright spots. By comparing the FFT of the reference area to that of the rest

of the image, local variations in lattice parameter can be quantitatively measured (without measuring the absolute lattice parameter values) by measuring the distance between the bright spots in the FFT to the slightly diffuse spots which originate due to areas which show strained lattices. These variations can be measured vertically, horizontally and diagonally to give the respective out-of-plane, in-plane and shear strain within the image (ε_{yy}, ε_{xx} and ε_{xy}) and are reflected by a colour intensity scale (given by a percentage relative to the unstrained reference lattice), see examples of GPA used to visualise the strain in mixed-phase BFO thin-films in Chapter 5.
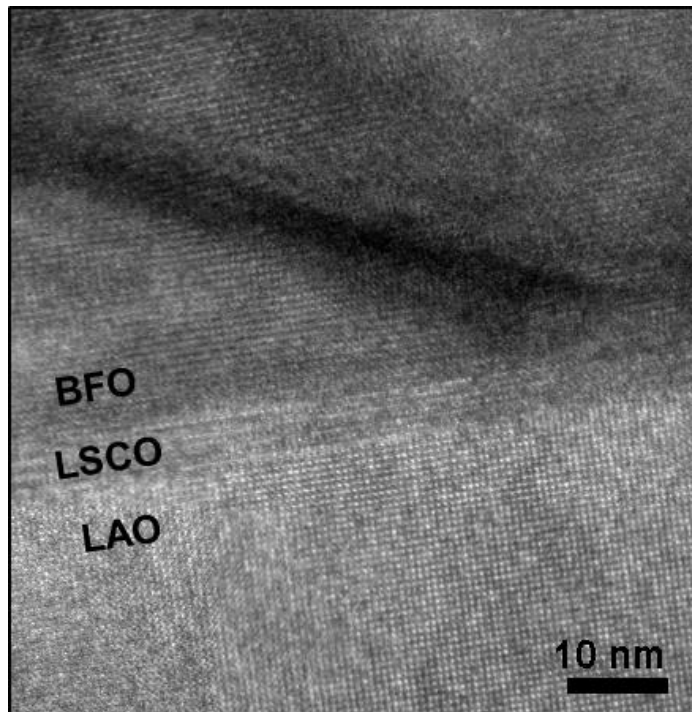
Figure 2.8: HRTEM image of a mixed-phase BFO thin film on a LAO substrate, with 5nm thick LSCO bottom electrode layer. The lattice fringes are visible, allowing the crystal lattice to be visualised along the $[010]_{pc}$ ZA.

2.6 Scanning TEM (STEM)

Whilst in TEM mode the convergence angle is small, leading to a parallel electron beam, in scanning TEM (STEM) mode the beam is converged (with a maximum convergence angle) to a small electron probe. The probe scans across the sample forming an image in series, pixel by pixel, collected as a function of the position of the probe position on the sample. Due to the raster (scanning) of the probe, image acquisition is slower than in TEM and must be acquired using different detectors, therefore the objective and projector lenses do not play a role in STEM image acquisition. Here, the resolution is governed by the size of the electron probe (smaller is better), the beam current (higher is better) and any aberrations (none is better) present in the condenser lens.

The various detectors used in STEM are summarised in Figure 2.9. Bright field images are acquired using a BF detector collecting electrons within a semiangle of 10mrad from the optical axis. A DF detector is an annular scintillator (shaped like a doughnut) and collects electrons between 10-50 mrad, constructing an image which is typically called an annular dark field (ADF) image. At even higher semiangles (>50 mrad) a high angle annular dark field (HAADF) detector is used, which collects electrons which have been inelastically scattered at high angles due to Rutherford scattering. In Rutherford scattering the angle through which the electron is scattered depends on the size of the nucleus of the atom, meaning that for heavier atoms (higher atomic no., Z), electrons will be scattered to higher angles. HAADF images show no or very little diffraction contrast, since the inner cut-off angle of the detector is so large that diffracted electrons do not

reach it. For a HAADF detector with a fixed collection semiangle, θ, the number of electrons collected will be:

$$N(\theta) \propto Z^2 \qquad (2.18)$$

Therefore, HAADF STEM images can also be called 'Z-contrast' images, heavier atoms will scatter more, generating more signal and hence appearing brighter in the image relative to lighter atoms. Electron channelling plays an important role in STEM imaging. When the electron probe is located over an atomic column in a crystal which is oriented on zone axis, the electrons are to some extent trapped by the attractive potential of the atoms. This effect maximises the signal and makes the atomic column appear brighter than an identical atomic column that is not oriented on zone axis. While STEM is a separate mode within TEM, dedicated STEM systems with no conventional TEM mode also exist (e.g. Nion UltraSTEM 100: microscope used to collect data in Chapter 4). Using a converged scanning beam in STEM mode is also useful for analytical techniques such as energy dispersive X-ray spectroscopy (EDX) and electron energy loss spectroscopy (EELS).

Figure 2.9: Schematic of detectors used in STEM mode. From [2]

2.7 Energy dispersive X-ray Spectroscopy (EDX)

When a high-energy electron is incident on the sample, an electron from the inner shell of an atom may be ejected, leaving a hole. Electrons from a higher-level shell will drop down to fill this inner shell hole and in doing so will emit a photon of an energy which is equal to the difference in energy of the two shells (see Figure 2.10a). The emitted photon is typically within the X-ray frequency region of the electromagnetic spectrum, and the process of detecting X-rays in electron microscopy is called electron dispersive X-ray spectroscopy (EDX or EDS). A measure of the X-ray energy can be used as a 'finger-print' of individual elements as the difference in atomic energy levels is unique to a particular element, X-rays produced in this way are known as 'characteristic X-rays'. Another type of X-ray production exists, which is always present alongside characteristic X-rays (see
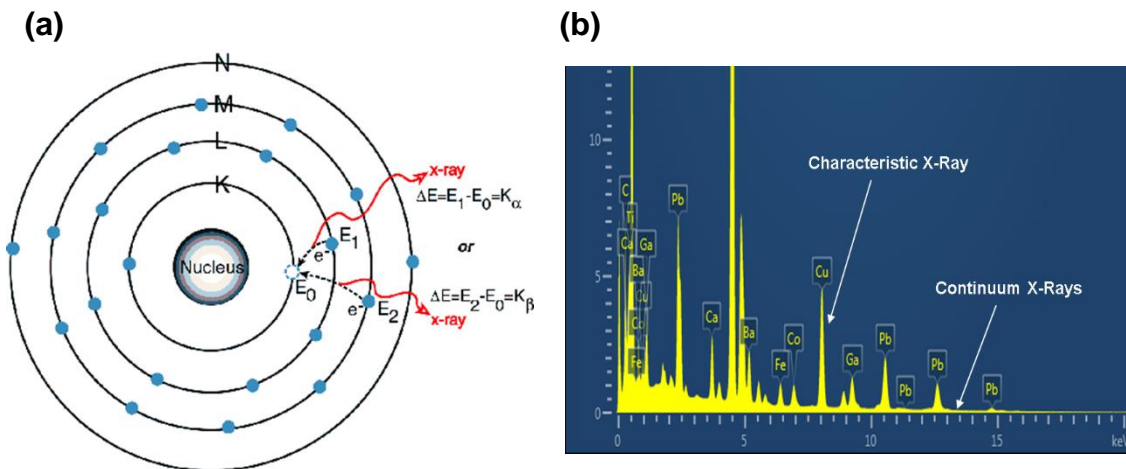
Figure 2.10: EDX. Schematic of atomic energy levels showing the transitions which give rise to characteristic X-ray production (a). From [10]. An example EDX spectrum displaying continuum X-rays and characteristic X-rays labelled with their corresponding elemental symbols (b).

experimental spectrum in Figure 2.10b) known as 'continuum' or 'Bremsstrahlung' X-rays, they result from the incident electrons interacting with the coulomb field of the nuclei of the atoms. The incident electron loses energy on interaction and this is given off as a continuum X-ray (seen mostly as a nuisance to microscopists because the characteristic X-rays used for elemental mapping need to be distinguished from the continuum X-rays).

EDX has several limitations, one being that the element detection is best used for heavy elements. This limitation comes from the detector itself; before 1980 detectors used to have a window made from beryllium (Be) and therefore only high energy X-rays could pass through the window [11]. Modern EDX detectors now have an ultrathin or windowless detector, allowing the detection of light elements down to Boron (Z = 4), however, the limited energy resolution of the EDX detector can lead to peak-overlap problems. An example of peak-overlapping is demonstrated in Figure 2.11, leading to the apparently identical EDX maps for two elements under investigation. Peak overlapping in EDX can be resolved with caution by using complex deconvolution procedures [11] which involve having good statistics and knowing a precise measurement of the local thickness of the sample. It takes a finite time for the detector to process each X-ray and during that time another X-ray cannot be recorded, this is called 'dead time'. If the arrival rate of the X-rays is too high, the dead time will approach 100%, allowing no X-rays to be recorded. Improving the energy resolution of the detector can reduce peak overlapping but this requires longer processing times, again at the expense of increased dead time and possible sample damage.
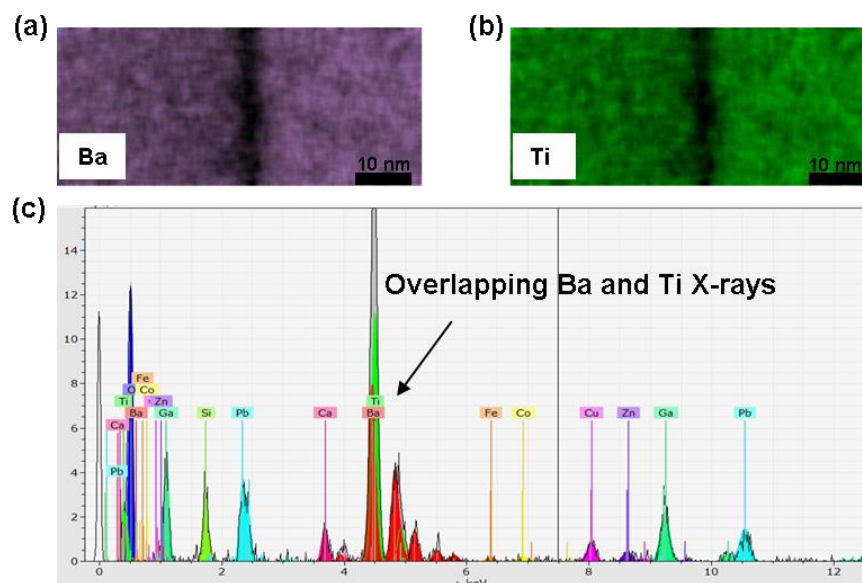
Figure 2.11: STEM-EDX demonstrating the effect of characteristic X-ray peak overlapping. Ba-$L\alpha$ (a) and Ti-$K\alpha$ (b) EDX maps appear to have identical elemental distributions, both showing a decrease in X-ray counts (dark contrast) along the grain boundary which is situated vertically along the centre of each map. The EDX spectrum (c) shows that the Ba-$L\alpha$ peaks and the Ti-$K\alpha$ peaks have overlapping energies making them undistinguishable in the maps (a) and (b).

2.8 Electron Energy Loss Spectroscopy (EELS)

Electron energy loss spectroscopy (EELS) is a very powerful technique because it detects any loss of energy by the incident electrons, not just a fraction of the inelastic scattering measured by EDX (which only measures when an X-ray is emitted and is within the collection angle of the detector). Above all, EELS is more sensitive to light (low Z) elements making it preferential for analysing elements such as oxygen which is the common element in the ferroelectric perovskites

studied in this thesis. EELS data is collected using a spectrometer added to the end of the STEM optical axis. When the electrons enter the EEL spectrometer, they are separated by energy based on their radius of curvature in a magnetic field and imaged by a charge-coupled device (CCD) [12]. As a result, the image on the CCD has one large bright peak corresponding to the non-scattered and elastically forward scattered electrons known as the zero-loss peak (ZLP), and satellite peaks corresponding to the elemental peaks with higher energy loss. This data can be plotted as the energy lost by an incident electron against its relative frequency, producing an energy loss spectrum. The EEL spectrum (see example in Figure 2.12) can be divided into two main energy ranges for analysis:

1. The *low-loss energy region* which includes transitions below electron energy losses of 50 eV. This region includes:

    a. The zero-loss peak (ZLP). The full width half-maximum (FWHM) of the ZLP can be taken as a measure of the spectral resolution, this can be as low as 15 meV with the latest monochromatic Nion 'HERMES' at SuperSTEM: the EPSRC National Facility for aberration corrected STEM.

    b. Plasmon peaks. In the energy range of around 10-15 eV, the plasmon peaks arise from collective, resonant oscillations of the valence electrons and can be utilised along with the ZLP to determine the local thickness, t, of the sample:

$$t = \lambda \frac{I_p}{I_0} \qquad (2.19)$$

where λ is the plasmon mean free path, I_P and I_0 are the intensities of the first plasmon peak and ZLP, respectively.

c. Interband transitions. The interaction of the electron beam can in some incidences excite valence electrons to the conduction band, producing characteristic peaks in the low energy loss region, allowing the band gap of some elements in the sample to be obtained.

2. The *core-loss energy region* which includes all transitions above 50 eV energy loss. This energy range contains more specific information about the electronic structure, chemical bonding and density of states (DOS) of elements within the sample. Peaks within the core-loss energy range are mainly caused by the inelastic electron interactions within core shells of the atoms, and because the binding energy of core electrons is dependent on the atomic no. each element has a unique ionisation edge energy onset in the energy loss spectrum. The excitation of electrons from the core shells gives rise to *K*, *L*, *M* and *N* edges, originating from initial sates with quantum numbers n=1,2,3 and 4. For example, the excitation of a *1s$_{1/2}$* state *K* shell electron gives rises to a single *K* edge, while the *L$_{2,3}$* edge arises from excitations of *2p$_{1/2}$* and *2p$_{3/2}$* electrons into unoccupied states. For heavy elements, it is more ideal to use the lower energy (L or M) ionisation edges for analysis, because the higher the atomic number, the more energy is required to excite electrons from the inner core shells as they are more tightly bound to the nucleus.
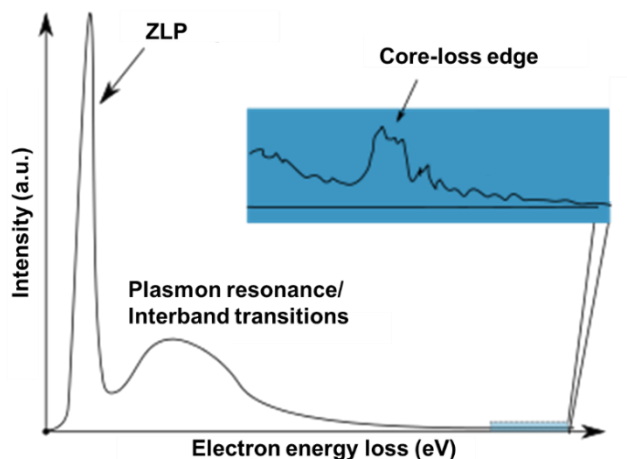
Figure 2.12: Schematic illustration of a typical EEL spectrum. The low-loss energy range shows the ZLP and plasmon resonance and interband transitions. The high-energy core-loss energy region shows a characteristic core-loss edge and extended post-edge structure. Adapted from [13].

2.8.1 Energy-loss near-edge structure (ELNES)

Core-loss edges are the most intriguing features in the EEL spectrum because they contain a wealth of information about the chemical composition of an element within the sample. The spectral features within 50 eV above the edge onset are called the energy-loss near-edge structure (ELNES) of the element, the shape and intensity of the ELNES provides information about the local atomic environment of the atom as well as the DOS. The most distinguished ELNES feature in transition metals is the "white lines", which occur due to spin-orbit coupling. They appear as intense sharp peaks in the EEL spectrum, an example of the $L_{2,3}$ white lines of Ti is shown in Figure 2.13a. As mentioned in Chapter 1, the ferroelectric phase of a perovskite involves the polar distortion of the unit cell which includes a shift of the central cation and distortion of the oxygen octahedra.

The ELNES of the central cation (Ti in the case of $BaTiO_3$) is therefore very sensitive to these changes, and so the Ti-$L_{2,3}$ edge along with the O-K edge (example shown in Figure 2.13b) are often used to understand the relation between local atomic environment, electronic structure and polarisation in ferroelectric materials.

After acquisition of the EEL spectrum, and before the ELNES can be usefully interpreted, further processing is required. Firstly, the continuous decaying background must be removed; this can be done using a power law model [11], followed by the integration of the intensity of the core-loss edges over a suitable energy window (typically 40 eV) beyond the edge onsets. If the sample is relatively thick (greater than t/mean free path=0.5 was used as the cut off in this thesis) then the spectra should also be treated for multiple scattering effects. To remove multiple scattering effects, the EEL spectrum needs to be deconvoluted from the low-loss region of the EEL spectrum to obtain a single scattering
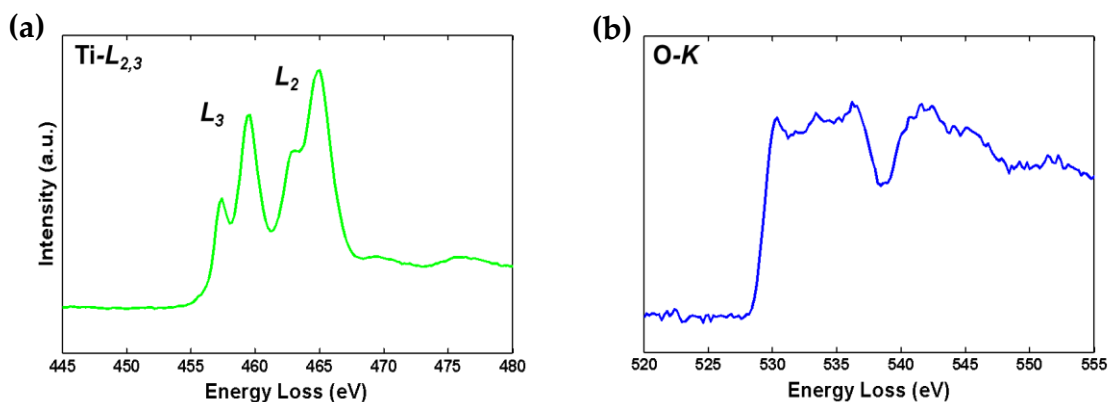
Figure 2.13: Example EELS edges. (a) Ti-$L_{2,3}$ edge and (b) O-K edge. The L_3 and L_2 edge ("white lines") are labelled in (a).

spectrum. There are two commonly used deconvolution procedures: Fourier Log and Fourier Ratio. The EELS data presented in Chapter 4 of this thesis was acquired on samples below the thickness threshold for treatment of multiple scattering effects. However, the EELS data in Chapter 5 was acquired on thicker samples (reasons explained within the chapter) and therefore the Fourier Ratio method was used. This procedure is effective in removing multiple scattering but usually cannot eliminate the energy broadening of the spectrometer system because high-frequency spectral noise becomes amplified during the Fourier division [14].

A recently developed method to reduce the noise in EEL spectra is to use principal component analysis (PCA), which is a form of multivariate statistical analysis. The software package ('Digital Micrograph Plugin for Multivariate Statistical Analysis' [15]) used in Chapter 5 of this thesis separates the data into components of variables in the form of a *scree plot*. By selecting only the components which have high eigenvalues (the noise is represented by an exponential decrease of the eigenvalues), the data is reconstructed and the resultant EEL spectrum map has a significantly improved signal/noise ratio.

Similar to EDX, EELS unfortunately has its own limitations, the main one being the effect of energy resolution and how this determines the amount of information that can be obtained from ELNES analysis. Energy resolution can to some extent be improved with thinner samples (t/mean free path< 0.5) but, more significantly it can be improved with the use of a cold-FEG (see data in Chapter 4) or using a monochromator to correct for C_c aberrations.

It should be noted that using higher voltages (200 − 400 kV) can in principle increase resolution, however, it can also generate beam damage as the probe rasters across the sample. If the sample suffers from contamination (e.g. carbon build up), the thickness of the sample will rapidly increase deeming the additional processing step of removing multiple scattering necessary.

2.9 Nano-Beam Electron Diffraction (NBED)

The nano-beam electron diffraction technique used in Chapter 5 of this thesis involves using a quasi-parallel electron beam whose diameter at full width at half maximum (FWHM) is ~2 nm, with a convergence semi-angle of 0.5 mrad. The NBED technique [16] consists of rastering the quasi-parallel probe across the sample, resembling a combination of STEM and TEM modes, collecting diffraction patterns, pixel by pixel on the CCD. The shift of the diffracted spots within the diffraction patterns allows the measurement of the lattice parameter evolution in the sample and therefore the strain. NBED offers the advantage of being able to accurately map lattice parameter changes over a large area compared to similar techniques such as GPA, which maps lattice spacing in a very localised area of the sample and is more prone to inaccuracies due to thickness variations or defects.

The aim of NBED is to obtain good spatial resolution (using the small beam size), and sharp diffraction spots. Energy filtering (zero-loss) of the diffraction patterns with a 10 eV slit has been found to significantly improve the signal/ noise ratio creating sharp diffraction spots. An image of the 2 nm sized

probe and an example NBED pattern is shown in Figure 2.14. In terms of acquisition time, a map of NBED patterns of ~100 pixels with pixel size of ~2 nm took ~20 minutes. This may seem quite inefficient however, the strain accuracy can be estimated to be 6 x10^{-4} using this technique [16]. A dedicated script developed by CEA-Grenoble was used to process all recorded NBED patterns (see results in Chapters 5), detailed in Ref [15].
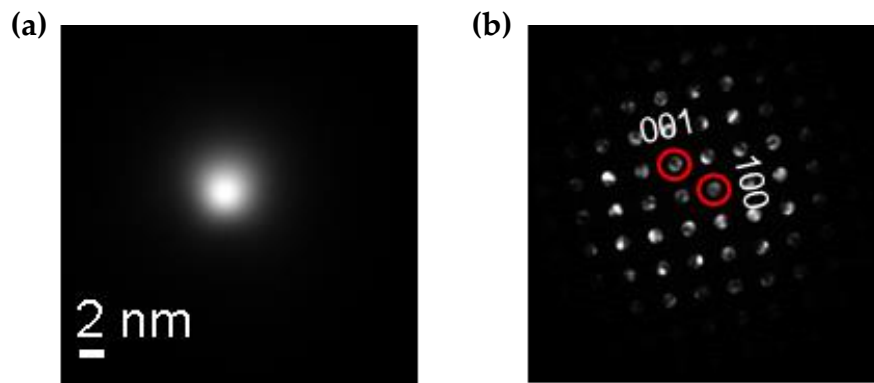
Figure 2.14: Image of the electron probe used for NBED (a). NBED pattern of LAO oriented along the [010]$_{pc}$ zone axis (b).

2.10 TEM Sample Preparation

TEM requires an electron-transparent sample with thickness ~<100 nm for conventional imaging and even thinner for carrying out high resolution imaging or spectroscopy techniques, especially EELS. Generally, for EELS the sample thickness should be less than half of the mean free path between plasmon scattering events (*mfp*) where mfp is dependent on the electron energy and is ~100 nm for metals and semiconductors at 100 keV [12]. For the TEM experiments carried out in this thesis, all samples were prepared as lamella (meaning "thin layer" in Latin) using a dual-beam (scanning electron microscope & focused ion beam) microscope. The focused ion beam microscope and scanning electron microscope within a dual-beam microscope will be described in the following sections.

2.10.1 Focused Ion Beam (FIB) microscope

Sample preparation by FIB is nowadays considered a routine procedure. However, care must be taken when selecting the operation parameters as to avoid as much damage and introduction of artefacts as possible. Thus, the instrumentation and procedures are continuously improving. FIB microscopes use a liquid metal ion source (LMIS) to produce ions (most commonly Ga^+) through field emission. The beam of Ga^+ ions is focused into an energetic beam using a series of electrostatic lenses, each ion has an energy related to the accelerating voltage (e.g. a 30 kV extractor will produce ions of 30 keV energy)

and the use of apertures can limit the current of the beam from μA to pA. Once incident on the sample surface, the Ga^+ ions will sputter material from both the surface and subsurface region via atomic collisions of the incident ion, shown schematically in Figure 2.15 where the Ga^+ ions penetration depth, R_P, and lateral range, R_L, are labelled. The sputtering process is very useful for fabricating thin sheets of electron transparent material (lamellae) suitable for TEM investigation. The smallest lamella thickness achievable in modern FIB microscopes (with very careful operation) is ~ 10 nm, ideal for single scattering EELS and high resolution
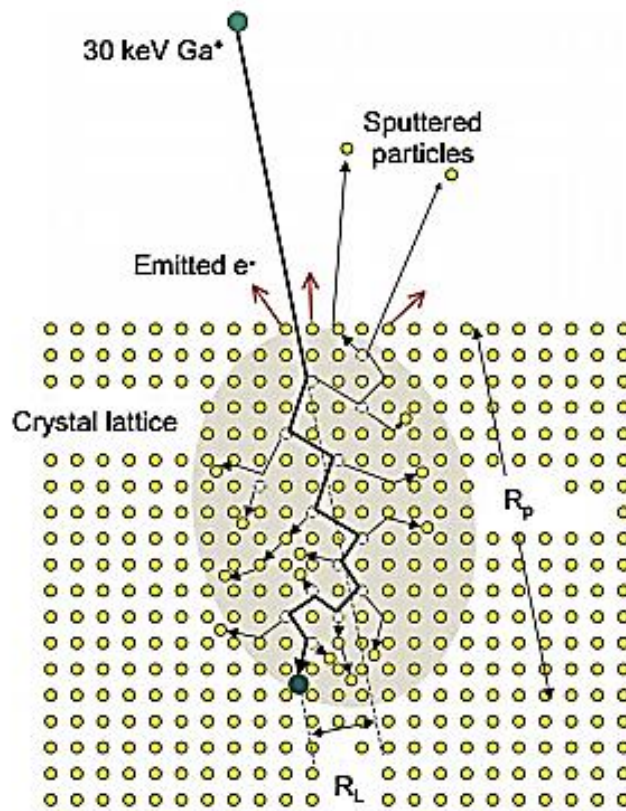
Figure 2.15: Schematic of the cascade volume created when a Ga+ ion interacts with a crystalline material during the FIB milling process. The crystallinity is broken down by atomic collisions with the incoming Ga+ ions. Adapted from [17].

experiments. However, caution is necessary when choosing the operating voltage and current of the beam to fabricate thin lamellae because the thickness of the damaged (amorphised) layer depends heavily on these parameters. Generally, for the lamellae fabricated in this thesis, a high extraction voltage (30 kV) and beam current (9 nA) was used to mill the initial trenches of the lamella and these parameters were lowered in succession until the final stage of "polishing" the lamella, where an extraction voltage of 5 kV and beam current of ~71 pA was used. In addition, the Ga^+ ions can breakdown gases containing Pt or W released within the vacuum chamber, allowing site-specific deposition. This is particularly useful for depositing a protective layer on the sample which decreases the thickness of the damaged layer on the top surface of the lamella. The main disadvantage of using FIB microscopes to prepare TEM samples is related to the destructive nature of the technique, where even sporadic/irregular imaging of the lamella during the milling process can greatly damage the lamella by creating Ga^+ implantation and crystal amorphisation in the lamella. Therefore, to reduce the extent of FIB damage a dual-beam FIB microscope was used to prepare TEM samples in this thesis. A dual-beam FIB microscope benefits from having both an ion beam microscope for milling and a scanning electron microscope to image the lamella in a less destructive manner.

2.10.2 Scanning Electron Microscope (SEM)

In a similar manner to TEM, a SEM operates by means of an electron gun at the top of the column which creates energetic electrons. The electrons are focused using a series of electromagnetic (rather than electrostatic in FIB) condenser lenses

to a spot size of ~1 nm on the sample, and the electron beam is rastered across the surface during operation. The signals produced by the electron beam-sample interactions are summarised in Figure 2.16, with imaging primarily carried out by the detection of secondary emitted electrons. The electron energies used for SEM (within a dual-beam FIB) are typically around 5 keV meaning that these electrons have low energy (in comparison to TEM), only interacting with a small interaction volume. The interaction volume can be increased with increased operating voltages and when incident on soft (low Z) materials, but in general, SEM obtains only surface-specific information from the detected signals.
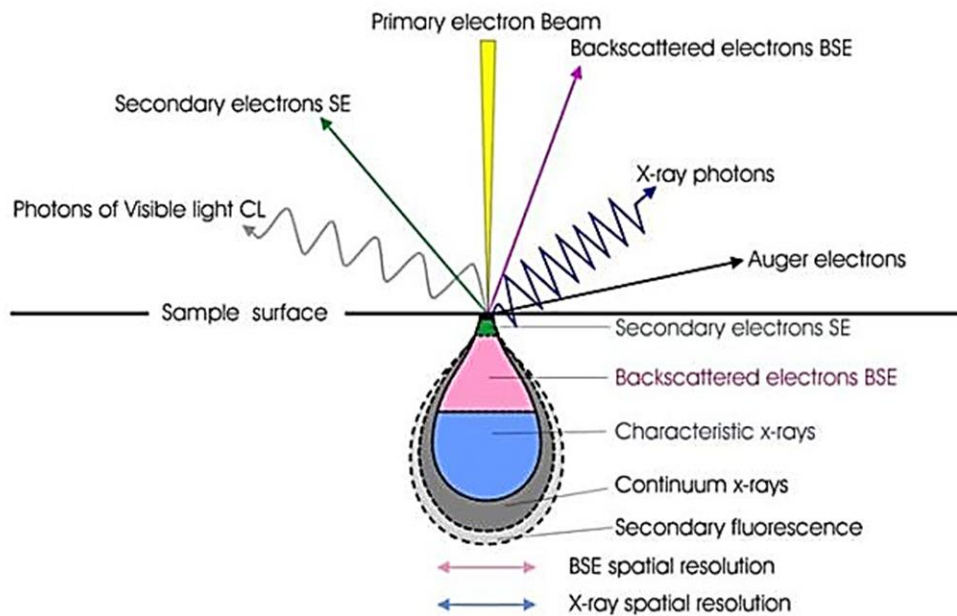
Figure 2.16: Schematic of the interaction volume and signals produced when electrons are incident on the surface of a material in an SEM. Imaging is primarily carried out by detecting secondary electrons or backscattered electrons. From [18].

2.10.3 Fabrication of TEM lamellae using a Dual-beam FIB Microscope

Preparation of TEM lamellae for preliminary data analysis was carried out using a FEI Nova 600 dual beam FIB at QUB. The Nova microscope (shown schematically in Figure 2.17) contains two separate columns, one for the ion and electron beam, respectively. Due to the design, the columns are separated by an angle of 52° but with careful alignment and setting of the sample eucentric height, both beams can be focused onto the same point of interest on the sample so that simultaneous milling and imaging can take place in a minimal-destructive manner. A standard procedure to fabricate TEM lamellae was used on the Nova microscope, this involved firstly depositing a W protective strip (~2 μm thick) on the surface of the desired site of the bulk sample. This step was followed by the milling of deep, wide trenches either side of the W strip, where the depth
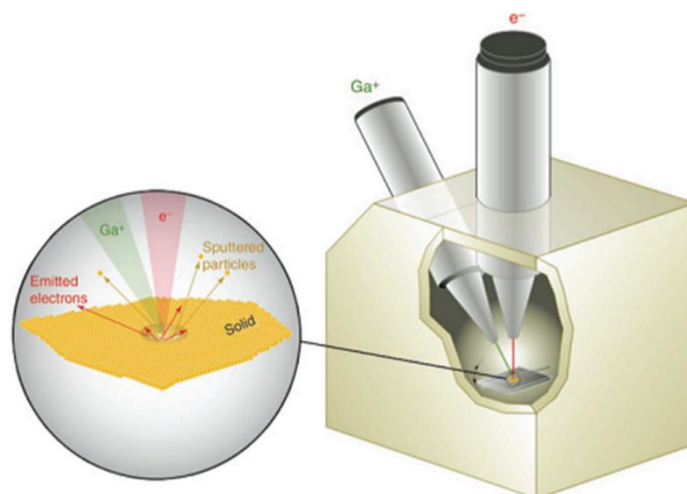
Figure 2.17: Schematic of a dual-beam FIB microscope. The central column (comprising the SEM) is separated by the ion beam column (comprising the FIB) by 52°. From [17].

determined the length of the lamella. After continuous milling (stepping down the voltage and current approx. every 250 nm) the lamella was ready to be cut free at the bottom and sides. The next step involved the delicate transfer of the lamella (now sitting free in between the trenches) to a TEM grid using the well-known ex-situ lift-out procedure [19]. The lamella was removed from the bulk sample by using a micromanipulator controlled glass needle (drawn to a fine point using a heating source), the electrostatic forces were sufficient to attach the lamella to the glass needle before placing it down onto a carbon membrane TEM grid.

Although sufficient for preliminary low magnification TEM investigation, the lamellae produced using this procedure (involving ex-situ lift-out) were inadequate for high resolution investigation (especially for low extraction voltage microscopes like the 100 kV Nion microscope used in Chapter 4). Instead, a different procedure which involved using an in-situ micromanipulator was considered necessary (these samples were fabricated in Leed's University (UK) and Ernst Ruska-Centre for Microscopy and Spectroscopy of Electrons (Germany)). The in-situ technique (meaning that the FIB milling and lift-out process both take place within the dual-beam microscope) was used to fabricate the lamellae investigated at the following advanced microscopy centres: SuperSTEM: The EPSRC National Facility for aberration corrected STEM (UK) and Ernst Ruska-Centre for Microscopy and Spectroscopy of Electrons (Germany), data presented in Chapters 4 and 5.

The in-situ technique, summarised in Figure 2.18, involved the removal of a thick (~1.5 μm) lamella from the trenches using an Omniprobe needle (made

from Pt and micromanipulated using electronics), followed by attachment to a specific type of grid to be mounted on; a Cu finger grid with no carbon membrane. Once removed from the trenches, the lamella was positioned within touching distance from the grid where it was then attached using Pt deposition, and further polished until the desired thickness was reached. The benefits of using the in-situ fabrication technique include the ability to re-thin the lamella if the desired thickness is not reached after the first FIB session (this includes using an argon source to give a final gentle clean). The fabricated lamellae are also less contaminated by re-deposition when using this technique because the majority of the FIB milling takes place outside of the trenches. Additionally, the absence of the carbon membrane on the omniprobe TEM grids means that there is less contamination during image acquisition (especially in STEM mode where carbon build up occurs quite rapidly as the probe is rastered across the sample, especially for oxides).
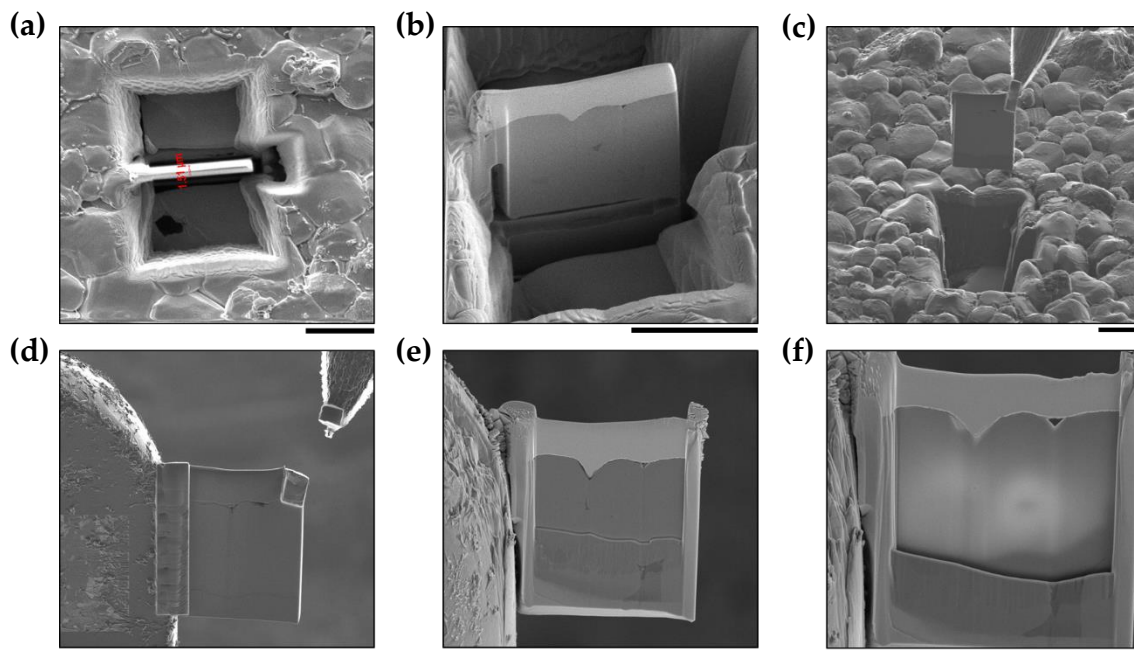
Figure 2.18: Example of FIB fabrication of a lamella using the in-situ technique. A Pt strip was deposited as a protective layer on the desired site and trenches were milled either side using high voltage (30 kV) and current (9 nA) (a). The lamella was tilted to 45° (with respect to the ion beam column) so that the bottom and one side of the lamella could be cut free (30 kV and 0.26 nA) (b). The in-situ needle was sharpened (milled by FIB) and attached to the free side of the lamella via Pt deposition. Once attached, the lamella was cut free on the remaining side and removed from the trench using micromanipulators (c). The lamella was brought into contact with the metal leg of the TEM grid and attached via Pt deposition. Once attached, the needle was milled free (d). The lamella was further milled, lowering the current in subsequent steps to 90 pA at ~200 nm thickness (e). The final polishing of the lamella was carried out at 5 kV and 71 pA until the lamella reached around ~100 nm thickness. The current was then further reduced to 17 pA until the thickness reached below 50 nm (measured from the top-down), some areas appear even thinner (bright contrast) in (f). All scale bars represent 10 μm.

2.10.4 MEMS chips for in-situ heat cycling experiments

The in-situ heat cycling experiments carried out in Chapters 3 and 5 of this thesis involved the use of MEMS (micro-electro-mechanical systems) chips for TEM. Lamellae were prepared using the standard FIB and ex-situ lift-out procedure previously described, meaning that the lamellae could be carefully positioned over the circular electron-transparent windows, as shown in Figures 2.19a and b.

Two types of MEMS heating chips were used for the investigations presented in this thesis: the in-situ heat cycling experiments on $BaTiO_3$ (Chapter 3) were carried out on chips produced by Protochips [20], while, the experiments on $BiFeO_3$ (Chapter 5) were carried out on chips produced by DENS solutions [21]. Both chips operate under the same principles, the passage of current through the chip produces heat via Joule heating. In the design of Protochips, the chip features a silicon carbide heater (which is integrated into the membrane itself so that the heater and sample-support is within a single thin film) with W electrodes that allow heating up to 1200 °C.

The DENS solutions chip has a slightly different design; instead of using a semiconductor membrane, it features a metal heater (exact metal not disclosed) in the shape of a coil. The heater lines are encapsulated in silicon nitride so that the sample is insulated from the heater and a thin carbon membrane coats the chip so that the lamella stays in place. Both Protochips and DENS solutions benefit from the 4-point-probe measurement system (shown in Figure 2.19c) where a voltage is applied to two of the contacts and the other two contacts accurately measure the resistance. The well-defined relationship between resistance and temperature for a semiconductor-based (Protochips) and metal-

based (DENS solutions) heating element is shown in Figure 2.19d. Each chip is calibrated separately at the final stage of production and a table of resistance vs. temperature is provided within the software which operates the MEMS chips. The temperature is regulated 3 times per second via the closed-loop feedback from the 4-probe design, ensuring accurate temperature control throughout.

In terms of tilt-ranges available for MEMS heating chips, both companies now have holders with double-tilt capabilities available (α and β tilt ~ ±25°). However, during the first set of experiments carried out in this thesis ($BaTiO_3$ in Chapter 3) only the single-tilt Protochips holder (α ±25°) was available (the technique was, and still is, relatively new!). Although the limited tilt range did not diminish the impressive heating stability provided during the experiments, the ability to tilt the $BaTiO_3$ crystal onto a main zone axis was unfortunately severely limited, as will be shown in the discussion of results in Chapter 3.
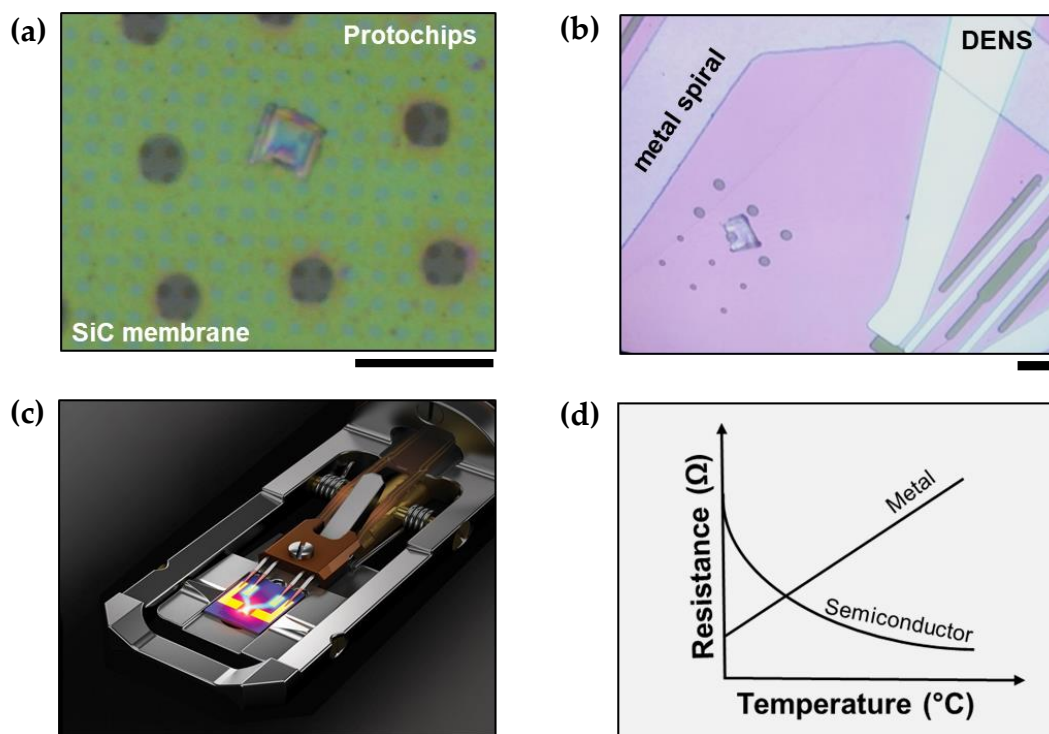
Figure 2.19: MEMS chips for in-situ heating with the TEM. Optical microscope image of the Protochips heating chip featuring a silicon carbide membrane heating element with circular holes, the lamella was placed over one of the larger circular electron-transparent windows using a glass needle (a). Optical microscope image of the DENS solutions heating chip featuring a metal spiral heating element which is encapsulated in silicon nitride, the lamella was placed over one of the circular electron-transparent windows, the thin layer of carbon which coats the chip kept the lamella in place (b). Photograph of a Protochips double-tilt holder with a MEMS heating chip inserted [20], four metal contact probes were present: two applied voltage and two measured the resistance (c). The typical relationship between resistance and temperature for a semiconductor (silicon carbide membrane in (a)) and metal (coils in (b)) heating element (d). Scale bars in (a) and (b) represent 20 μm.

2.11 Other techniques

2.11.1 Atomic Force Microscopy (AFM)

Atomic force microscopy (AFM) is a type of scanning probe microscopy (SPM) which can provide micron lateral-scale maps of surface topography with nanometre resolution [22]. Information is gathered by scanning a metal tip (probe) along the surface of the sample using piezo-tube actuators, allowing for precise movements in all directions. The position of the probe can be detected using a laser spot focused on the probe backside and the reflection is detected by a photodiode detector [23]. The AFM can operate in a number of different modes due to the dependence of force interactions on the tip-surface separation (e.g. contact or non-contact mode). The following modes of AFM were used within the work of this thesis: Piezoresponse force microscopy, conductive-Atomic force microscopy and Kelvin probe force microscopy. The AFM experiments were carried out by collaborators at QUB (special thanks to Dr. A. Douglas, N. Browne and D. Edwards) and a brief description of the techniques used will be described in the sections which follow.

2.11.1.1 Piezoresponse Force Microscopy (PFM)

Piezoresponse force microscopy (PFM) is a surface-based technique which is non-destructive (un-like the sample preparation necessary for TEM) and has been the source of the most recent experimental advances in ferroelectric switching of domains [24, 25]. PFM works by measuring the (converse) piezoelectric response

of the ferroelectric to an applied bias via the deflection of a conductive tip in contact with the surface. For imaging domains, the reaction of the probe to the forces that the sample imposes on it can be used to form an image of the topography of the sample [23]. Noting that ferroelectric domains respond to an electric field with a characteristic deformation (strain), in PFM an AC signal is applied to the conductive tip (which acts as a movable top electrode) and in the simplest case the vertical (z-direction) surface strain is recorded by measuring the amplitude and phase of the periodic response of the ferroelectric, transferred to the cantilever (shown schematically in Figure 2.20) [26].
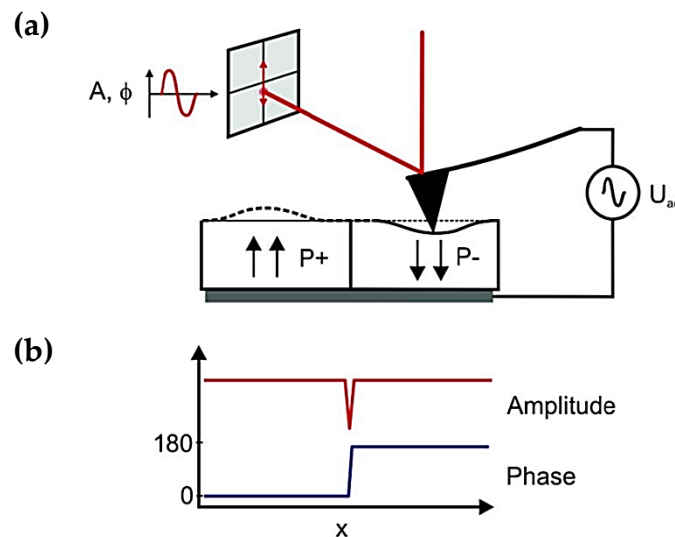
Figure 2.20: Schematic of the setup of PFM (a). The ferroelectric material has a bottom electrode painted on with Ag paste. An AC voltage is applied to the tip (top electrode) and the domain orientation which gives an in-phase response for P+ and out-of-phase response for P- domains are recorded relative to the modulated bias (b). The amplitude is independent of the domain polarisation, if the size and depth remains the same. From [26].

2.11.1.2 Conductive-Atomic Force Microscopy (c-AFM)

Conductive atomic force microscopy (c-AFM) is a mode in AFM that simultaneously measures the topography and the electric current flow at the contact point of the tip with the surface of the sample. The current is measured using a current-to-voltage preamplifier while the topography is measured using the cantilever optical system shown in Figure 2.20. The c-AFM is usually operated in contact mode so that the tip can be kept at one location while the voltage and current is read, or the tip can scan a specific region of the sample under constant voltage while the current is measured [27, 28].

2.11.1.3 Kelvin Probe Force Microscopy (KPFM)

Kelvin probe force microscopy (KPFM) also known as 'surface potential microscopy' is a noncontact mode in AFM based on the detection of electrostatic forces. If the tip encounters a surface charge while scanning, it will begin to oscillate. The KPFM is setup with a feedback system to dampen the cantilever's oscillation through the variation of the DC voltage applied. Recording this dampening voltage signal gives a direct measure of the surface potential. KPFM can therefore create a map of local potential as the tip is rastered across the sample surface [29, 30].

2.11.2 Electron Backscatter Diffraction (EBSD)

Electron backscatter diffraction (EBSD) is a technique used with the scanning electron microscope. EBSD provides quantitative microstructural information about materials and is ideal for revealing the crystallographic orientation of crystals within a bulk material (e.g. the orientation of specific grains within a bulk polycrystalline sample) before sample preparation for TEM investigation. EBSD was made available (via collaboration with the University of Manchester) during the late stages of the TEM studies in this thesis, but the benefits for future studies, especially in relation to the study of domains in polycrystalline barium titanate, are highlighted in Chapter 3.

EBSD works by positioning a flat (highly polished) sample at angle of 20° to the electron beam; the SEM is operated at ~20 kV and incident beam currents of ~50 nA. When the primary beam interacts with the crystal lattice low energy loss backscattered electrons are channelled and are subject to path differences that lead to constructive and destructive interference. By placing a phosphor screen a short distance from the sample (see schematic in Figure 2.21a) in the path of the diffracted electrons, a diffraction pattern can be seen (known as the electron backscattered pattern (EBSP)) [31]. The EBSP is in the form of black and white Kikuchi lines (previously described in Section 2.2), an example of an EBSP from a grain within a polycrystalline $BaTiO_3$ sample is shown in Figure 2.21b. By scanning the electron beam across the surface of the sample (which has cm dimensions), EBSPs can be collected from each neighbouring grain on the surface of the sample and a resultant EBSD map can be created. The EBSD map can be colour coded for each grain in terms of its crystallographic orientation using the

Euler angle convention [32]. During a measurement, this is the relationship between the EBSP detector and the particular point on the sample being measured under the beam; an example EBSD map for polycrystalline $BaTiO_3$ is shown in Figure 2.21c.
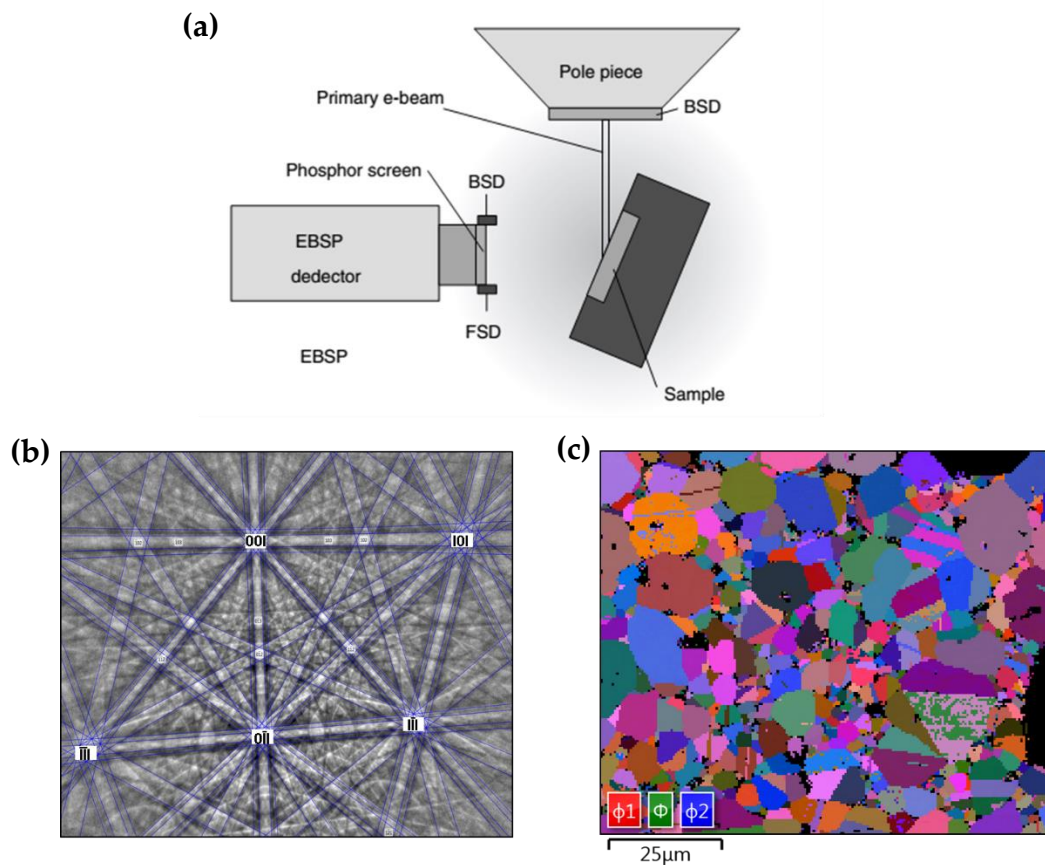
Figure 2.21: EBSD technique. Schematic arrangement of the sample orientation in the SEM (a). From [31]. Example EBSP from a grain of $BaTiO_3$, the main zone axes are labelled (b). Example EBSD map created by scanning the electron beam across the surface, collecting EBSPs at each point. The map is colour coded in terms of the corresponding Euler angles shown in the bottom left (c).

2.12 References

[1] T. Frangsmyr, Ed, *Nobel Lectures, Physics 1981-1990*, World Scientific Publishing Co., Singapore **1993**.

[2] D. B. Williams, C. B. Carter, *Transmission Electron Microscopy A textbook for Materials Science*, Plenum Press, New York **1996**.

[3] J. Sloan, Online Lecture Notes, The University of Warwick, **2014**.

[4] R. Brydson, *Aberration-Corrected Analytical Transmission Electron Microscopy*, John Wiley & Sons, Ltd, U.K. **2011**.

[5] Online notes on TEM, The University of Iowa,
https://cmrf.research.uiowa.edu/transmission-electron-microscopy

[6] Q. Ramasse, Lecture notes from the CCEM Summer School in Electron Microscopy, **May 2015.**

[7] O. L. Krivanek, J. P. Ursin, N. J. Bacon, G. J. Corbin, N. Dellby, P. Hrncirik, M. F. Murfitt, C. S. Own, Z. S. Szilagyi, *Philosophical Transactions of the Royal Society A-Mathematical Physical and Engineering Sciences.* **2009**, *367*(1903), 3683-3697.

[8] X. Huiping, L. Qi, S. Guangjun, W. Luchun, S. Zhenshun, Z. Jianming, F. Duan, W. Jiyang, **1993**, *10*(5), 298.

[9] S. Cheng, N. Ho, H. Lu, *J Am Ceram Soc.* **2006**, *89*(7), 2177-2187.

[10] Online notes on X-rays, Ametek Materials Analysis Diviesion, http://chemphys.u-strasbg.fr/mpb/teach/daniel/Projet/$mecafluox.htm

[11] R. F. Egerton, *Electron Energy-Loss Spectroscopy in the Electron Microscope*, Third edn., Springer, New York **2011**.

[12] B. Fultz, J. Howe, *Transmission Electron Microscopy and Diffractometry of Materials*, Third edn., Springer, Berlin, Heidelberg, New York **2008**.

[13] EELS online notes:
https://en.wikipedia.org/wiki/Electron_energy_loss_spectroscopy

[14] R. F. Egerton, F. Wang, M. Malac, M. S. Moreno, F. Hofer, *Micron.* **2008**, *39*(6), 642-647.

[15] G. Lucas, P. Burdet, M. Cantoni, C. Hebert, *Micron.* **2013**, *52-53*, 49-56.

[16] A. Beche, J. L. Rouviere, J. P. Barnes, D. Cooper, *Ultramicroscopy.* **2013**, *131*, 10-23.

[17] C. A. Volkert, A. M. Minor, *MRS Bull.* **2007**, *32*(5), 389-395.

[18] Online SEM notes, ISAAC: Imaging Spectroscopy and Analysis Centre, http://www.gla.ac.uk/schools/ges/researchandimpact/researchfacilities/isaac/services/scanningelectronmicroscopy

[19] L. A. Giannuzzi, Z. Yu, D. Yin, M. P. Harmer, Q. Xu, N. S. Smith, L. Chan, J. Hiller, D. Hess, T. Clark, *Microscopy and Microanalysis.* **2015**, *21*(4), 1034-1048.

[20] Protochips website: http://protochips.com/products/fusion/#1463264736106-fa512f54-9c27

[21] DENS solutions website: http://www.denssolutions.com/products/heating/nano-chip/

[22] Y. Seo, W. Jhe, *Reports on Progress in Physics.* **2008**, *71*(1), 016101.

[23] L. J. McGilly, *QUB PhD Thesis*, "Domain Topologies in Nanoscale Single-Crystal Ferroelectrics", **2011.**

[24] J. R. Whyte, J. M. Gregg, *Nature Communications.* **2015**, *6*, 7361.

[25] R. G. P. McQuaid, M. P. Campbell, R. W. Whatmore, A. Kumar, J. M. Gregg, *Nature Communications.* **2017**, *8*, 15105.

[26] Online Notes, *Technical Note on PFM by* JPK Instruments, *www.jpk.com.*

[27] *"Nanoscale phenomena in ferroelectric thin films"*, Ed. S. Hong, Springer Science+Business Media, New York **2004**.

[28] M. P. Campbell, J. P. V. McConville, R. G. P. McQuaid, D. Prabhakaran, A. Kumar, J. M. Gregg, *Nature Communications.* **2016**, *7*, 13764.

[29] T. Melin, M. Zdrojek, D. Brunel, *Scanning Probe Microscopy in Nanoscience and Nanotechnology*, **2010** 89-128.

[30] A. M. Douglas, QUB PhD Thesis, *"Establishing the role of ferroelectric interfaces on nanoscale current and potential distributions"*, **2016.**

 [31] T. Maitland, S. Sitzman, in *Scanning Microscopy for Nanotechnology Techniques and Applications* (Eds: W. Zhou, Z. L. Wang), Springer **2007**, pp. 41-75..

[32] T. B. Britton, J. Jiang, Y. Guo, A. Vilalta-Clemente, D. Wallis, L. N. Hansen, A. Winkelmann, A. J. Wilkinson, *Mater Charact.* **2016**, *117*, 113-126.

3. Domain compatibility across BaTiO$_3$ grain boundaries

In this chapter a study of domain patterns and compatibility of domains across grain boundaries is presented, exploring whether domains within individual grains of a polycrystalline ceramic behave in a similar way to single crystals, or whether they can couple across grain boundaries in a stress-free manner. The arrangement, or pattern, of domains present in a ferroelectric is of great significance in determining the properties of a material at the nanoscale [1-6]. For instance, the effective piezoelectric coefficients depend upon the fractions of different domains types present [7], and enhanced actuation can be achieved by engineering specific domain patterns [2]. Polycrystalline ferroics remain in widespread use in the technology industry (in actuators and sensors) due to their low-cost and fast preparation time scales, on par with higher quality single-crystal counterparts when possible. However, the intricate domain patterns

which form in polycrystals are not well understood and thought to be a difficult and unsolved problem at the present [8]. Therefore, it is of high scientific and technological importance that a good understanding of domain compatibility across grain boundaries is achieved to optimise the use and practical control of domain configurations for future technological applications. In this study, scanning transmission electron microscopy (STEM) was used to image the ferroelastic domain patterns which occur within grains and near grain boundaries in lamellae cut from a BaTiO₃ ceramic. Moreover, STEM in-situ heat cycling experiments were carried out to explore the new domain arrangements produced by heating and subsequent cooling of lamellae through T_C. The study within this chapter demonstrates that the domain arrangements near grain boundaries, can be rationalised in terms of the theory of martensite crystallography. If experimentally confirmed assumptions are undertaken, such as if the grains are pancake-like, with grain size significantly greater than the lamella thickness, then the relaxation of the out-of-plane strain gives rise to an undetermined set of linear equations in the volume fractions of domains. Interestingly, additional inequality constraints on the volume fractions lead to (non-unique) solutions, demonstrating that groups of adjacent grains in lamellae can form compatible stress-free domain arrangements across grain boundaries.

The work in this chapter was carried out in collaboration with Dr. E. Prestat and Dr. S. Haigh at the University of Manchester, where STEM in-situ heating experiments were performed. Following this set of experiments, the analysis of grain boundary domain arrangements in relation to the theory of martensite crystallography was carried out in collaboration with Prof. J. Huber from the University of Oxford.

3.1 Morphology of domains in polycrystalline ceramics

While domain formation in single crystal ferroic materials is relatively well understood, the morphology of domains in polycrystalline materials is much more complex. In fact, for many years it had been assumed that domain walls were confined within grains, and could not penetrate grain boundaries [9]. This was fully disproved when evidence of ferroelectric domains was shown overlapping adjacent grains in $Pb[Zr_xTi_{1-x}]O_3$ [10]. More recently, evidence has shown that domains can spontaneously nucleate at grain boundaries and the macroscopic polarisation distribution can be correlated across neighbouring grains [11]. Gruverman et al. verified this experimentally using piezoresponse force microscopy (PFM) [12, 13]. Furthermore, it has been shown that grain boundaries can act to pin domain walls [14-17]; x-ray diffraction has shown ferroelastic domain wall pinning by intergranular elastic clamping [18]. Arlt et al. demonstrated that the width of 90° domains in $BaTiO_3$ ceramics decreases proportionately to the square root of the grain diameter, and the dielectric constant is partially controlled by 90° domain walls [19]. Meanwhile, global dielectric and piezoelectric measurements exhibit decreased domain wall motion with decreasing grain size [14, 20, 21].

In polycrystalline ceramics, it is expected that neighbouring grains will impose constraint upon each-other and this will ultimately affect the final domain configuration formed upon cooling through T_C. Typically, the constraints on grains in randomly oriented bulk polycrystalline ceramics are so severe that

stress-free states are unlikely and complex, hence energy minimising patterns form [8, 22]. Furthermore, in polycrystalline thin films and lamellae, the out-of-plane constraints can be relaxed, giving the material even greater freedom to adopt a stress-free configuration [23].

A bulk BaTiO₃-based ceramic is shown in Figure 3.1a, with average grain size ~4 µm. This ceramic is commercially available as a positive temperature coefficient of resistivity (PTCR) material; the functional properties and chemical identity of which will be studied in detail in the following chapter. Examples of ferroelastic domain patterns near grain boundaries in lamellae cut (via FIB) from the bulk ceramic are shown in Figure 3.1b and c; the domain configurations vary from high- to low-angle alignment (b-c) across grain boundaries and sectors with domains oriented parallel to the grain boundary are also present (b). The expectation is that as the lamellae are heated/cooled through T$_C$, the ferroelastic domains will rescale in accordance to Kittel's law [24, 25]. However, apart from
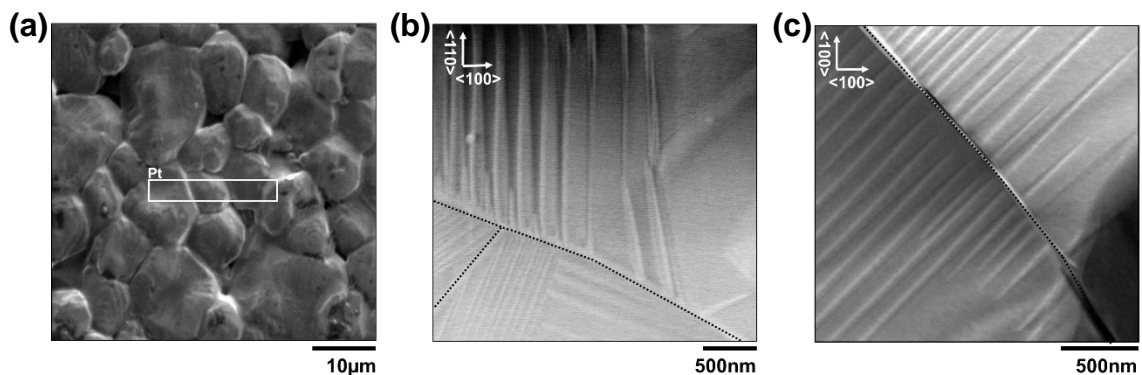
Figure 3.1: SEM image of a bulk BaTiO₃ ceramic (a). STEM images of lamellae fabricated via FIB from the bulk ceramic (b) and (c), displaying varied domain configurations near grain boundaries. Domains intersect the grain boundary at high angles (b) and low angles (c). Grain boundaries are marked by black dotted lines.

the rescaling it is of interest to analyse the new domain configuration, under the new stress regime (against the original, bulk one) and to investigate where the domain nucleation starts from; if the presence of grain boundaries plays a role in the nucleation. Hence, the approach utilised here is to study two cases: domains coupling across a single grain boundary, and the more complex case of the domain configuration within adjacent grains which meet around a junction (or pore). This study aims to have the starting point of knowing the static domain configuration before moving on to analyse the dynamic one (with heating).

3.2 Domain compatibility across a single grain boundary

 An example of a lamellae containing multiple grains is shown in Figure 3.2a. At this stage, the crystallographic orientations of the grains and types of domains (polarisation in-plane or out-of-plane) were unknown and deemed necessary before domain compatibility could be put to the test. However, it is well recognised that 180° domain walls produce negligible contrast in the TEM whereas, the change in unit cell orientation across ferroelastic 90° domain walls makes them widely accessible for observation. Therefore, the domains observed in Figure 3.2a were initially characterised as being the typical 90° type.

The left grain (labelled '1') was tilted to align the electron beam with the $<100>_{pc}$ type directions as can be determined from the diffraction pattern in Figure 3.2b, and without any further tilting of the lamella a subsequent diffraction
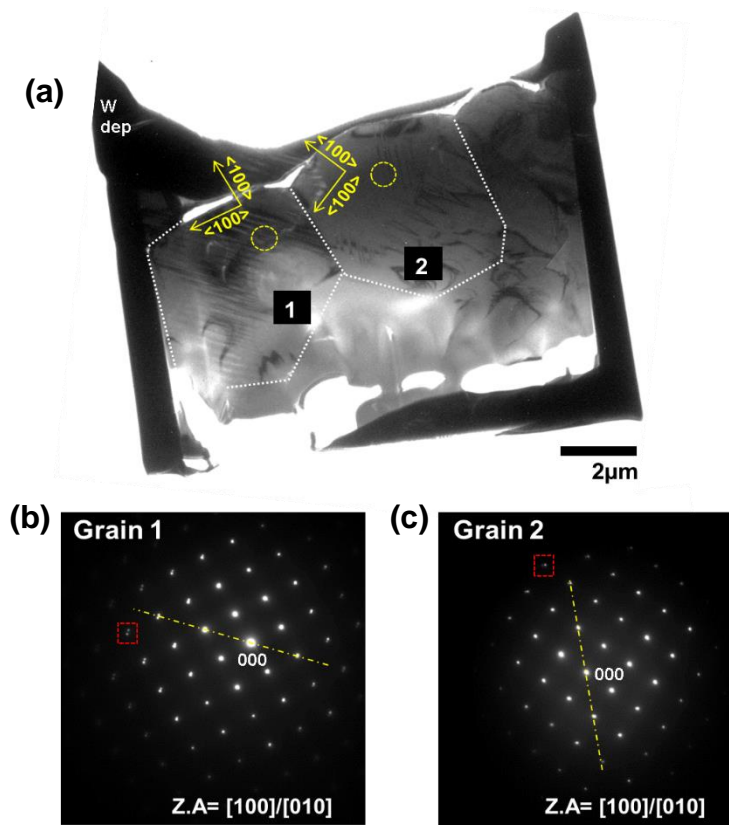
Figure 3.2: TEM BF image of a FIB prepared lamella (a), containing multiple grains and ferroelastic 90° domains. Corresponding diffraction patterns of grain 1 (b) and grain 2 (c) acquired from the designated dashed circles in (a). Domain wall orientations are overlaid (dashed lines) and the corresponding splitting of diffraction spots is highlighted (dashed boxes) in (b) and (c).

pattern was acquired from the dashed circle area in grain 2 (as shown in Figure 3.2c). Analysis of the diffraction patterns was carried out to determine whether the domains present in the selected area of each grain are 90° a-c type or a-a type structures. The presence of diffraction spot splitting along the orientation of the domain walls, which habitat $\{110\}_{pc}$ planes, was a tell-tail sign that the domains in both grains are 90° a-a domain types. The origin of the spot slitting stems from the fact that 90° domains have different unit cell orientations and therefore

polarisations that are separated by (90°-θ), where θ is dependent on the tetragonality as:

$$\theta = 2\tan^{-1}\left(\frac{c}{a}\right) - 90° \tag{3.1}$$

where c and a are the long and short lattice parameters of the tetragonal unit cell, respectively [26]. The value of θ measured from the diffraction patterns within grains 1 and 2 is 1.2 ± 0.4°. This splitting is further illustrated in Figure 3.3a where green and yellow rectangles indicate the diffraction patterns originating from each a-domain. A schematic picture is portrayed in Figure 3.3b illustrating the real-space vectors which describe the 90° a-a domains shown in Figure 3.3c. It is apparent that two real-space vectors in Figure 3.3b, each from different domains, have angular separation of θ or 90°±θ and these vectors are of the type <0kl>$_{pc}$ and <h0l>$_{pc}$ (where h=±k and k and l ≠0). The exception is the combination of two real-space vectors which lie in the plane parallel to the domain wall, these vectors have no angular separation. The same vector traits follow through to reciprocal space, as shown in an enlarged version of the diffraction spot splitting in Figure 3.3d. The specific polarisation direction of each domain cannot be established using this technique, however, the two possible directions to which each domain is crystallographic constrained are shown schematically in Figure 3.3c; it should be noted that the domains could be the other way around.
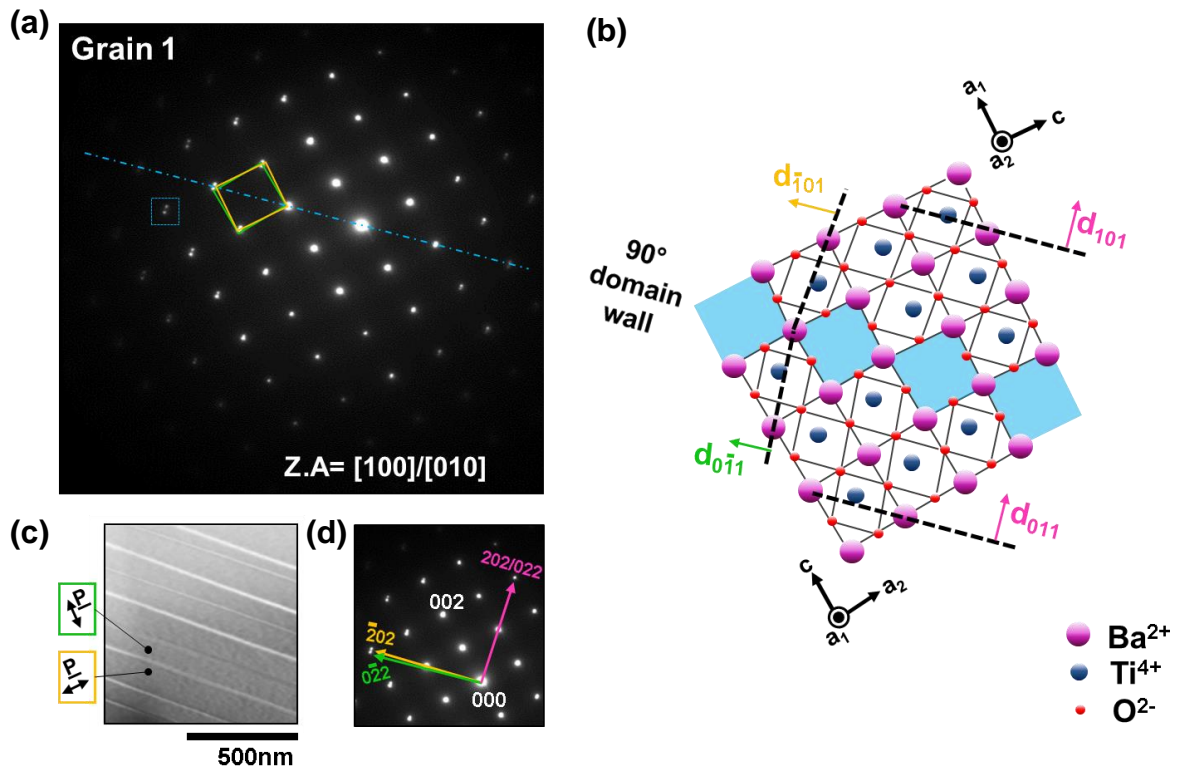
Figure 3.3: Diffraction pattern (a) and schematic representation of one of the 90° domain walls separating a-a domains in the STEM image of an area within grain 1 (c). The domain wall orientation is marked by a dashed line and the spot splitting is highlighted by a dashed box in (a). Yellow and green rectangles in (a) represent the diffraction patterns from each a-type domain shown in (c). The allowed polarisation directions are labelled for each domain in (c). The real space vectors shown in (b) are revealed in reciprocal space in an enlarged diffraction pattern (d). The schematic (b) was adapted from [26].

3.2.1 Analysis using theory of martensite crystallography

The compatibility conditions at a single domain wall are well known from the crystallographic theory of martensite [8, 27, 28]. Domain walls with a low energy configuration are said to be compatible if they have no net charge (continuity of the normal component of electrical polarisation) and no dislocations (continuity

of lattice strain) [29]. For a pair of ferroelectric domains i and j with lattice strain states $\boldsymbol{\varepsilon}_i$, $\boldsymbol{\varepsilon}_j$, and corresponding polarisation vectors $\mathbf{p}_i$, $\mathbf{p}_j$, the interface normal vector $\mathbf{n}$ of a compatible domain wall must satisfy:

$$\boldsymbol{\varepsilon}_i - \boldsymbol{\varepsilon}_j = \frac{1}{2}(\boldsymbol{a} \otimes \boldsymbol{n} + \boldsymbol{n} \otimes \boldsymbol{a}) \tag{3.2}$$

$$(\boldsymbol{p}_i - \boldsymbol{p}_j) \cdot \boldsymbol{n} = 0 \tag{3.3}$$

Provided a non-trivial vector $\mathbf{a}$ exists that satisfies (3.2), there is a compatibility of strains. Equation (3.3) ensures continuity of electrical polarisation, giving a charge-free domain wall in the absence of electric field or stress.

To test the compatibility of domains across a grain boundary, an area (1.6 µm x 1.6 µm) enclosing one of the grain boundaries shown in Figure 3.2a was analysed. The area shown in Figure 3.4a is thought to be a reasonable representation of the whole grain boundary, considering the grain size displayed in the overview of Figure 3.2a. The advantage of using STEM for this next stage of the analysis hails from the fact that STEM provides less diffraction contrast from bending contours, and is therefore ideal for providing a clearer observation of the domain contrast and grain boundary.

Figure 3.4a displays a STEM image of two sets of a-a domains which intersect along the grain boundary between grains 1 and 2. The domain walls are orientated at 45° to the local [001] directions as determined from the diffraction patterns (Figure 3.4b and c), the separation between local [001] directions was measured to be 24° as displayed in the inset of Figure 3.4c.
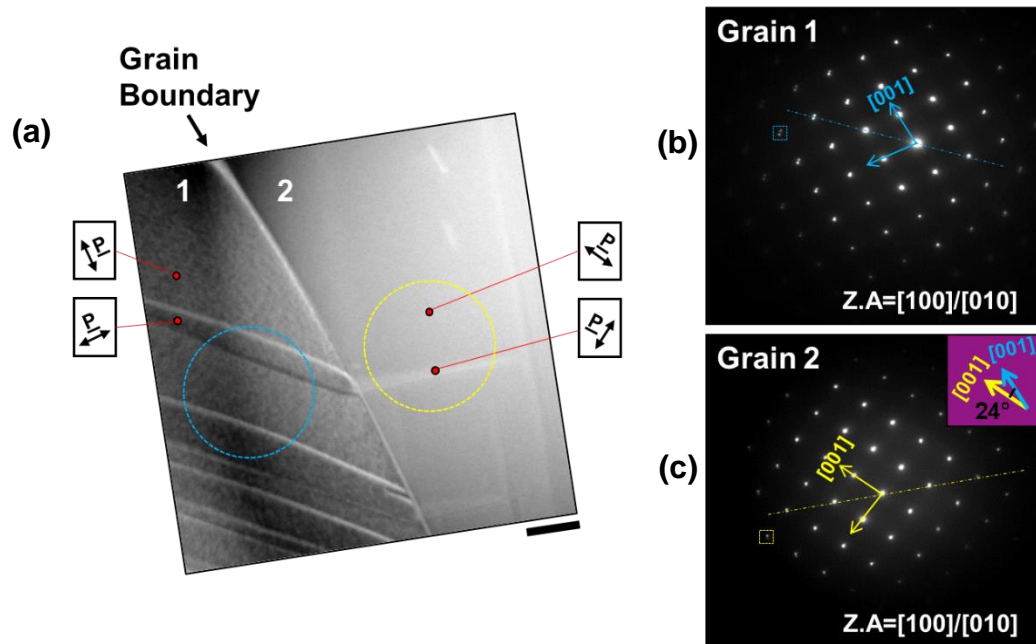
Figure 3.4: STEM image of the grain boundary separating grains 1 and 2 (a). Diffraction pattern acquired from the circled area in grain 1 (b) and grain 2 (c). The allowed polarisation directions are labelled in (a). The separation between local [001] directions was measured to be 24° as displayed in the inset of (c). The scale bar represents 200nm.

A schematic of the area imaged in Figure 3.4a is depicted in Figure 3.5 for ease of analysis using crystallographic theory of martensite. The domains have been labelled A-D for clarity and the (x, y, z) coordinates have been aligned with respect to grain 1. It can be noted from Figure 3.5 that grain 1 consists of A and B domains with about $1/3$ being B domains, mostly towards the lower part of the image. The A/B domain walls are 45° to the local [001] (and hence the x-axis of the chosen coordinates). The grain boundary curves slightly but is about 2° from the x-axis. Grain 2 consists of nearly all C domains near the grain boundary, with a small quantity <0.1 (fractional volume) of D. The local [001] direction is 24° from the x-axis and the C/D domain walls are 45° from the local [001] direction.
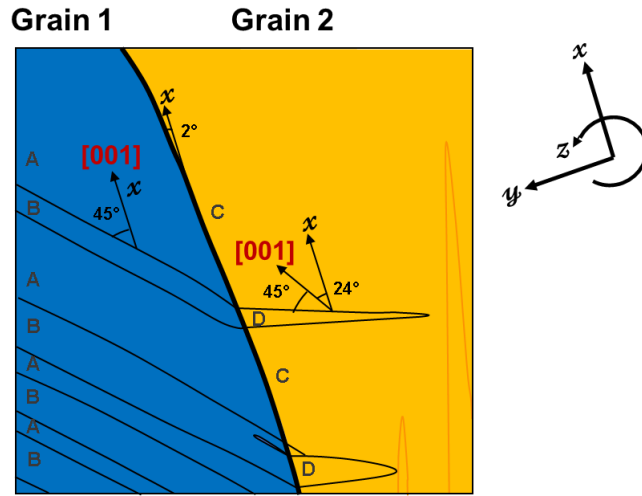
Figure 3.5: Schematic of the grain boundary imaged in Figure 3.4a. Domains and local [001] directions have been labelled. The (x, y, z) coordinates are aligned with grain 1.

Assuming that both grains are stress-free containing cubic unit cells of BaTiO₃ above T_C with lattice parameter a~4.009Å [30] and at room temperature, the unit cells have tetragonal structure with a_1=3.992Å and c=4.035Å. It can then be expected that A and B are compatible domains with c-axis arranged as follows (note that they could be the other way around):

Domain	c-axis	Strain state	
A	[001]	$$\varepsilon_A = \begin{bmatrix} \frac{c-a}{a} & 0 & 0 \\ 0 & \frac{a_1-a}{a} & 0 \\ 0 & 0 & \frac{a_1-a}{a} \end{bmatrix}$$	(3.4)
B	[010]	$$\varepsilon_B = \begin{bmatrix} \frac{a_1-a}{a} & 0 & 0 \\ 0 & \frac{c-a}{a} & 0 \\ 0 & 0 & \frac{a_1-a}{a} \end{bmatrix}$$	(3.5)

86

Then,

$$\boldsymbol{\varepsilon}_A = \begin{bmatrix} 0.0065 & 0 & 0 \\ 0 & -0.0042 & 0 \\ 0 & 0 & -0.0042 \end{bmatrix} \tag{3.6}$$

$$\boldsymbol{\varepsilon}_B = \begin{bmatrix} -0.0042 & 0 & 0 \\ 0 & 0.0065 & 0 \\ 0 & 0 & -0.0042 \end{bmatrix} \tag{3.7}$$

The A/B domain wall has normal:

$$\underline{\mathbf{n}} = \frac{1}{\sqrt{2}} \begin{bmatrix} 1 \\ -1 \\ 0 \end{bmatrix} \tag{3.8}$$

The Hadamard Jump condition for compatibility of small strains requires (for some $\mathbf{s}$) [31, 32]:

$$\boldsymbol{\varepsilon}_A - \boldsymbol{\varepsilon}_B = \underline{\mathbf{n}}\underline{\mathbf{s}}^{\mathrm{T}} + \underline{\mathbf{s}}\underline{\mathbf{n}}^{\mathrm{T}} \tag{3.9}$$

By inspection, this is true for

$$\underline{\mathbf{s}} = \frac{0.0107}{\sqrt{2}} \begin{bmatrix} 1 \\ 1 \\ 0 \end{bmatrix} \tag{3.10}$$

so, domains A and B can be compatible and stress-free.

To work out the strains in grain 2 the strain states can be rotated into (x,y,z) coordinates with a 24° rotation:

$$\mathbf{R} = \begin{bmatrix} \cos 24° & -\sin 24° & 0 \\ \sin 24° & \cos 24° & 0 \\ 0 & 0 & 1 \end{bmatrix} \tag{3.11}$$

therefore,

$$\boldsymbol{\varepsilon}_C = \mathbf{R}\boldsymbol{\varepsilon}_A\mathbf{R}^{\mathrm{T}} = \begin{bmatrix} 0.0047 & 0.0040 & 0 \\ 0.0040 & -0.0025 & 0 \\ 0 & 0 & -0.0042 \end{bmatrix} \tag{3.12}$$

and

$$\boldsymbol{\varepsilon}_D = \mathbf{R}\boldsymbol{\varepsilon}_B\mathbf{R}^{\mathrm{T}} = \begin{bmatrix} -0.0025 & -0.0040 & 0 \\ -0.0040 & 0.0047 & 0 \\ 0 & 0 & -0.0042 \end{bmatrix} \tag{3.13}$$

The A/C and B/D grain boundary has normal direction:

$$\underline{\mathbf{n}}_{AC} = \begin{bmatrix} -\sin 2° \\ \cos 2° \\ 0 \end{bmatrix} = \begin{bmatrix} -0.0349 \\ 0.9994 \\ 0 \end{bmatrix} \tag{3.14}$$

And tangent direction:

$$\underline{\mathbf{t}}_{AC} = \begin{bmatrix} \cos 2° \\ \sin 2° \\ 0 \end{bmatrix} = \begin{bmatrix} 0.9994 \\ 0.0349 \\ 0 \end{bmatrix} \tag{3.15}$$

The C/D domain wall is at 69° to the x-axis, with normal direction:

$$\underline{\mathbf{n}}_{CD} = \begin{bmatrix} \sin 69° \\ -\cos 69° \\ 0 \end{bmatrix} = \begin{bmatrix} 0.9336 \\ -0.3584 \\ 0 \end{bmatrix} \tag{3.16}$$

The condition

$$\boldsymbol{\varepsilon}_C - \boldsymbol{\varepsilon}_D = \underline{\mathbf{n}}_{CD}\underline{\mathbf{s}}^{\mathrm{T}} + \underline{\mathbf{s}}\underline{\mathbf{n}}_{CD}^{\mathrm{T}} \tag{3.17}$$

solves to give

$$\underline{\mathbf{s}} = \begin{bmatrix} 0.0088 \\ 0.0100 \\ 0 \end{bmatrix} \tag{3.18}$$

So, it is confirmed that the C/D domain wall is a compatible stress-free domain wall. The question now lies in whether domains A and C are compatible across the grain boundary. This would require (for some $\mathbf{s}$):

$$\boldsymbol{\varepsilon}_A - \boldsymbol{\varepsilon}_C = \underline{\mathbf{n}}_{AC}\underline{\mathbf{s}}^{\mathrm{T}} + \underline{\mathbf{s}}\underline{\mathbf{n}}_{AC}^{\mathrm{T}} \tag{3.19}$$

There is no solution to (3.19), meaning that the A/C grain boundary is stressed.

It is now of interest to investigate whether some mixture of A/B domains can produce an average strain that is compatible with the average strain of the C/D domains at the grain boundary. To do this, the stretch at the grain boundary due to each type of domain needs to be considered.

The stretch, e, takes the form:

$$\underline{\mathbf{t}}_{AC} \cdot \left(\boldsymbol{\varepsilon}.\underline{\mathbf{t}}_{AC}\right) \tag{3.20}$$

Calculating the stretch for each domain type gives:

$$e_A = \underline{\mathbf{t}}_{AC} \cdot \left(\boldsymbol{\varepsilon}_A \cdot \underline{\mathbf{t}}_{AC}\right) = 0.00647 \tag{3.21}$$

$$e_B = \underline{\mathbf{t}}_{AC} \cdot \left(\boldsymbol{\varepsilon}_B \cdot \underline{\mathbf{t}}_{AC}\right) = -0.00423 \tag{3.22}$$

$$e_C = \underline{\mathbf{t}}_{AC} \cdot \left(\boldsymbol{\varepsilon}_C \cdot \underline{\mathbf{t}}_{AC}\right) = 0.00498 \tag{3.23}$$

$$e_D = \underline{\mathbf{t}}_{AC} \cdot \left(\boldsymbol{\varepsilon}_D \cdot \underline{\mathbf{t}}_{AC}\right) = -0.00274 \tag{3.24}$$

For example, to form a boundary that is on average stress-free, and with equal ratios A:B =C:D, the following could be set:

$$e_A + f e_B = e_C + f e_D \tag{3.25}$$

where *f* represents the volume fraction. This solves to give *f*=1.00

This result may seem a coincidence at first sight, but actually is unsurprising since setting *f*=1.00 produces a mixture of domains with an average strain state that is in-plane isotropic. The resulting strain state is hence compatible with any rotation of itself in plane. It might well be expected that the grains in this example should have formed with roughly equal fractions of A:B and C:D domains. This did not happen here. One explanation could be that grain 2 formed a large C domain first and then grain 1 formed domains to match this. If this were the case, the A:B mixture would form such that

$$\boldsymbol{e}_A + f\boldsymbol{e}_B = \boldsymbol{e}_C \qquad (3.26)$$

which solves to give f=0.35, roughly matching the observed A:B ratio. Other evidence in support of this interpretation is:

- $\boldsymbol{e}_B$ and $\boldsymbol{e}_C$ have opposite sign. The B domains narrow as they approach the grain boundary

- $\boldsymbol{e}_B$ is close to $\boldsymbol{e}_D$, explaining the formation of D domains across the grain boundary to minimise stress. The D domains do not penetrate far into grain 2.

- Considering other possible arrangements of the domains at the grain boundary shows that A/D are badly mismatched and B/C are badly mismatched.

It can be concluded that in this example, it is probable that grain 2 formed a large C domain on cooling through T$_c$ to the ferroelectric phase, grain 1 then formed a mixture of A/B domains to accommodate the imposed strain. The new B domains

are mismatched to the C domain at the grain boundary and so a small quantity of D domains formed to reduce stress. Overall, the domains observed in this example demonstrate a "compatible on average" domain arrangement at the grain boundary.

3.3 Compatible domain arrangements in grains meeting around a junction

A more complex situation of interest is the domain microstructure which arises in grains which meet around a junction (or pore); which also resembles the more common case found in the bulk ceramic. This investigation includes the added intricacy of a group of grains with rotation between neighbouring grains varying in more than one direction, compared to the investigation in Section 3.2 which consisted of only two grains and a rotation only along the x axes.

3.3.1 Problem definition

A group of N grains i=1….N fit together around a junction in a thin lamella which lies in the x-y plane, as shown in Figure 3.6. The grain boundary between pairs of grains (i, j) has normal direction $\mathbf{n}_{ij}$ and tangential direction $\mathbf{t}_{ij}$ in the plane of the lamella. Each grain has its crystallographic axes rotated relative to reference (x,y,z) coordinates by rotation matrix $\mathbf{R}_i$ and undergoes a transformation strain $\boldsymbol{\varepsilon}_i$
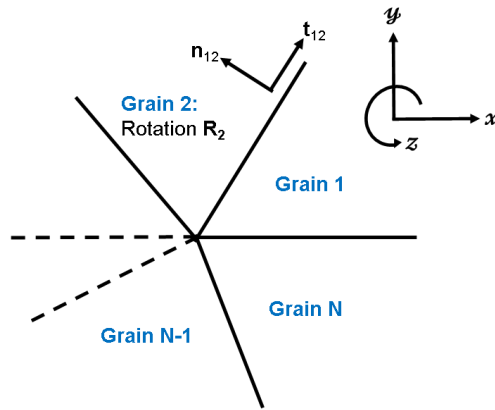
Figure 3.6: Schematic of the configuration of grains around a junction.

belonging to the set of stress-free martensitic states, or mixtures of such crystal variants (domains). The question of interest is whether the resulting group of grains can fit together without stress, and, what pattern of domains will form?

3.3.2 Reduction to linear equations and inequalities

Of interest is the state where each grain undergoes a transformation strain that is uniform on the scale of the grain (though not on finer scales), with the grain comprising a mixture of the stress-free transformation strains that correspond to the individual crystal variants (domains). Then the transformation strain may be written, in the local coordinates of the grain, as:

$$\varepsilon_i' = \sum_k f_{ik} \varepsilon_k^0 \tag{3.27}$$

where ε_k^0 is the transformation strain of the k th crystal variant and f_{ik} is the volume of that crystal variant in the i th grain. In reference coordinates, this becomes

$$\boldsymbol{\varepsilon}_i = \sum_k f_{ik} \mathbf{R}_i \boldsymbol{\varepsilon}_k^0 \mathbf{R}_i^{\mathrm{T}} \tag{3.28}$$

Where adjacent grains meet, the compatibility condition

$$\boldsymbol{\varepsilon}_i - \boldsymbol{\varepsilon}_j = \mathbf{a}_{ij} \otimes \boldsymbol{n}_{ij} + \mathbf{n}_{ij} \otimes \boldsymbol{a}_{ij} \tag{3.29}$$

can be used to ensure continuity of displacement. If equation (3.29) is satisfied by choosing some vector $\mathbf{a}_{ij}$, then the grain boundary is a compatible interface in the stress-free state. While equation (3.29) is suitable for full three-dimensional constraint, the case of a thin lamella is less constrained provided that the grains are much larger than the lamellar thickness. This is because out-of-plane displacements are unconstrained. In fact, only a single displacement component is of relevance in the lamellar case: displacement in the plane of the lamella and in the direction along the grain boundary. Continuity requires no jump of displacement along the boundary as it is crossed. A condition for matching displacement components along the boundary is achieved by considering equation (3.29) resolved in the $\mathbf{t}_{ij}$ direction:

$$\mathbf{t}_{ij} \cdot (\boldsymbol{\varepsilon}_i - \boldsymbol{\varepsilon}_j) \cdot \mathbf{t}_{ij} = \mathbf{t}_{ij} \cdot (\mathbf{a}_{ij} \otimes \mathbf{n}_{ij} + \mathbf{n}_{ij} \otimes \mathbf{a}_{ij}) \cdot \mathbf{t}_{ij} = 0 \tag{3.30}$$

The compatibility conditions for the grains of the lamella become a set of N equations of the form

$$\mathbf{t}_{12} \cdot \boldsymbol{\varepsilon}_1 \cdot \mathbf{t}_{12} - \mathbf{t}_{12} \cdot \boldsymbol{\varepsilon}_2 \cdot \mathbf{t}_{12} = 0 \tag{3.31}$$

and so forth. Defining scalar l_{ijk} as the linear strain in grain i along the boundary with grain j due to the k th crystal variant,

$$l_{ijk} = \mathbf{t}_{ij} \cdot (\mathbf{R}_i \boldsymbol{\varepsilon}_k^0 \mathbf{R}_i^{\mathrm{T}}) \cdot \mathbf{t}_{ij} \tag{3.32}$$

The N compatibility conditions then take the form

$$\sum_k f_{ik} l_{ijk} - f_{jk} l_{jik} = 0 \tag{3.33}$$

where only the N pairings (i,j) for which grain boundaries exist are allowed. Note that the formulation is readily extended to consider the more general problem of a group of grains in a polycrystalline lamella by allowing all (i,j) pairings that represent grain boundaries present in the polycrystalline sample. For the present problem, the equations entailed by (3.33) form a closed chain of connections between adjacent grains around a single junction, and ignore any constraint external to that group. Since equation (3.33) expresses the compatibility conditions explicitly in terms of the volume fractions of the crystal variants, the following additional constraints apply to f_{ik}:

$$\sum_k f_{ik} = 1 \tag{3.34}$$

and

$$f_{ik} \geq 0 \tag{3.35}$$

Equation (3.34) produces N linear equations, and equation (3.35) is a set of mN inequalities in a system with m crystal variants and N grains. Equations (3.33) and (3.34) provide $2N$ linear relations for the mN volume fractions in the individual grains. Thus, the system of linear equations is underdetermined except in the case $m=2$. For tetragonal martensites $m=3$ and so there can exist a space of solutions of the form

$$f_{ik} = \sum_{j=0}^{N} \alpha^j f_{ik}^j \tag{3.36}$$

With $\alpha^0 = 1$, f_{ik}^0 a particular solution, and the f_{ik}^j ($j > 0$) comprising a basis for the solution space. The $\alpha^j (j = 1 \dots N)$ are arbitrary and provide the N degrees of freedom of the solution. By further imposing the inequality constraints, (3.35), the α^j values may be restricted to those that give feasible volume fractions. Therefore, uniqueness of solutions is not guaranteed (and indeed is unlikely in practical examples).

3.3.3 Assumptions and approximations

The compatibility conditions and feasible volume fraction conditions, (3.33) - (3.35), do not provide a complete description of the problem, and some other aspects should be noted. Firstly, the problem has been formulated using the small strain, linear, theory. This is adequate for describing the constraint at individual boundaries in materials such as BaTiO₃, which have spontaneous strain magnitudes less than 1%. However, it does not capture the closure condition around a junction of grains. This situation is best understood by considering the orientation and position of one grain boundary (for example $i = N$, $j = 1$) to be fixed. Subsequent grain boundaries may translate and rotate relative to their reference position. However, on making a complete circuit of the central junction of grains, the final grain must meet the initial grain at the fixed initial boundary. This constraint could be formulated in terms of a sum over in-plane strain components. Alternatively, use of the non-linear version of the theory of compatibility will capture the continuity requirement. The closure conditions are likely to be of importance in fully three-dimensional examples such as films with grain diameter less than the film thickness, or bulk polycrystals. In thin lamellae

with large grains, the closure conditions become less significant because mismatch can be accommodated by out-of-plane bending or buckling of the lamella with relatively low energetic cost. For the present investigation, the full closure conditions have been neglected as an approximation. Secondly, it should be noted that polar materials such as $BaTiO_3$ will be subject to electrical compatibility conditions due to Maxwell's laws. If the surface is charge-free, for example, the average normal component of electrical polarisation will be close to zero. Similarly, there can be no jump in the tangential component of electric field across each grain boundary. Fuller consideration of these conditions is relatively straightforward by extending the description to six tetragonal crystal variants in pairs with opposite polarisation. In the present description, this detail has been ignored in the expectation that the electrical conditions are less restrictive than their mechanical counterparts, and can usually be met by introducing 180° domain pairing into the purely mechanical solution. Finally, the assumption of macroscopically uniform straining in each grain may be overly restrictive. In nature, the system may introduce variations in the pattern of domains within a single grain. One simple example would be the division of a single grain into two regions, each of uniform strain. Divisions of this type are evident in experimental data, but have been neglected for simplicity in the present investigation.

3.3.4 Computation of a compatibility solution

For computation, it is convenient to prepare the linear algebra problem in the form

$$\mathbf{Lf} = \mathbf{k}; \quad \mathbf{f} \geq 0 \tag{3.37}$$

Where $\mathbf{L}$ is the $2N$ x mN matrix of coefficients

$$\begin{bmatrix} l_{121} & \cdots & l_{12m} & -l_{211} & \cdots & -l_{21m} & 0 & \cdots & 0 \\ 0 & \cdots & 0 & l_{231} & \cdots & l_{23m} & -l_{321} & \cdots & 0 \\ \vdots & & & & \ddots & & & & \\ -l_{1N1} & \cdots & -l_{1Nm} & & & & & & l_{N1m} \\ 1 & \cdots & 1 & 0 & \cdots & 0 & & \cdots & 0 \\ 0 & \cdots & 0 & 1 & \cdots & 1 & & \cdots & 0 \\ \vdots & & & & \ddots & & & & \vdots \\ 0 & & & & & & & \cdots & 1 \end{bmatrix} \tag{3.38}$$

while $\mathbf{f}$ and $\mathbf{k}$ are column matrices of length mN and $2N$ respectively, given by

$$\boldsymbol{f} = \begin{bmatrix} f_{11} \\ f_{12} \\ \vdots \\ f_{1m} \\ f_{21} \\ \vdots \\ f_{Nm} \end{bmatrix}, \qquad \boldsymbol{k} = \begin{bmatrix} 0 \\ \vdots \\ 0 \\ 1 \\ 1 \\ \vdots \\ 1 \end{bmatrix} \tag{3.39}$$

The first N rows provide the compatibility equations, while rows $N+1\cdots2N$ ensure that the volume fractions sum to unity in each grain. Inverting this system of equations, including the inequalities in (3.37) can be achieved using active set methods, for example using the Matlab function **1sqnonneg**. This function seeks a solution that satisfies all the inequalities and minimises the norm $\|\mathbf{Lf} - \mathbf{k}\|$. Formulated in this way, the solution is of interest only if the residual is zero, in

which case **1sqnonneg** identifies an exact solution for the volume fractions in **f**. Minimisers of $\|\mathbf{Lf} - \mathbf{k}\|$ with non-zero residual do not represent minimum energy solutions; they may also violate the overall constraints on volume fractions summing to unity. Since the solution may be non-unique, further interrogation of the solution space could be achieved by considering the kernel of **L**, which can be computed by the Matlab function **null**.

Once a solution in terms of the volume fractions, **f**, is known, the strains of the individual grains are readily reconstructed using (3.28). Of interest in the context of experimental images of the lamellae are the orientations and spacing of visible domain walls. Non-zero elements of **f** indicate which crystal variants are present and in what proportions. Then, the compatible domain wall orientations between these crystal variants can be reconstructed using a local version of (3.29):

$$\boldsymbol{\varepsilon}_k^0 - \boldsymbol{\varepsilon}_l^0 = \mathbf{a} \otimes \mathbf{n} + \mathbf{n} \otimes \mathbf{a} \qquad (3.40)$$

where k and l are any two crystal variants present and solving for **n** gives a domain wall normal in local grain coordinates. The solutions are well known for most crystal systems; for tetragonal unit cells, they lie in the <110>pc directions. Visible lines in the lamella, that are intersections of the domain walls with the x-y plane of the lamella, are parallel to

$$\boldsymbol{e}_z \times (\mathbf{R}_i \mathbf{n}) \qquad (3.41)$$

where $\mathbf{e}_z$ is a unit vector in the z-direction. Their spacing is indicative of the volume fractions.

To illustrate the calculation, consider a group of four grains meeting at a junction in a BaTiO₃ lamella, as experimentally shown in the STEM image of Figure 3.7a (and schematically shown in Figure 3.7b) with domains clearly visible. The STEM image of this junction was acquired with the grain labelled '3' oriented along the [131] zone axis. Since this grain has been imaged with the electron beam parallel to a direction which is not one of the main crystallographic axes (e.g. <100>), projection effects have resulted in non-90° angles between domains [33, 34]. Projection effects are also apparent in the other grains ('1', '2' and '4') of this image (domain angle discrepancies of ± 5-10°) since the electron beam was not parallel to a main zone axis for any of these grains on image acquisition.

The three tetragonal strain states in this example can be represented by:

$$\boldsymbol{\varepsilon}_1^0 = \begin{bmatrix} 1 & 0 & 0 \\ 0 & -\frac{1}{2} & 0 \\ 0 & 0 & -\frac{1}{2} \end{bmatrix}; \quad \boldsymbol{\varepsilon}_2^0 = \begin{bmatrix} -\frac{1}{2} & 0 & 0 \\ 0 & 1 & 0 \\ 0 & 0 & -\frac{1}{2} \end{bmatrix}; \quad \boldsymbol{\varepsilon}_3^0 = \begin{bmatrix} -\frac{1}{2} & 0 & 0 \\ 0 & -\frac{1}{2} & 0 \\ 0 & 0 & 1 \end{bmatrix} \quad (3.42)$$

The orientations of the grains can be represented using Euler angles $(\alpha, \beta, \gamma)_i$ where angle α specifies a first rotation about the z-axis, producing (x',y',z'), β specifies a second rotation about the y'-axis, producing axes (x'',y'',z''), and γ specifies a third rotation about the x''-axis. Then rotation matrices $\mathbf{R}_i$ are given by

$$\mathbf{R}_i = \begin{bmatrix} \cos\alpha & -\sin\alpha & 0 \\ \sin\alpha & \cos\alpha & 0 \\ 0 & 0 & 1 \end{bmatrix} \begin{bmatrix} \cos\beta & 0 & -\sin\beta \\ 0 & 1 & 0 \\ \sin\beta & 0 & \cos\beta \end{bmatrix} \begin{bmatrix} 1 & 0 & 0 \\ 0 & \cos\gamma & -\sin\gamma \\ 0 & \sin\gamma & \cos\gamma \end{bmatrix} \quad (3.43)$$

The example shown in Figure 3.7 has approximate Euler angles as listed in Table 1. The Euler angles were approximated based on tilting each individual grain near
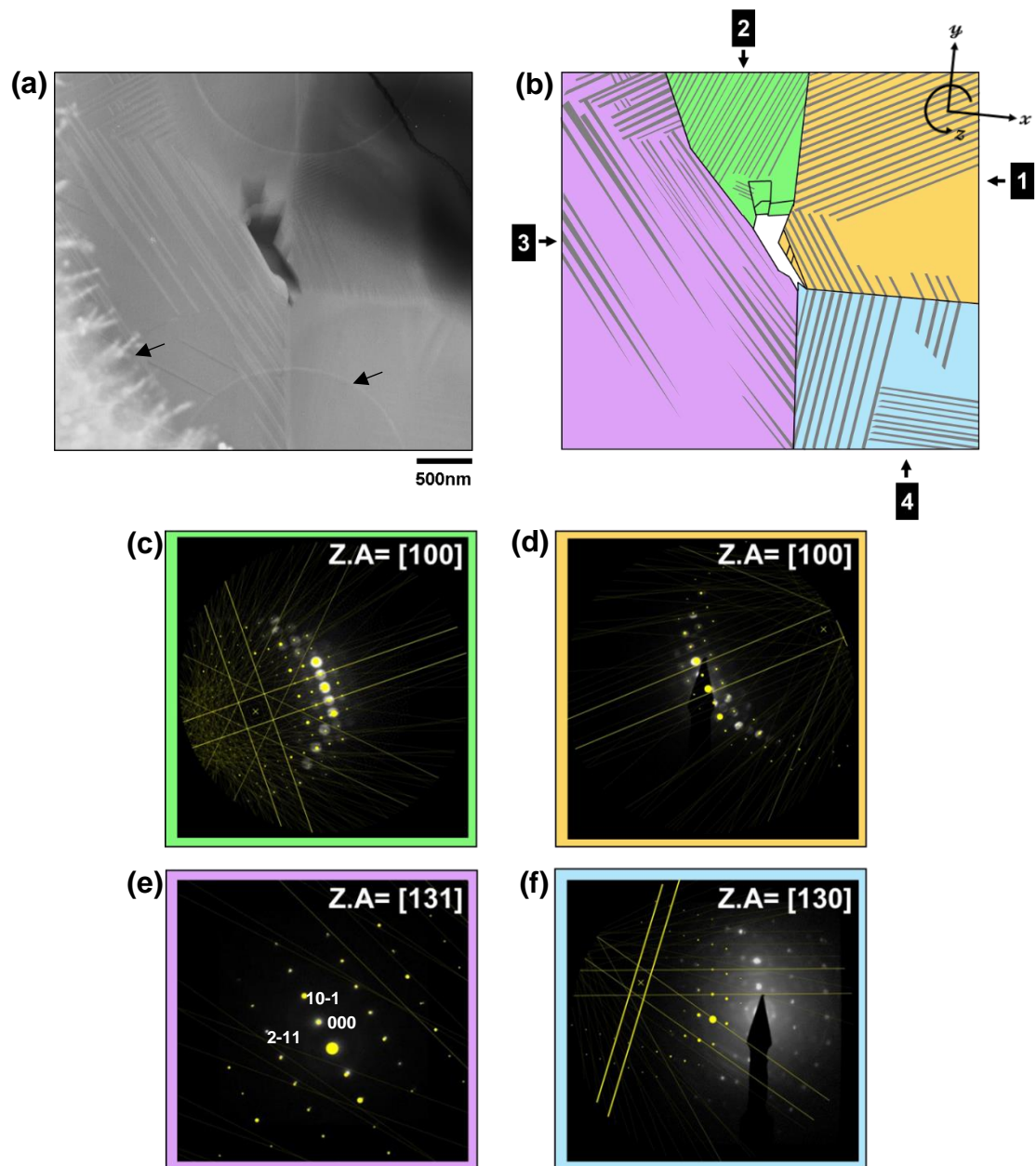
Figure 3.7: Experimental example of a grain junction. STEM image of four grains surrounding a pore (a), with grain 3 on zone axis, features marked with arrows can be ignored (from the carbon membrane). Schematic of the junction with coloured grains (1-4) and ferroelastic domains illustrated (b). Diffraction patterns for grain 2 (c), grain 1 (d), grain 3 (e) and grain 4 (f), with the nearest zone axis labelled in the top right, reference kikuchi lines and diffraction spots are overlaid in yellow.

to a zone axis (as shown in the diffraction patterns in Figures 3.7c-f). It should be noted however, that the ability to tilt the grains onto the centre of a zone axis was severely limited by the tilting capabilities of the TEM holder, a single-tilt in-situ heating holder was used for the imaging of this grain junction example (heating investigation to follow in Section 3.4); since no double-tilt was available at the time. The closest zone-axis for each grain was confirmed by overlaying reference kikuchi lines and corresponding diffraction spots onto each diffraction pattern, displayed in yellow in Figures 3.7c-f. It would be of interest however, to use EBSD prior to FIB milling of future lamellae, in this way the precise Euler angles could be obtained.

Grain	α (°)	β (°)	γ (°)
1	0	0	0
2	0	0	135
3	30	0	0
4	90	90	0

Table 1: Euler angles used for the example lamella in Figure 3.7.

The grain boundaries in Figure 3.7 are at angles of 90°, 150°, 275° and 0° respectively, measured from the x-axis. Hence

$$\mathbf{t}_{12} = [0.0000\ 1.0000\ 0.0000]^{\mathrm{T}}; \quad \mathbf{t}_{23} = [-0.8660\ 0.5000\ 0.0000]^{\mathrm{T}};$$

$$\mathbf{t}_{34} = [\,0.0872 - 0.9962\ 0.0000]^{\mathrm{T}}; \quad \mathbf{t}_{41} = [1.0000\ 0.0000\ 0.0000]^{\mathrm{T}};$$

Using Matlab, the element matrix elements of **L** were generated as:

−0.5000	1.0000	−0.5000	0.5000	−0.2500	−0.2500	0.0000	0.0000	0.0000	0.0000	0.0000	0.0000
0.0000	0.0000	0.0000	0.6250	−0.3125	−0.3125	0.1250	−0.6250	0.5000	0.0000	0.0000	0.0000
0.0000	0.0000	0.0000	0.0000	0.0000	0.0000	−0.2321	0.7321	−0.5000	0.5000	0.4886	−0.9886
−1.0000	0.5000	0.5000	0.0000	0.0000	0.0000	0.0000	0.0000	0.0000	−0.5000	1.0000	−0.5000
1.0000	1.0000	1.0000	0.0000	0.0000	0.0000	0.0000	0.0000	0.0000	0.0000	0.0000	0.0000
0.0000	0.0000	0.0000	1.0000	1.0000	1.0000	0.0000	0.0000	0.0000	0.0000	0.0000	0.0000
0.0000	0.0000	0.0000	0.0000	0.0000	0.0000	1.0000	1.0000	1.0000	0.0000	0.0000	0.0000
0.0000	0.0000	0.0000	0.0000	0.0000	0.0000	0.0000	0.0000	0.0000	1.0000	1.0000	1.0000

The solution satisfying the compatibility conditions generated the volume fractions, **f**:

Grain	Variant 1	Variant 2	Variant 3
1	0.686	0.314	0.000
2	0.372	0.628	0.000
3	0.785	0.215	0.000
4	0.000	0.686	0.314

Note that all four grains have two crystal variants present and so can form domain walls. Using equations (3.40) and (3.41), the domain walls were calculated as lines in the lamella oriented along the directions shown in (x, y) coordinates in Table 2, and illustrated in Figure 3.8a.

Grain	Visible domain wall drections $[x, y]$	
1	$[0.707, −0.707]$	$[0.707, 0.707]$
2	$[−0.577, −0.816]$	$[−0.577, 0.816]$
3	$[0.966, −0.259]$	$[0.259, 0.966]$
4	$[−0.707, 0.707]$	$[−0.707, −0.707]$

Table 2: Domain wall intersections with the plane of the lamella
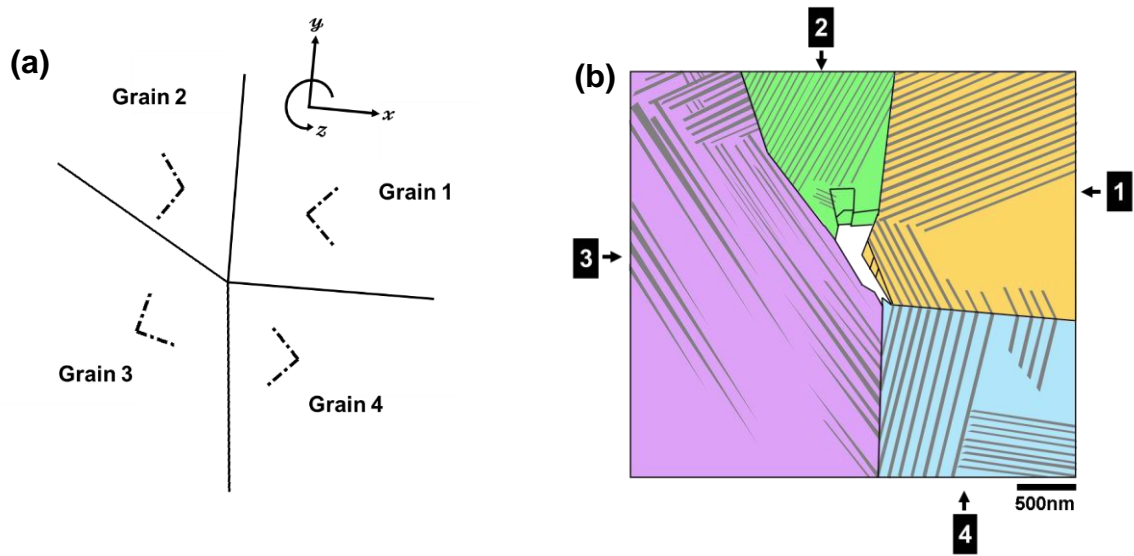
Figure 3.8: Solution of domain wall directions (black dashed lines) for the grain junction calculation (a). Schematic of experimental lamella example (b) repeated from Figure 3.7b for ease of comparison.

3.3.5 Discussion of the compatibility solution and comparison to the experimental example

The calculation here presented provides a good approach for satisfying the compatibility conditions in a group of twinned grains around a junction. Comparing the fractional volume of crystal variants f, with the experimental image shows good agreement. For example, grain 3 has a calculated 80% fractional volume of one crystal variant (resembling the purple domain type in Figure 3.8b) and 20% of the other crystal variant (grey domains). Due to the relatively simple grain rotations used in the calculation, the domain wall directions in the solution, Figure 3.8a, do not match perfectly with the experimental domain walls shown in Figure 3.8b. The discrepancies in domain

wall directions are ~20° about the x-axis. The largest discrepancy occurs in grain 3 with one of the domain wall directions misaligned by 45°. This is unsurprising for several reasons, firstly, the Euler angles used in the calculation were approximated because EBSD measurements were not available for the experiment. Secondly, the experimental image was acquired with grain 3 (the largest grain) on zone axis whereas the calculation effectively sees grain 1 on zone axis, with the domain walls of the neighbouring grains calculated as directions in the lamella oriented along the (x, y) coordinates. Thirdly, in the experimental example there is a large rotational twist in the grain boundary which neighbours the domain walls with the highest angular discrepancy (the grain boundary between grains 2 and 3), this artefact was not taken into account in the simplified calculation.

In a polycrystalline ceramic, a grain can produce two distinct strains along its two constrained boundaries, and has the freedom to vary these by having multiple domains. There is of course no constraint to have a uniform strain state over the whole grain. A simple way in which the polycrystalline ceramic can enhance its ability to satisfy the compatibility constraints without stress is by the splitting of grains into multiple sectors with different domain patterns in each sector (as demonstrated in Figure 3.8b). The compatibility solution can then take the advantage of the additional degrees of freedom to vary the volume fractions and domain pattern across the family of grains. It is worth noting that this lamella is relatively unconstrained, compared to the bulk. Therefore, a lamella removed from the bulk may reorganise its domain structure during a heating and cooling cycle to give a lower energy state. Many configurations may be possible due to the undetermined nature of the problem. Active set solution methods in this grain

junction calculation typically first seek a solution without using the inequality constraints, and proceed by invoking any inequalities that are violated by this solution. Hence, the result of using **1sqnonneg** typically has at least some volume fractions set to zero: this is advantageous in that it represents a solution with relatively few crystal variants present and hence few domain walls, consistent with minimisation of domain wall energy. The existence of solutions suggests that such lamellae may adopt states nearly free of self-stress.

To conclude, the problem of satisfying the compatibility conditions in a group of twinning grains around a shared junction has demonstrated that in the case of a lamellar polycrystal, the relaxation of out-of-plane constraint gives rise to an undetermined set of linear equations in the volume fractions of crystal variants. Additional inequality constraints on the volume fractions lead to (non-unique) solutions, indicating that groups of twinned grains in lamellae can form stress-free domain patterns. Since the constraint is much less than that of the bulk, a reorganisation of the bulk domain structure during heating and cooling of a lamella extracted from the bulk is likely.

3.4 Domain reorganisation on heat cycling through T$_c$

The grain junction lamella shown in Section 3.3 was investigated in-situ, availing of live STEM imaging to observe the domain reorganisation during heating and cooling through T$_c$. Figure 3.9 shows selected frames from the first heat cycle

where the lamella was heated from room temperature to 210°C (higher than T_c to ensure a full transition to the paraelectric phase) and back to room temperature. The T_c for this ceramic is ~160°C, this is higher than normal for BaTiO₃ (~120°C) due to an addition of Pb, most commonly added to commercial ceramics to raise the T_c [35].

Determination of domain type (whether it be a-a or a-c) is less straight forward for crystal orientations such as the [131] zone axis of grain 3; most likely domains within this grain will have a component of polarisation both in-plane and out-of plane of the lamellar face. The initial state of grain 3 prior to heat cycling (Figure 3.9a) shows a microstructure in which ferroelastic domains exist with two domain wall orientations, one spanning the length of the grain along $<101>_{pc}$ directions and the other along $<112>_{pc}$ directions (shown in the top corner of grain 3). The most likely explanation for this microstructure is that, at the initial phase transition cooling through T_c (during the processing of the ceramic), polarisation nucleated in different sites of the lamella, and the domains then grew laterally until they met. Adjacent domains with orthogonal polarisation impose elastic stress on each other, providing the driving force for the splitting into smaller twins.

The first heat cycle carried out was continuous in nature ranging from 25°C-210°C-25°C at 1°C per second. Important features to notice in the heat cycle frames from Figure 3.9 (mainly focusing on grain 3 (large left grain) because it is on zone axis and therefore provides the best domain contrast) include the reconfiguration of the bright contrast domains which span the length of grain 3. Focusing on these domains, which have domain walls along $<101>_{pc}$ directions, it
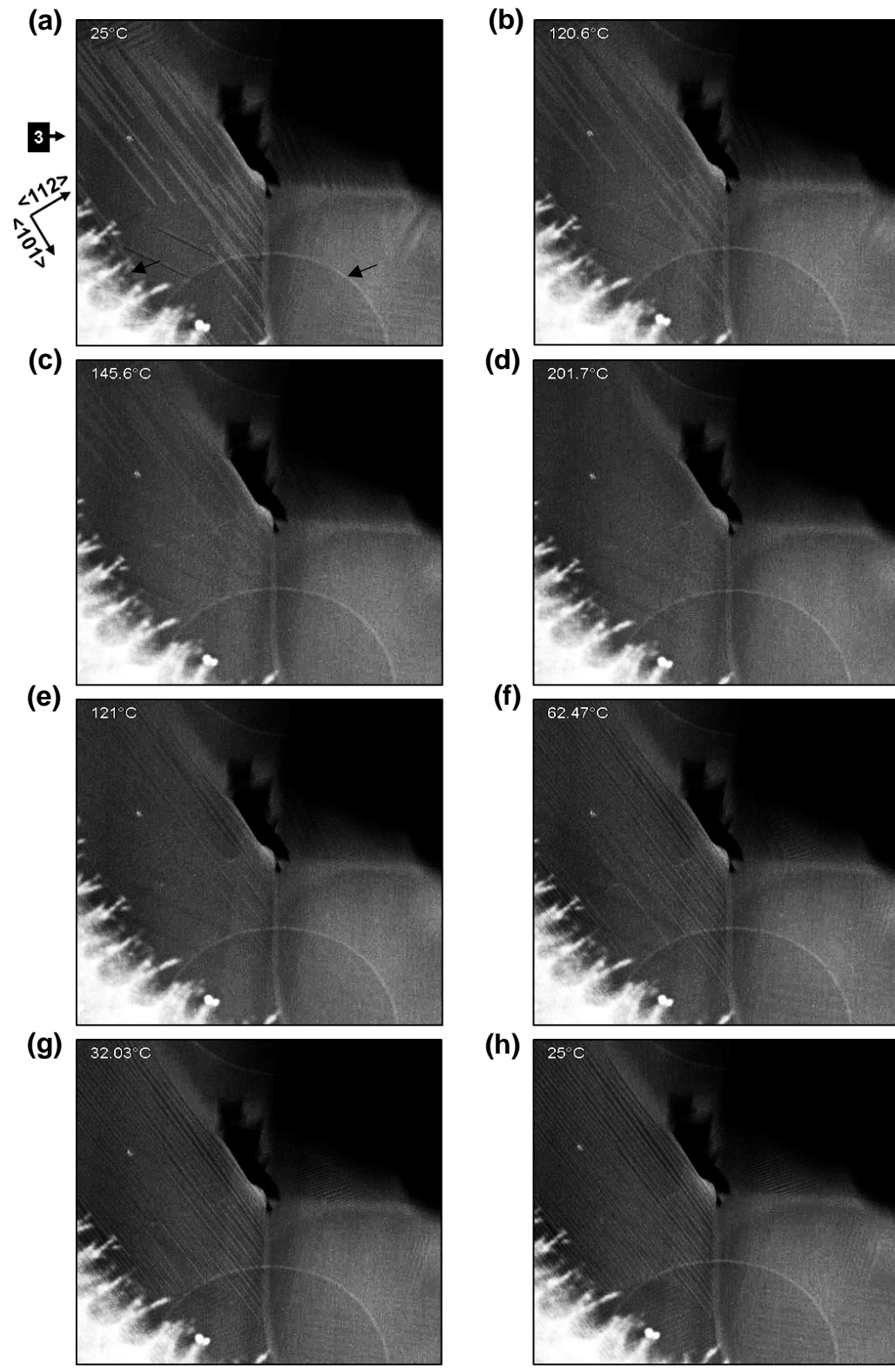
Figure 3.9: STEM images from the 1st heat-cycle: 25°C-210°C-25°C (1°C/sec). Temperature is labelled in the top left (a)-(h). Features marked with arrows in (a) can be ignored. Scale bar=500nm.

is firstly noticeable that as the temperature is raised the domains begin to disappear from the centre of the grain (beginning ~120°C in Figure 3.9b). These domains continue to disappear away from the centre of the grain (Figure 3.9c)until the ceramic lamella has fully transitioned to the paraelectric phase (Figure 3.9d). On cooling back to room temperature through T_c, these domains begin to propagate at a higher density from the top grain boundary spanning along the length of the grain (Figures 3.9e,f and g) until they reach the lower grain boundary (between grains 3 and 4). A small section of these domains fail to propagate the whole length of the grain, where this happens the domains are met by another set (or bundle) of domains with domain walls oriented along <112>$_{pc}$ directions (approximately perpendicular to the pore). The complete reconfiguration of domains before and after this heat cycle is shown in Figure 3.10 along with schematic images for ease of interpretation.

Domain reconfiguration in the other grains (1,2 and 4) displays a similar doubling in density of the bright contrast ferroelastic domains (bright in STEM image but grey in schematic) after cooling through T_c. This domain reconfiguration can be rationalised in terms of the obvious alterations in geometry and relaxation of out-of-plane constraint from cutting this lamella from the bulk ceramic. Most likely, the bright contrast domains have a larger component of polarisation in-the-plane of the lamellar surface allowing the annihilation of a large proportion of the dark contrast domains which likely have a larger out-of-plane component in comparison.
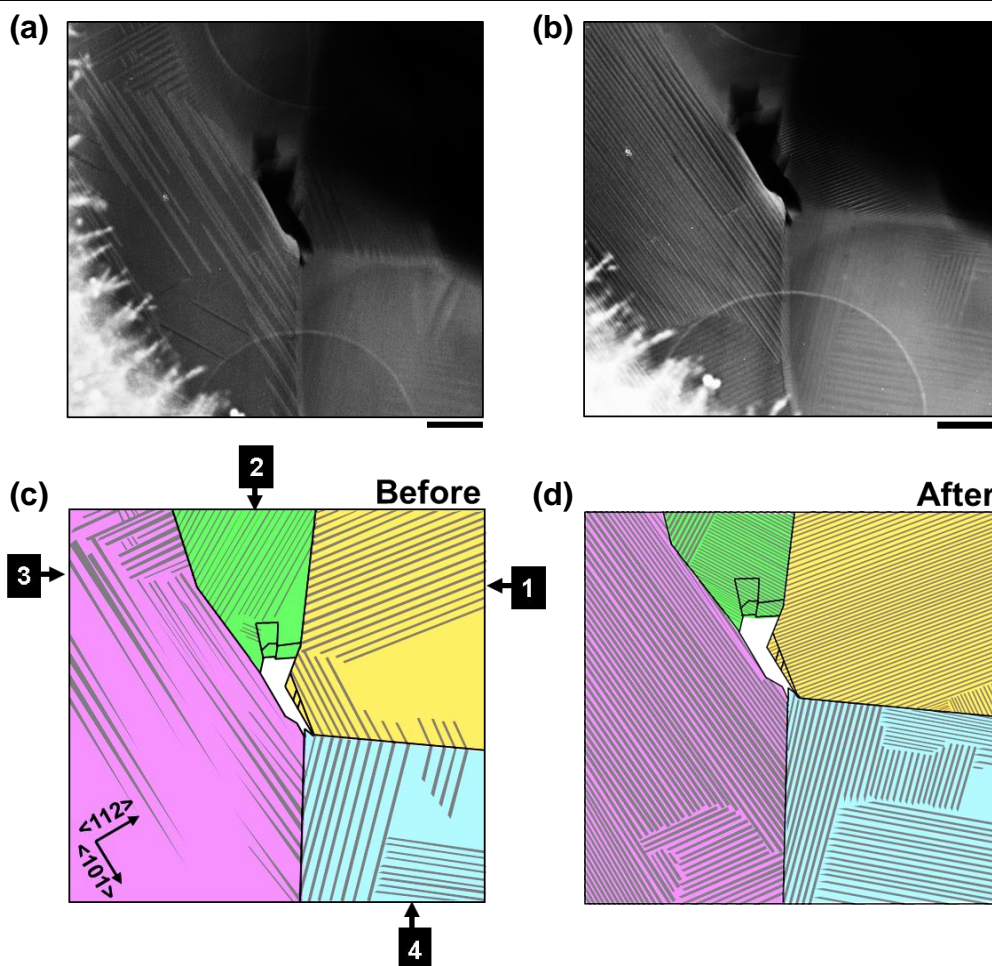
Figure 3.10: STEM images of before (a) and after (b) the first in-situ heat cycle shown in Figure 3.9. Schematics for ease of interpret show before (a) and after (b) the heat cycle. Scale bars represent 500nm.

The periodicity of the bright contrast domains was further investigated in Figure 3.11 where the domain width was measured in relation to position along the linescan shown in blue before (Figure 3.11a) and in red after the first heat-cycle (Figure 3.11b). The linescan was positioned so that the domain width could be measured starting at the junction (pore) and ending at the centre of grain 3. It can be assumed that the area nearest to the pore is much thinner than the rest of the grain [36, 37] and therefore provides a thickness gradient transitioning to the

centre of the grain. With this in mind, the relation between domain width and position along the linescan shown in Figure 3.11c can be rationalised in terms of the thickness gradient observations made by Mc Gilly et al. [38] where if the thickness gradient is perpendicular to the orientation of the domain walls (which
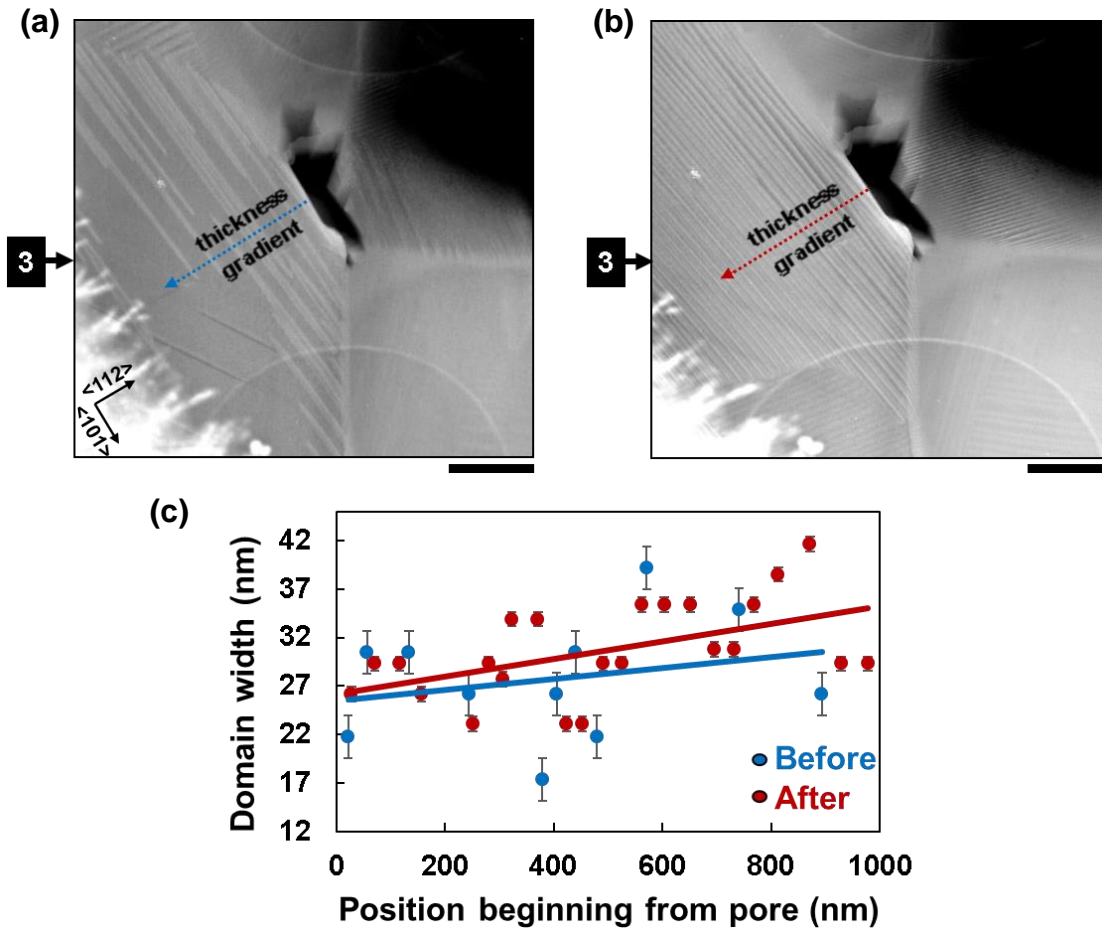
Figure 3.11: STEM magnified image of grain 3 before (a) and after (b) the first heat cycle. Relation between width of the bright contrast domains (domain walls along <101>pc directions) and position from the junction (pore) (c). Scale bars represent 500nm.

in Figure 3.11 it is) the domain width (w) increases continuously in a linear fashion, consistent with Kittel's relation [24]:

$$w_{min} = \sqrt{\gamma \frac{d}{U}} \tag{3.44}$$

where the electrostatic charge is considered as a surface energy density, U, the domain wall energy density is γ and the thickness of the lamella is d.

The reconfiguration of domains on cycling through T_c was further investigated by varying the speed of the ramp and de-ramp of temperature. Figure 3.12a shows the domain reconfiguration at the grain boundary between grains 3 and 4 after a relatively quick but continuous heat-cycle: 25°C-210°C-25°C (8°C/sec). Two things are noticeable when comparing Figure 3.12a with the after image of the first heat cycle in Figure 3.10b. Firstly, in grain 3, more of the domains which span the length of the grain fail to propagate as far as the lower grain boundary between grains 3 and 4. Instead, a group of domains with perpendicular domain walls (along <112>$_{pc}$ directions) propagate towards what appears to be a dislocation (circled in yellow).It is well known that dislocations can act as pinning sites for domain wall motion under the application of electric field [39] and therefore, some insight into this observed phenomenon may be gained by considering the thermodynamics of domain wall motion by dislocations, analogous to reported modelling of domain wall pinning by the application of electric field and shear stress [40]. The second thing to notice in Figure 3.12a is that in grain 4, the favourable domain wall orientation has changed after this heat cycle. The fact that grain 4 occupies an approx. 90° sector means that it can produce two distinct strains along its two constrained grain boundaries
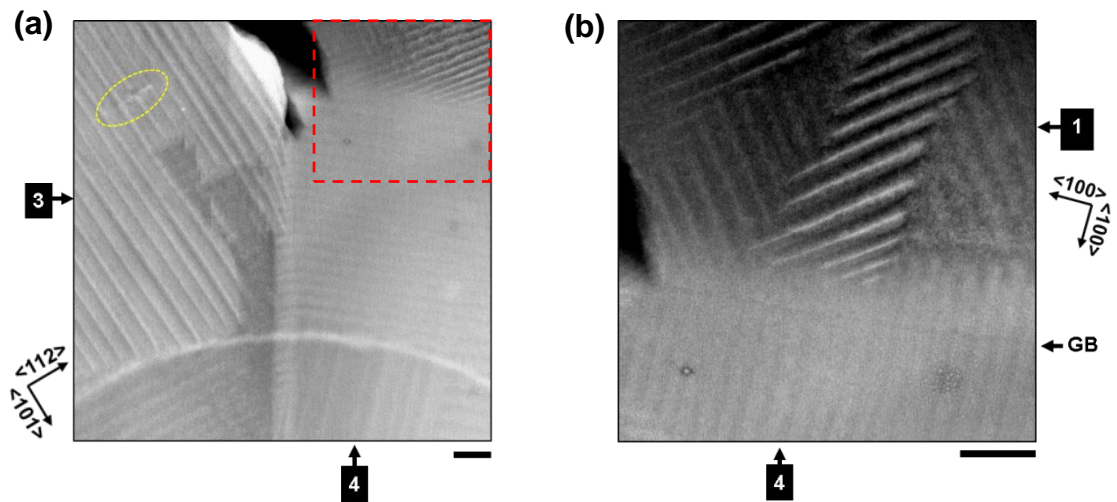
Figure 3.12: STEM images of domain reconfiguration after the 2nd in-situ heat-cycle (a): 25°C-210°C-25°C (8°C/sec). Domain reconfiguration in the area marked by a red box in (a) after the 3rd heat-cycle (b): 25°C–200°C (10°C/sec) - wait 10sec - 200°C–25°C(175°C/sec). Scale bars represent 100nm.

and has a wider freedom to vary these by having multiple favourable domain arrangements. In contrary, grains which occupy either narrow, or near 180° (like grain 3), sectors are likely to adopt one favourable domain arrangement to maximise its change in axial strain over a small rotation, and therefore this domain arrangement does not vary significantly after subsequent heat-cycles.

A third type of heat-cycle was carried out in which the temperature was ramped up to 200°C continuously (10°C/sec) and then 10 seconds were waited before the temperature was ramped down to room temperature in a very rapid quench (175°C/sec). The effect of this hasty transition through T_c back to room temperature meant that the condition of the lamella surface deteriorated quite rapidly (carbon contamination build up) but also, interesting areas of domain bundles like that shown in Figure 3.12b were created in several locations

throughout grains 1-4. These complex domain bundles bear resemblance to the superdomains observed by McGilly and McQuaid et al. [26, 41]. It is probable that the quick quench of the cooling within this heating cycle lead to multiple nucleation sites of ferroelastic domains, leading to attractively intricate bundle patterns were groups of domains intersected.

3.5 Conclusion

While domain configurations in polycrystalline ceramics have been reported previously, as of yet, there has been no explicit rationalisation for how compatible domain patterns arise at grain boundaries or any such prediction, or calculation, of compatible domain arrangements likely to form. Consequently, the results within this chapter represent an advance in understanding in ferroelastic domain formation and compatibility in polycrystalline ferroics. The analysis using theory of martensite crystallography of a single grain boundary demonstrated that the domains intersecting the grain boundary do on average arrange themselves in a compatible and stress-free manner. This result spurred on the identification and creation of a computational calculation which solved for a compatibility solution of domain wall orientations and domain fractional volumes likely to form within grains arranged around a junction (or pore). The investigation was expanded by carrying out STEM in-situ heating experiments which explored the rescaling and reconfiguration of ferroelastic domains on heat-cycling through T_C. It was shown that the domain density increased after the first heat-cycle through T_C and the presence of more intricate domain bundles increased when the temperature was

cooled back to room temperature in a quick quench-like fashion. Overall, it is thought that the results within this chapter offer an advancing insight into the nature of ferroelastic domains coupling across grain boundaries within polycrystalline ceramics.

3.6 References

[1] G. Arlt, *Ferroelectrics.* **1990**, *104*, 217-227.

[2] G. J. Weng, D. T. Wong, *J. Mech. Phys. Solids.* **2009**, *57*(3), 571-597.

[3] N. Liu, Y. Su, G. J. Weng, *J. Appl. Phys.* **2013**, *113*(20), 204106.

[4] S. Park, S. Wada, L. Cross, T. Shrout, *J. Appl. Phys.* **1999**, *86*(5), 2746-2750.

[5] S. Wada, K. Muraoka, H. Kakemoto, T. Tsurumi, H. Kumagai, *Ferroelectrics.* **2005**, *319*, 127-134.

[6] J. Yin, W. Cao, *J. Appl. Phys.* **2002**, *92*(1), 444-448.

[7] J. Roedel, *Mech. Mater.* **2007**, *39*(4), 302-325.

[8] K. Bhattacharya, *"Microstructure of martensite, why it forms and how it gives rise to the shape-memory effect"*, Vol. Volume 2 of Oxford Series on Materials Modelling, Oxford Materials, Oxford **1991**.

[9] K. Franke, J. Besold, W. Haessler, C. Seegebarth, *Surf. Sci.* **1994**, *302*(1-2), L283-L288.

[10] A. Gruverman, O. Auciello, H. Tokumoto, *Appl. Phys. Lett.* **1996**, *69*(21), 3191-3193.

[11] J. F. Scott, *Ferroelectrics.* **1996**, *183*, 51-63.

[12] A. Gruverman, O. Auciello, H. Tokumoto, *Annual Review of Materials Science.* **1998**, *28*, 101-123.

[13] A. Gruverman, H. Tokumoto, A. Prakash, S. Aggarwal, B. Yang, M. Wuttig, R. Ramesh, O. Auciello, T. Venkatesan, *Appl. Phys. Lett.* **1997**, *71*(24), 3492-3494.

[14] M. Demartin, D. Damjanovic, *Appl. Phys. Lett.* **1996**, *68*(21), 3046-3048.

[15] D. M. Marincel, H. Zhang, A. Kumar, S. Jesse, S. V. Kalinin, W. M. Rainforth, I. M. Reaney, C. A. Randall, S. Trolier-McKinstry, *Advanced Functional Materials.* **2014**, *24*(10), 1409-1417.

[16] B. J. Rodriguez, S. Choudhury, Y. H. Chu, A. Bhattacharyya, S. Jesse, K. Seal, A. P. Baddorf, R. Ramesh, L. Chen, S. V. Kalinin, *Advanced Functional Materials.* **2009**, *19*(13), 2053-2063.

[17] S. Choudhury, Y. L. Li, Krill, C., III, L. Q. Chen, *Acta Materialia.* **2007**, *55*(4), 1415-1426.

[18] D. Hall, A. Steuwer, B. Cherdhirunkorn, T. Mori, P. Withers, *J. Appl. Phys.* **2004**, *96*(8), 4245-4252.

[19] G. Arlt, D. Hennings, G. Dewith, *J. Appl. Phys.* **1985**, *58*(4), 1619-1625.

[20] F. Griggio, S. Trolier-McKinstry, *J. Appl. Phys.* **2010**, *107*(2), 024105.

[21] J. F. Ihlefeld, A. M. Vodnick, S. P. Baker, W. J. Borland, J. Maria, *J. Appl. Phys.* **2008**, *103*(7), 074112.

[22] Y. Ivry, D. Chu, J. F. Scott, C. Durkan, *Advanced Functional Materials.* **2011**, *21*(10), 1827-1832.

[23] Y. Shu, *Archive for Rational Mechanics and Analysis.* **2000**, *153*(1), 39-90.

[24] C. Kittel, *Phys. Rev*. **1946**, *(70)*, 965-971.

[25] A. Schilling, R. M. Bowman, J. M. Gregg, G. Catalan, J. F. Scott, *Appl. Phys. Lett.* **2006**, *89*(21), 212902.

[26] L. J. McGilly, *QUB PhD Thesis, "Domain Topologies in Nanoscale Single-Crystal Ferroelectrics"*, **2011**.

[27] Y. Shu, K. Bhattacharya, *Philosophical Magazine B-Physics of Condensed Matter Statistical Mechanics Electronic Optical and Magnetic Properties.* **2001**, *81*(12), 2021-2054.

[28] J. Li, D. Liu, *J. Mech. Phys. Solids.* **2004**, *52*(8), 1719-1742.

[29] P. R. Potnis, N. Tsou, J. E. Huber, *Materials.* **2011**, *4*(2), 417-447.

[30] B. Jaffe, W. R. Cook, H. Jaffe, "*Piezoelectric ceramics"*, Vol. 20, 4th edn., Elsevier, London and New York **1971**.

[31] J. Hadamard, "*Le̵cons sur la Propagation des Ondes et les Equations de l'Hydrodynamique"*, Re-issued (1949), Chelsea Publishing Company, New York **1903**.

[32] J. Ball, C. Carstensen, *Materials Science and Engineering A-Structural Materials Properties Microstructure and Processing.* **1999**, *273*, 231-236.

[33] W. Zhou, H. F. Greer, *European Journal of Inorganic Chemistry.* **2016,** (7), 941-950.

[34] J. Ricote, R. Whatmore, D. Barber, *Journal of Physics-Condensed Matter.* **2000**, *12*(3), 323-337.

[35] D. Hill, H. Tuller, "*Ceramic Sensors: Theory and Practise, Ceramic Materials for Electronics"* (Ed: R. Buchanan), Marcel Dekker Inc., NY **1991**.

[36] F. A. Martinsen, B. K. Smeltzer, M. Nord, T. Hawkins, J. Ballato, U. J. Gibson, *Scientific Reports.* **2014**, *4*, 6283.

[37] E. Holmstrom, J. Kotakoski, L. Lechner, U. Kaiser, K. Nordlund, *Aip Advances.* **2012**, *2*(1), 012186.

[38] L. J. McGilly, T. L. Burnett, A. Schilling, M. G. Cain, J. M. Gregg, *Physical Review B.* **2012**, *85*(5), 054113.

[39] P. Gao, J. Britson, C. T. Nelson, J. R. Jokisaari, C. Duan, M. Trassin, S. Baek, H. Guo, L. Li, Y. Wang, Y. Chu, A. M. Minor, C. Eom, R. Ramesh, L. Chen, X. Pan, *Nature Communications.* **2014**, *5*, 3801.

[40] A. Kontsos, C. M. Landis, *Int. J. Solids Structures.* **2009**, *46*(6), 1491-1498.

[41] R. G. P. McQuaid, *QUB PhD Thesis,* "Domain Patterns and Domain Wall Dynamics in Small-Scale Ferroelectrics", **2012**.

4. Relating domain structure to chemical heterogeneity and ceramic functionality

In this chapter interest is directed towards the relation between domain structure, chemical heterogeneity and the functional properties exhibited by the polycrystalline ferroelectric under investigation. In functional ceramics, the processing conditions can often lead to chemical heterogeneity or strain effects which understandably can have an impact on the resulting ceramic performance. The polycrystalline ferroelectric under investigation here is a $BaTiO_3$-based ceramic displaying a positive temperature coefficient of resistivity (PTCR) effect. Despite being of wide commercial use (in devices such as self-regulating heaters and smart fuses), the orders of magnitude increase in resistance that can be seen in $BaTiO_3$-based ceramics on heating through T_C, is far from well understood [1]. Current understanding hinges on the role of grain boundary resistance that can be modified by polarisation discontinuities which develop in the ferroelectric

state [2], and the magnitude of the switch appears to be optimised through trial and error changes in the processing conditions [3, 4]. Given the polydomain nature of the ceramic under investigation, as discussed in the previous chapter, and the fact that it is commercially available as a PTCR, a full chemical analysis relating the domain structure to the functionality was considered of interest.

This experimental study begins by showing a direct visualisation of resistive grain boundaries, which has rarely been attempted [5-7], using Kelvin probe force microscopy. Following this, aberration-corrected scanning transmission electron microscopy and electron energy loss spectroscopy reveals new evidence of Pb-rich grain boundaries associated with an increased local polarisation in the domains adjacent to the grain boundaries. The clarity of the results shown here validate the link between optimised PTCR performance and high local polarisation at grain boundaries, and suggests a novel route towards engineering devices where an interface layer of higher spontaneous polarisation could lead to vastly enhanced PTCR functionality.

This chapter features work carried out in collaboration with Prof. Q. Ramasse and Dr. D. Kepaptsoglou at SuperSTEM: The EPSRC National Facility for Aberration Corrected STEM, as well as KPFM data courtesy of Dr. A. Douglas at QUB and is published in 'Applied Physics Letters Materials' as:

4.1 Overview of the PTCR effect

The Positive Temperature Coefficient of Resistivity (PTCR) effect is a property found in polycrystalline materials which produce a switch from a low resistance semiconducting state to a higher state of resistance in response to either internal/external heating (Figure 4.1). Understandably, this effect has found extensive applications in sensing technologies such as self-regulating heating elements, current sensors and sensors for the detection of air flow, liquid level and temperature changes [8]. Among the various materials exhibiting a PTCR effect to date, the most favoured material group is $BaTiO_3$-based compounds where the temperature at which this switch in behaviour occurs, near the ferroelectric-paraelectric Curie transition temperature (T_c), and the magnitude of the switch can be controlled and optimised via the addition of different dopants and/or changes in the processing conditions [3, 4].
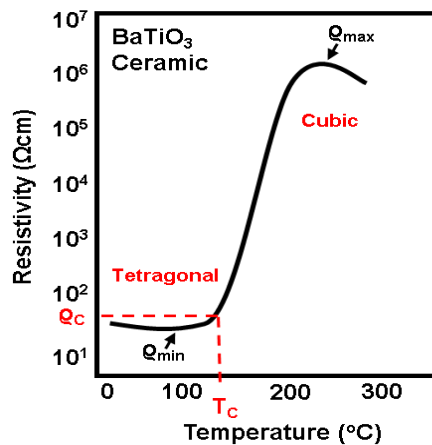

Figure: 4.1: Demonstration of the PTCR effect in a $BaTiO_3$-based ceramic. The resistivity jumps by around four orders of magnitude when the ceramic is heated through the tetragonal (ferroelectric) to cubic (paraelectric) phase transition temperature, T_c. Adapted from [9].

Over the past 50 years, research on the PTCR effect has focused on compositional and structural issues that govern the electrical properties [1, 10]. It was identified quite early that the effect is dominant in polycrystalline samples [11], with rich microstructures and an equally interesting domain structure embedded within grains, and several models have been proposed to explain the observed experimental behaviour [2, 12-14]. The most accepted among these models is the Heywang-Jonker model [1, 2, 12], which states that the presence of a potential barrier at the grain boundaries is responsible for enhanced resistivity of the boundary in comparison to the grain interior (see Figure 4.2a). The Heywang-Jonker model also considers the ferroelectric nature of the material (see Figure 4.2b) and postulates that the spontaneous polarisation below T_c, or more appropriately the polar discontinuity arising from domain structures, effectively lowers the potential barrier in the vicinity of the grain boundary, thus lowering the resistivities below T_c. As the material undergoes the ferroelectric-paraelectric transition, domains disappear and with no influence of polarisation, depletion regions and resistive barriers at the grain boundaries are restored leading to a high resistance state. The polarisation discontinuity at the boundary and its origin, particularly from the underpinning ferroelectric domain structure, have been an ongoing topic of debate in $BaTiO_3$-based PTCR ceramics [10, 15].

To investigate the ferroelectric nature and the local resistivity of grain boundaries, a commercially available PTCR ceramic composed of $BaTiO_3$-$PbTiO_3$-$CaTiO_3$ ($BaTiO_3$-$PbTiO_3$-$CaTiO_3$) was examined. The percentage concentrations are 68%, 20% and 12% respectively, with an average measured grain size diameter of 4μm. It is common to add Pb to $BaTiO_3$ PTCR ceramics to modify the T_c for

relevant applications [16], while Ca is employed to achieve refinement of grains [17].

(a) $> T_C$ **(b)** $< T_C$
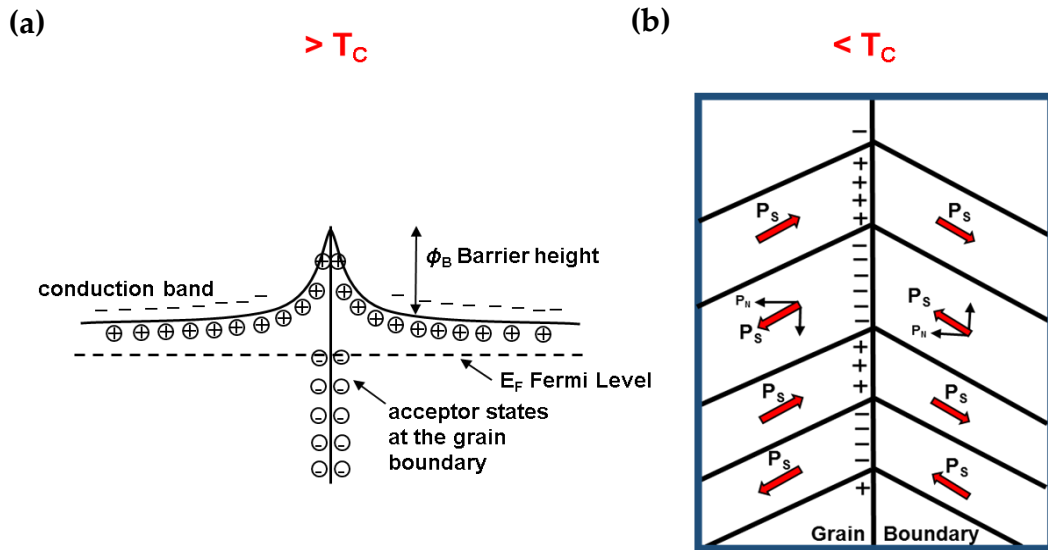
Figure 4.2: Heywang-Jonker model. Schematic of the potential barrier band structure at the grain boundary (a), after Heywang [12]. Schematic of domains, below T_c, lowering potential barriers along the grain boundary due to certain orientations of polarisation (P_s), after Jonker [2].

4.2 Observation of ferroelectric-ferroelastic domains in a BaTiO₃-based PTCR ceramic

The domains in this ceramic were observed via both PFM and low magnification TEM as an initial study. The PFM data in Figure 4.3 shows the presence of a rich microstructure of ferroelectric-ferroelastic stripe domains which have random orientational variation from grain to grain. This implies that the polarisation change across grain boundaries is highly inhomogeneous and varies from 0 to 2x

122
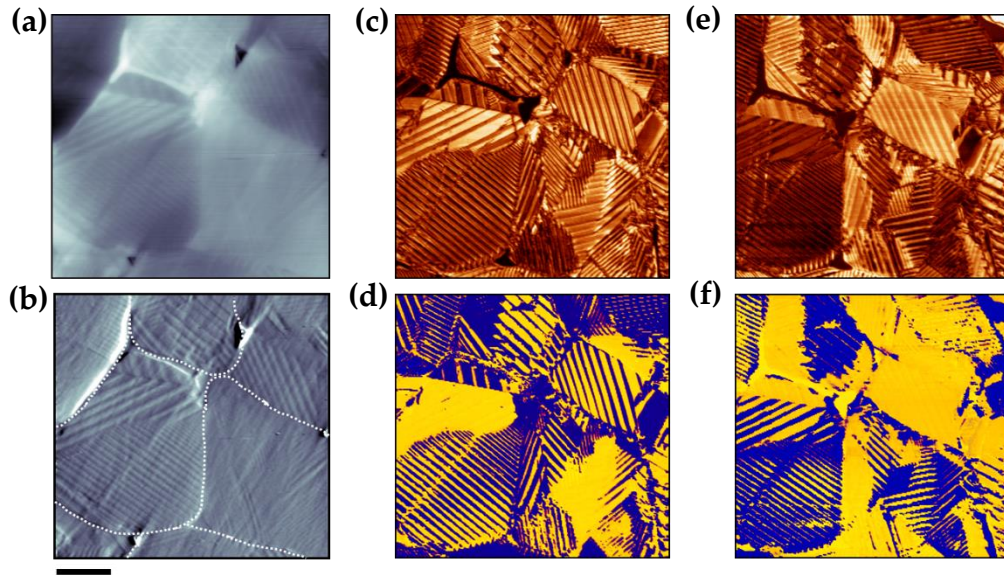
Figure 4.3: PFM imaging of ferroelectric-ferroelastic domains. A 10μm x 10μm scan of topography (a) and its derivative (b) of a polished $BaTiO_3$-$PbTiO_3$-$CaTiO_3$ sample. The scale bar represents 2 μm and the dashed lines in (b) mark the grain boundaries. The lateral PFM of amplitude (c) and phase (d), along with the vertical PFM of amplitude (e) and phase (f), show an intricate series of domains at the surface of each grain. Domains are clear in the derivative of topography. In both sets of PFM scans, 2 volts AC was applied, with the PFM amplitude scale of the lateral signal ranging from 0V to 4V, and 0V to 1V for the vertical. Figure courtesy of A. Douglas, more data can be found here [18].

spontaneous polarisation (P_s), corresponding with polar orientations varying from being parallel with to perpendicular to the grain boundary.

The intricate domain structure inside the grains is also noticeable in the STEM images of Figure 4.4, where a cross-sectional lamella containing multiple grains and grain boundaries was prepared via focused ion beam. Here, the grain in the centre (coloured purple in Figures 4.4a and b) was tilted to align the electron beam with <100>$_{pseudocubic (pc)}$ directions, as shown in the diffraction pattern (Figure

4.4c) acquired from the region highlighted by a dashed-circle in Figure 4.4a. The fine-scale domains within this grain can be identified as being 90° a-a domains
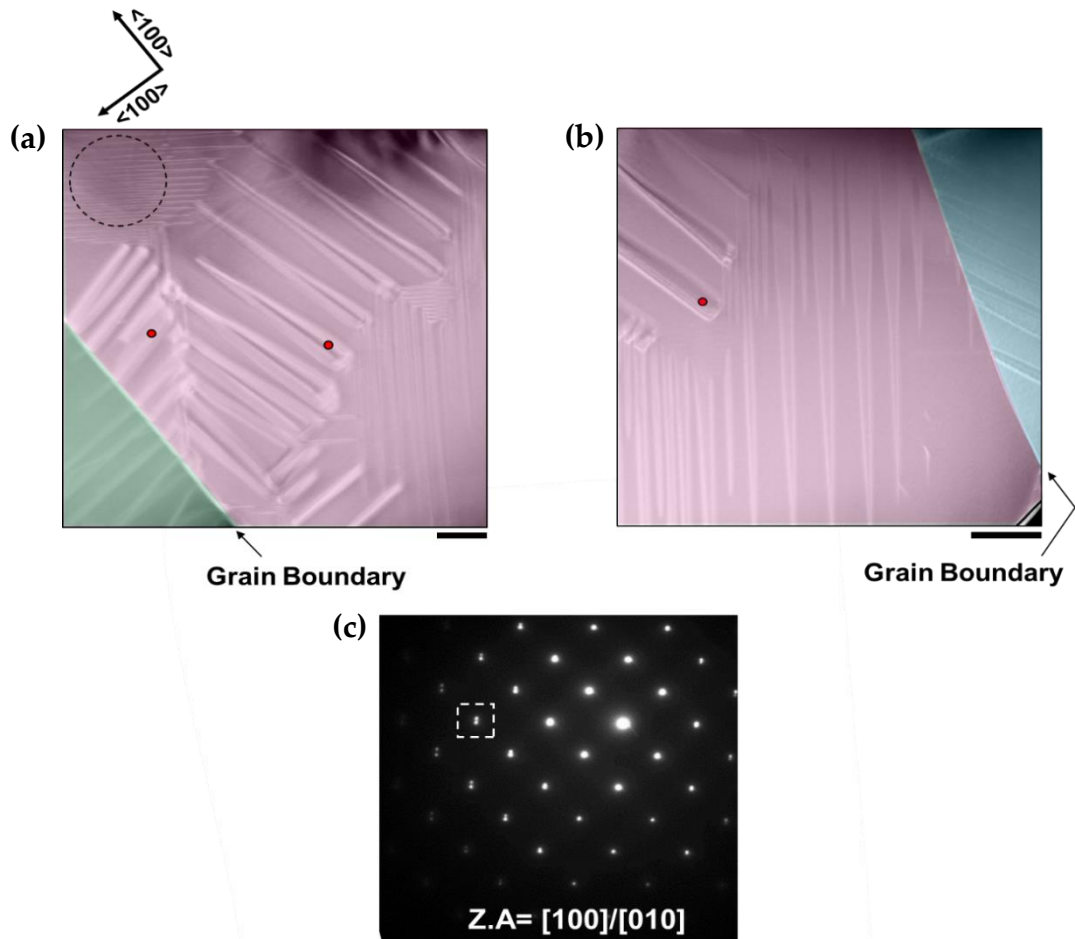
Figure 4.4: STEM imaging of ferroelectric-ferroelastic domains. Multiple grains (green, purple and blue) separated by grain boundaries (a) and (b). Electron diffraction pattern (c) acquired from the dashed circle (representing selective area aperture) in (a) with the electron beam oriented along the [100] (by symmetry could be [010]) zone axis. Occupation of the fine scale domain walls along {110}$_{pc}$ planes and splitting of the diffraction spots in (c) allows determination of the domains to be 90° a-a domain type. Additional ferroelectric-ferroelastic domains from overlapping grains (variants marked by red dots in (a) and (b)) add to the complexity of the rich polydomain microstructure observed within this ceramic. Scale bars represent 500nm.

due to the sharp domain walls occupying {110}$_{Pc}$ planes and the appearance of spot splitting, as demonstrated in Chapter 3, representing the crystal structure alteration brought about by the creation of ferroelectric-ferroelastic domains [19]. Strikingly though, in Figures 4.4a and b there appears to be additional domain variants present (those marked by red dots), domains with domain walls which do not occupy {110}$_{Pc}$ planes and whose domain wall widths appear to be broadly projected along this particular electron beam orientation. Mostly likely, these domains are originating from overlapping neighbour grains which were unknowingly included in the lamella during the FIB milling process, and like all ferroelastic domains are highly sensitive to STEM imaging.

The domain variants displayed in both the STEM and PFM images reveal a complex arrangement of ferroelectric-ferroelastic domains present in a small subset of what is a random orientational bulk ceramic. It is expected therefore, that a large range of polar discontinuities will be present at the grain boundaries based on the polydomain microstructure and the random nature of the grain boundary-crystallite orientations observed here.

4.3 Local resistivity of grain boundaries

The role of grain boundaries in enhanced PTCR behaviour has been strongly deliberated in previous studies; most of the experimental evidence is based on macroscopic studies such as impedance spectroscopy, which allows the interpretation of grain-boundary resistivity in terms of equivalent circuit diagrams [6, 7]. However, the use of large electrodes during macroscopic

investigations precludes the exact determination of the grain boundaries' role in the PTCR effect due to an averaging of their behaviour. It would appear obvious therefore that the cleanest way to gain experimental insight into the electrical behaviour of these elements would be to investigate them at a local scale, especially in a lateral geometry where the boundaries themselves form elements of the conduction circuit.

In this context, nanoscale studies aimed at visualisation of local resistivity or potential barriers at grain boundaries using scanning probe microscopy based techniques were carried out on the ceramic. Typically, the ceramic has relatively low bulk resistivity at room temperature (10-100 Ωcm) increasing by up to 4 orders of magnitude, on heating through T_c. Kelvin probe force microscopy (KPFM), a non-contact scanning probe microscopy technique was employed to establish the local resistivity of the grain boundaries. KPFM was performed on samples prepared from bulk by cutting and polishing using diamond paper and a colloidal silica solution. Figure 4.5a shows the resulting topography for the KPFM experiment, grain boundaries are highlighted with black dashed lines in a schematic of the scanned structure (Figure 4.5b) allowing for ease of reference. Au electrodes were sputtered, forming an inter-electrode gap of 80µm, to allow the application of an in-plane electric field whilst measuring the change in potential across the surface of the material.

During the experiment -10V DC was applied from the right electrode, with respect to the KPFM image, and in the 15µm region scanned a change in potential of roughly 1.5V DC was observed. Typically, when a lateral electric field is

applied to a material with homogeneous electrical properties the change in potential is linear but in this ceramic, the potential map in Figure 4.5c illustrates
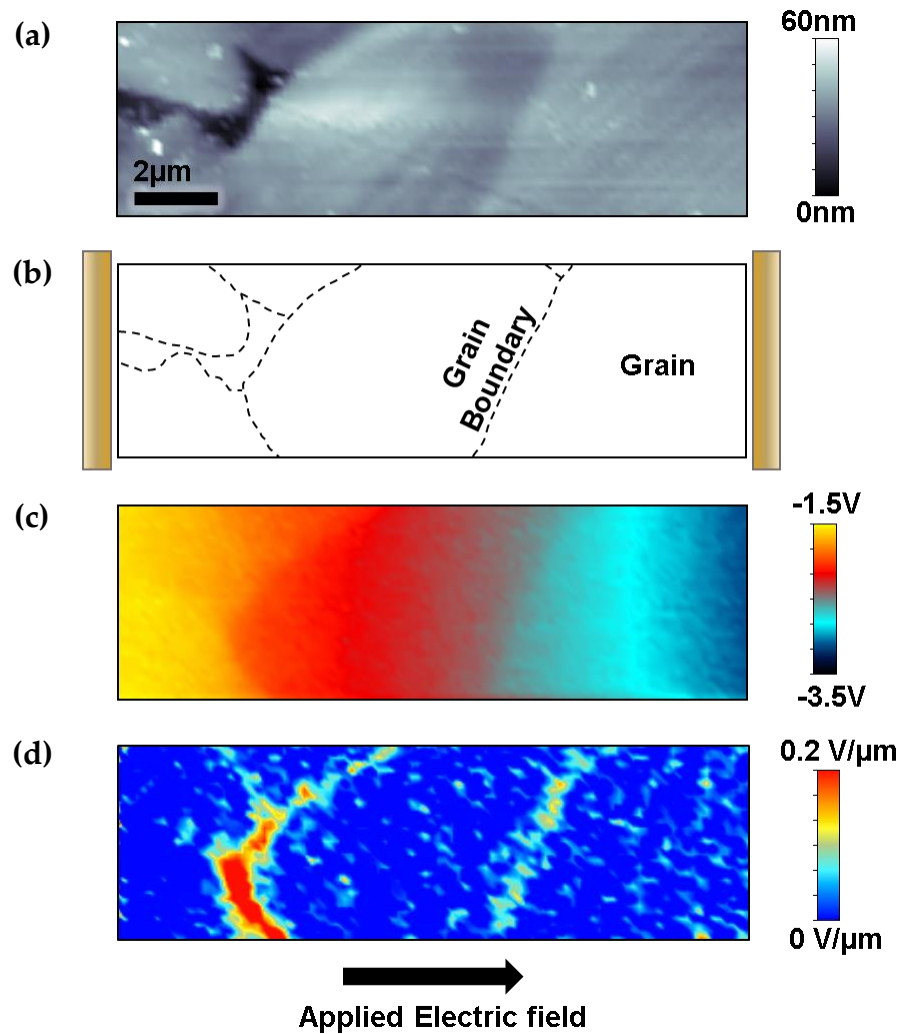
Figure 4.5: KPFM investigation of a polished BaTiO₃-PbTiO₃-CaTiO₃ sample. Topography of the surface for the KPFM experiment (15x5μm), with Au electrodes placed parallel to the vertical scan direction (a). Schematic of the scanned area (b). Potential map acquired by applying -10V across the surface of the sample, measured using KPFM (c) and negative gradient of the potential map (d). Figure courtesy of A. Douglas.

that there are distinct areas of non-linear change. To elucidate the exact location of the largest change in electrostatic potential, the negative gradient of the potential (electric field) along each horizontal scan line was calculated. Figure 4.5d reveals that the largest drop of potential occurs at the grain boundaries, a result which confirms that these interfaces are indeed much more resistive than the bulk (interior) of the grain.

The maximum height of the barrier at the grain boundaries can be estimated using the potential gradient differences inferred by KPFM mapping. Using a series resistance model, the ratio of the resistivities of the grain boundary (ρ_b) and the grain (ρ_g) is given by the ratio of the potential derivatives observed at them. The average value of this ratio as observed in Figure 4.5d is ~4. Using the Boltzmann distribution, the ratio of the resistivities at the grain and grain boundary can be expressed in terms of the barrier height (E_b), Fermi energy (E_F), carrier density in the grain (n_g) and carrier density at the grain boundary (n_b), as shown below:

$$\frac{\rho_b}{\rho_g} = \frac{n_g}{n_b} = \frac{e^{-\frac{E_c - E_F}{kT}}}{e^{-\frac{E_c + E_b - E_F}{kT}}} = e^{\frac{E_b}{kT}} \tag{4.1}$$

which implies,

$$E_b = kT \ln\left(\frac{\rho_b}{\rho_g}\right) = kT \ln(4) = 35.2 \text{ meV (at room temperature)} \tag{4.2}$$

This value of the barrier height at the grain boundary is estimated to be ~ 35 meV which is well within the range of thermal activation at room temperature. Overall the presence of resistive grain boundaries is consistent with models proposed for the electrical structure of the grains using impedance analysis [20] and other

techniques [5, 21]. While this result is almost expected based on various models, local measurements showing resistive boundaries at room temperature with an applied electric field in this lateral geometry have hitherto not been carried out directly. The concentration of potential contours at the grain boundaries provides direct evidence towards the existence of resistive boundaries and highlights them as the clear regions of interest. To further investigate the nature of these regions, their structural and chemical identity was studied on the atomic scale, using high resolution TEM techniques.

4.4 Elemental mapping of grain boundaries

Several studies have hinted towards chemical diffusion and segregation at the grain boundaries being linked with enhanced PTCR behaviour, but attempts to provide evidence of this chemical heterogeneity have so far been unsuccessful [22-24]. Moreover, the most accepted models do not consider links between chemical heterogeneity and polarisation discontinuity at grain boundaries [2, 12]. Therefore, there is an evident need to investigate the chemical distribution at the grain boundaries in these complex microstructures, and the modification of potential barriers while preserving the original domain structure at the interface.

As a first approach to study the chemical distribution electron energy loss spectroscopy (EELS) elemental maps were acquired. An overview of a typical specimen, a focused ion beam cross-section, containing several randomly oriented grains is shown in Figure 4.6a, with grain boundaries marked by white dashed lines. Representative boundaries, such as that in Figure 4.6b between

grains oriented in directions close to the [110] and [210] zone axes, were chosen. EELS maps were acquired on an aberration corrected Nion UltraSTEM 100 at SuperSTEM: The EPSRC National Facility for aberration corrected STEM. Rather than aligning the specimen along one of the main crystallographic axes, it was carefully oriented in the microscope to align the grain boundary parallel to the electron beam (edge-on, to unambiguously reveal the chemical changes across the boundary without projection effects). The microscope was operated in STEM mode at 100kV, equipped with a cold field emission gun and a Gatan Enfina spectrometer. A dispersion of 1 eV/channel was used to simultaneously acquire the Pb-M_4, Ba-$M_{4,5}$, Ti-$L_{2,3}$, Ca-$L_{2,3}$ and O-K edges; the resulting effective energy resolution was limited by the detector point spread function. The convergence and collection semi-angles were 32 and 37 mrad, respectively. The estimated t/mfp value was 0.29 (t~30nm (lamella thickness)), based on the integration of zero loss and plasmon peaks from low loss EELS data acquired immediately following the core-loss EELS acquisitions; consequently, it was deemed unnecessary to treat the data for multiple scattering effects and no further data processing was applied. Figures 4.6c-g reveal intensity maps (coloured and normalised to [0 1] for clarity) for the Pb-$M_{4,5,}$ Ba-$M_{4,5}$, Ti-$L_{2,3}$, Ca-$L_{2,3}$ and O-K EELS edges respectively. These maps were produced by integrating the intensity of the ionisation edges at each pixel over a suitable energy window (typically 40eV) beyond the edge onsets after subtraction of the continuous decaying background using a power law model.

The most striking feature of the EELS maps is the segregation of Pb, most obvious within a 10-15 nm region spanning across the grain boundary (Figure 4.6c), whilst Ba appears to be depleted within the same length scale (Figure 4.6d).

Meanwhile, elemental maps for the remaining elements (Ti, Ca and O) indicate a homogeneous chemical distribution (Figures 4.6e-g). The Pb segregation and Ba depletion observed here can be assumed to be attributed to A-site substitutions within the ABO$_3$ perovskite structure. Grain boundaries are well known for their
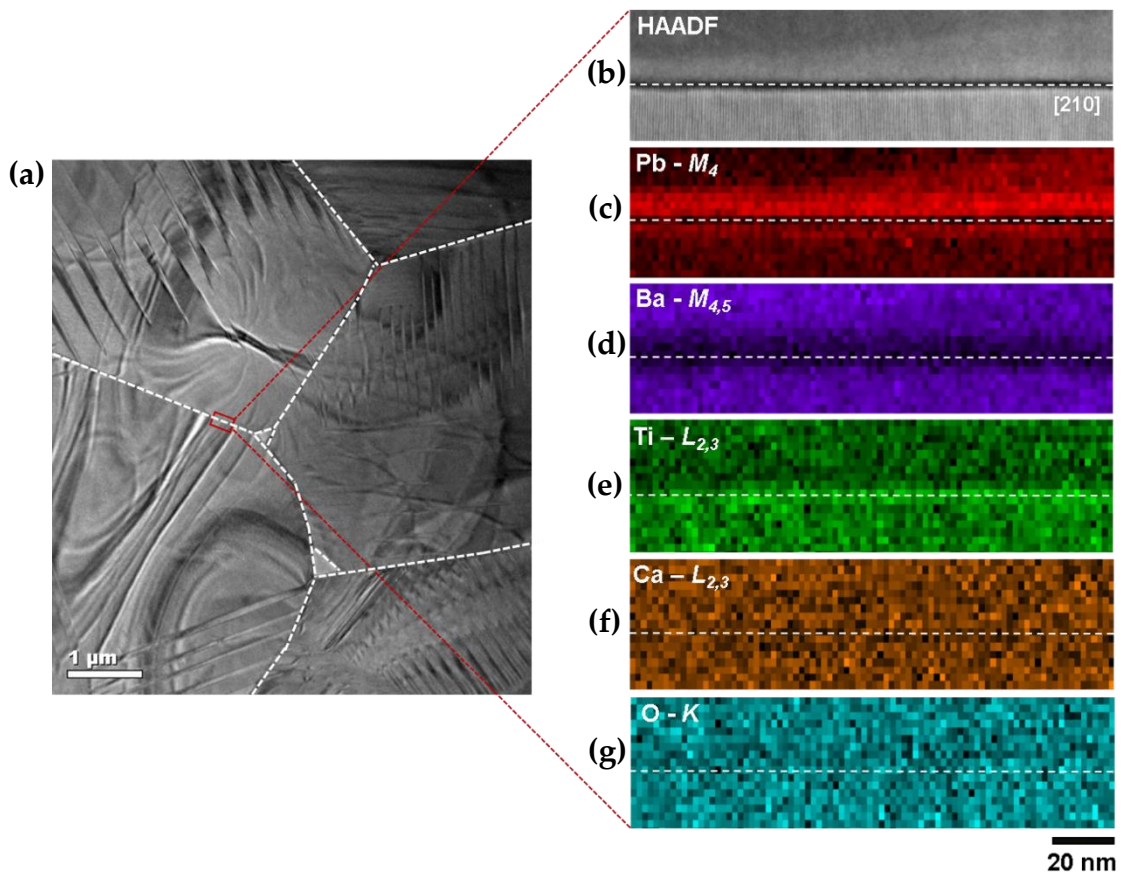
Figure 4.6: Chemical distribution across grain boundaries. Bright field TEM overview of various grains used for STEM-EELS analysis, where a polydomain structure can be seen within each grain (a). HAADF image of a single grain boundary where the bottom grain is tilted on zone axis (b). The grain boundary shows a dark contrast and is marked by a white dashed line. EELS elemental maps for Pb-M_4 (c) Ba-$M_{4,5}$ (d) Ti-$L_{2,3}$ (e) Ca-$L_{2,3}$ (f) and O-K (g), respectively.

disordered nature, formed by structural defects or dislocation cores [25], and Pb being more volatile could be attracted to these defective (and highly strained) areas during sintering [26], hence explaining the chemical heterogeneity observed here. It should be noted that the extent of Pb segregation could differ from one grain to another due to each grain developing slightly different strain gradients during the sintering process [27]. An example of this is observed in Figure 4.6c, where more segregation of Pb is observed in the top grain. Other grain boundaries were analysed, with different neighbouring grain orientations and relative tilt angles, all demonstrating similar results.

4.5 Electronic structure across grain boundaries

As previously mentioned, PTCR ceramics have rich microstructures that are highly sensitive to chemistry and processing conditions, making them complex ceramics to analyse. Previous studies have shown rich structural heterogeneity between grains, where grain boundaries with high lattice disruption and incoherency are a common feature [10]. This lattice disruption makes high resolution imaging of grain boundaries quite challenging, including direct mapping of the polarisation across them. However, another approach to access similar information is to study the local electronic structure through a detailed analysis of the Ti-O octahedral distortions. Hence, to determine the effect that chemical heterogeneity has on the electronic structure across the grain boundary, atomic-scale EELS measurements were carried out and more specifically, the electron-energy loss near-edge fine structure (ELNES) of the acquired spectra was

examined for changes indicative of electronic structure reconfiguration, focusing on the Ti and O signals.
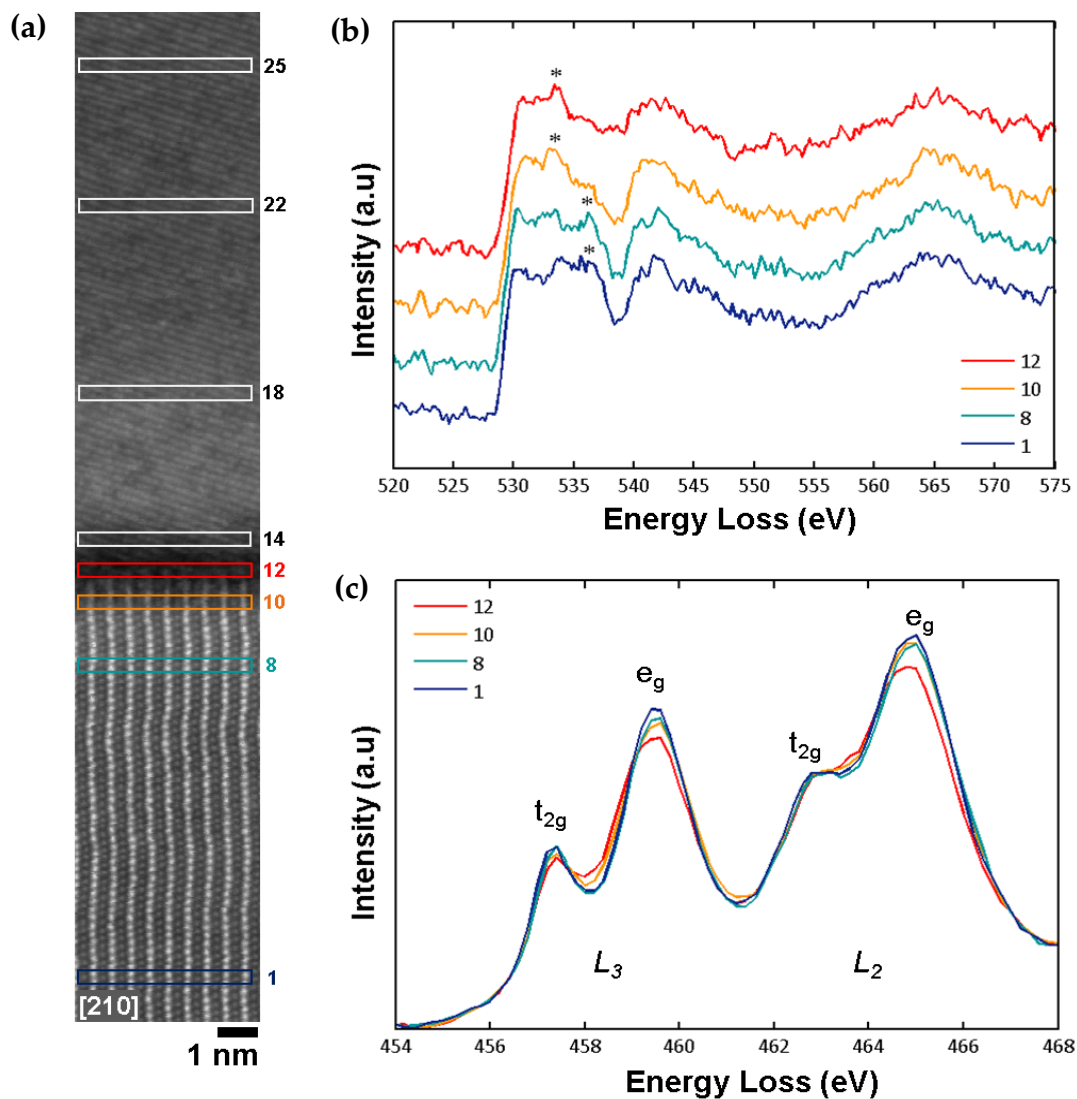
Figure 4.7: ELNES for O-*K* and Ti-*L*$_{2,3}$ edges. High resolution HAADF image of a single grain boundary (a) where spectra have been extracted from highlighted numbered regions. For clarity, only selected spectra are shown here but the full range can be seen in Figure 4.8. O-*K* edge (b) and Ti-*L*$_{2,3}$ edge (c) extracted from positions 1, 8, 10 and 12.

The Ti and O ELNES contain key information about octahedral distortions within the crystal structure as EEL spectra reflect the density of unoccupied states of the material, and can thus be used to identify changes in valence and atomic bonding [28-30]. Figure 4.7a is a high resolution high-angle annular dark-field (HAADF) image containing the grain boundary shown in Figure 4.6, where EEL spectra have been extracted from 25 positions. Each extracted spectrum spans over an average of eight unit cells, parallel to the interface. A dispersion of 0.2 eV/channel was used to acquire simultaneously the Ti and O edges resulting in an effective energy resolution of 0.58eV. The O-*K* edge shown in Figure 4.7b is perhaps the most challenging edge to characterise in oxides due to its multiple peaks that originate from the oxygen bonding to both A and B-site cations; however even subtle differences in the peaks represent a change in the chemistry and in the electronic structure [31].

The most striking feature observed here is a gradual shift in the peak marked with an asterisk. This peak is recognised to arise from the hybridisation of the O-*2p* orbitals with states attributed to the A-site cation [32], making it possible to distinguish a chemical transition in the A-site (Ba, Pb and Ca). The largest shift of this peak occurs on approaching the grain boundary, leading to a spectrum shape which has a remarkable resemblance to the O-*K* edge of bulk PbTiO$_3$ [32]. This shift confirms how the bonding nature of oxygen is altered as a function of the change in the A-site chemistry between the more BaTiO$_3$-like bulk-of-grain regions compared to the PbTiO$_3$-like grain boundary regions. To rule out any orientation effects influencing the ELNES the same area was measured twice, once with the bottom grain tilted onto zone axis, and once with the top grain tilted onto zone axis; similar features were seen either side of the grain boundary. For

completeness, spectra from both sides of the grain boundary in Figure 4.7 are presented in Figure 4.8.

Furthermore, we investigate changes in the crystal and electronic structure along the grain boundary by analysing the Ti-$L_{2,3}$ edge, associated to the Ti-O octahedral distortions. The splitting of the $L_{2,3}$ edge due to spin-orbit coupling is attributed to electron excitations from the Ti-$2p_{3/2}$ (L_3 edge) and $2p_{1/2}$ (L_2 edge) states into unoccupied Ti-$3d$ states near the Fermi level [31, 33, 34]. Due to the octahedral symmetry of the coulomb potential the L_3 and L_2 edges are each split into two further peaks representing the molecular orbitals e_g and t_{2g}, where the separation is known as the crystal field splitting (CFS) [35]. The lower energy t_{2g} orbitals point toward the faces of the TiO$_6$ octahedron (xy, xz and yz) whereas, the e_g higher energy orbitals point toward corners containing O anions ($d_{x^2-y^2}$ and d_{z^2}). It is well accepted that in a cubic symmetry crystal (e.g. SrTiO$_3$) [36, 37] the energies of the orbitals in the e_g peak are degenerate, presenting a single sharp peak. However, for a tetragonal symmetry (e.g. BaTiO$_3$, PbTiO$_3$), the e_g peak shows a clear splitting due to the breaking of degeneracy. Given that the EELS signal is highly sensitive to the subtle changes in the TiO$_6$ octahedron, we can expect a change in the Ti-$L_{2,3}$ edge between the BaTiO$_3$-like bulk-of-grain regions compared to the PbTiO$_3$-like grain boundary regions. The Ti-$L_{2,3}$ spectra (Figure 4.7c) show significant trends on approaching the grain boundary, such as a decrease in ratio between the t_{2g} and e_g peaks, and a broadening of the e_g peak, most obvious when comparing the spectrum from within the grain (position 1) and the grain boundary (position 12). Due to the energy resolution in experiment, the splitting of the e_g peak is not easily resolved, however it is well established that this splitting effect is observed as an e_g peak broadening [32, 36, 38].
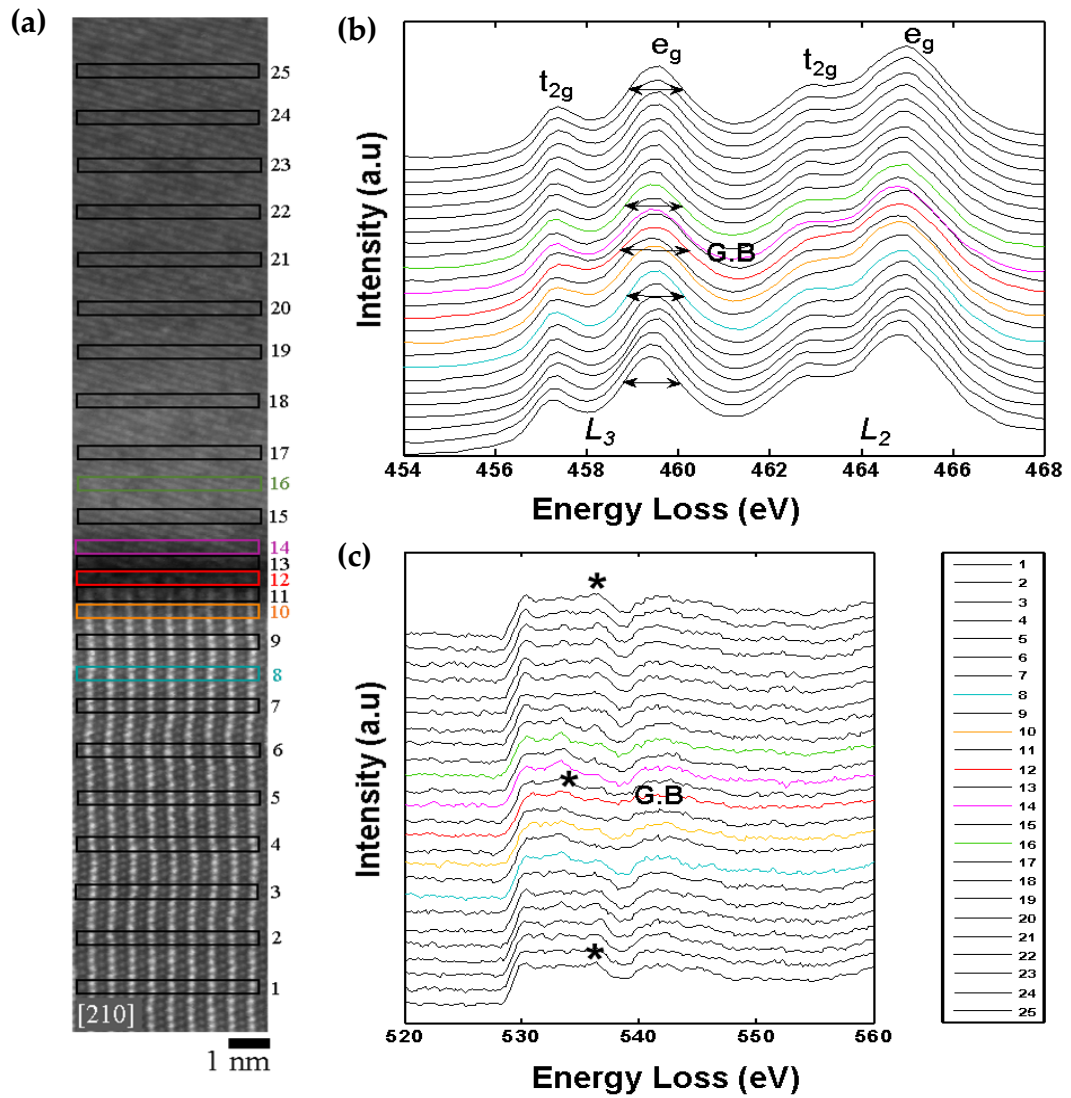
Figure 4.8: EEL spectra for both sides of a grain boundary, located around position 12 in (a), demonstrating symmetry in ELNES features. HAADF of single grain boundary (a). Ti $L_{2,3}$ edge (b); double sided arrows demonstrate the broadening of the L_3-e_g peak towards the grain boundary. O K edge (c); the asterisk marks the large peak shift on approaching the grain boundary.

As the e_g peak broadens the CFS is reduced and an inverse relationship between CFS and the average Ti-O bond length is established [37, 39]. Due to the

clear chemical inhomogeneity in this ceramic and the intrinsic change in symmetry between BaTiO₃, PbTiO₃ and CaTiO₃, the CFS is expected to change [31, 32, 37]. It has been shown that bulk BaTiO₃ has a higher CFS compared to bulk PbTiO₃ [36, 38], and therefore a quantitative analysis of the CFS across the grain boundary was carried out. The contribution from CaTiO₃ can be disregarded since the Ca content is constant. Figure 4.9 displays the CFS trend of the L_3 edge for each of the spectra positions in Figure 4.8. The CFS estimate of the L_3 edge is
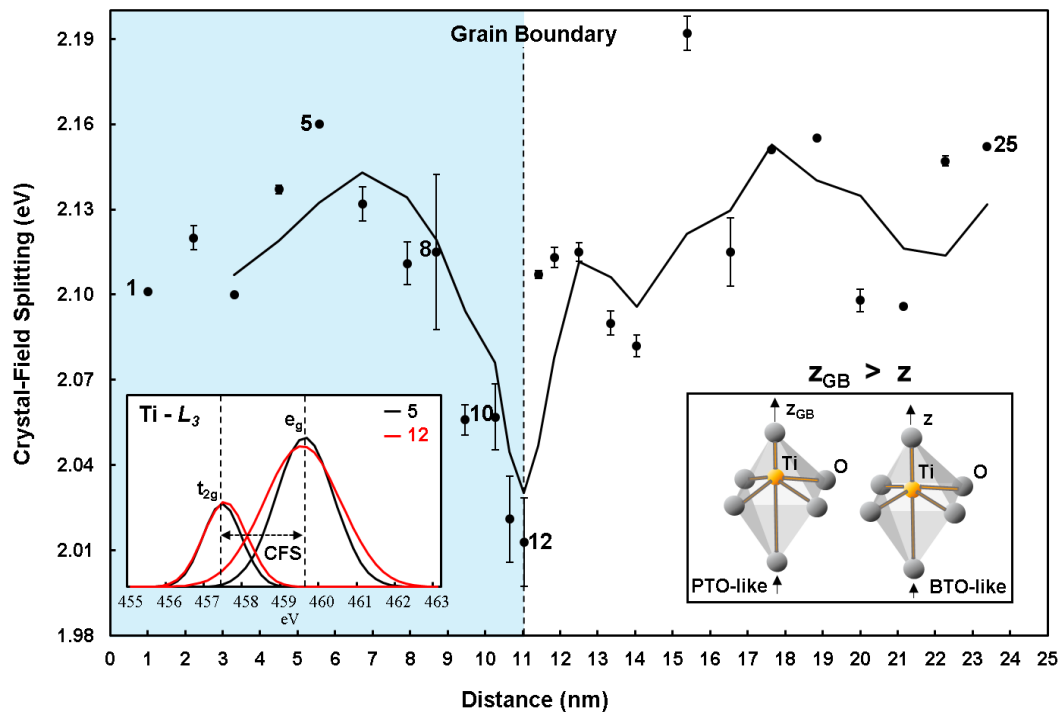
Figure 4.9: CFS of Ti-L_3 edge spanning 25 nm across the grain boundary presented in Figure 4.8. CFS was calculated by fitting Gaussian curves to the e_g and t_{2g} peak and measuring the centre-to-centre displacement, as exemplified in the left inset. Position markings are in reference to those in Figure 4.8. Schematics of octahedral distortion are depicted for the BaTiO₃-like and PbTiO₃-like regions in the right inset.

more accurate than that for the L_2 edge, due to a more accurate pre-edge background fitting and higher signal levels, and therefore only the former is shown in Figure 4.9. The CFS was calculated by fitting Gaussians to the respective peaks and measuring the centre-to-centre displacement (see left inset in Figure 4.9 as an example) with sub-pixel accuracy. From these measurements, a decrease in CFS is clearly observed approaching the grain boundary. The decrease in CFS (Δ 0.14 eV) confirms a tetragonal distortion of the TiO_6 octahedron, and points towards an enhanced noncentrosymmetric position of the Ti cation from the lowering of energy of the d_{z^2} orbitals [37], represented by L_3-e_g peak broadening. Thus, a transition between a $BaTiO_3$-like grain interior and a $PbTiO_3$-like grain boundary region has been further determined by a decrease in CFS.

The Ti valence state was also examined over various datasets by measuring the L_3/L_2 ratio. The method used followed that of D. H. Pearson et al. [29] which involves the isolation and normalisation of the $L_{2,3}$ intensities via an accurate background subtraction followed by the creation of a stepped continuum function using a double arctangent function, and subsequent integration of the edges over a suitable energy window (~5eV). Figure 4.10 displays two examples where the L_3/L_2 ratio was measured across the grain boundary shown in Figure 4.8 in two different locations (a few μm apart). Small changes in the L_3/L_2 ratio were observed; however, a variation from the characteristic Ti^{4+} oxidation state of $BaTiO_3$, $PbTiO_3$ and $CaTiO_3$ at the grain boundary was determined to be inconclusive since the L_3/L_2 ratio changes lay within the measurement error. The error was approximated by varying the integration energy window-width and continuum intensities systematically. The lack of evidence for a Ti valence change is not a surprising result given the complicated chemistry of this ceramic.
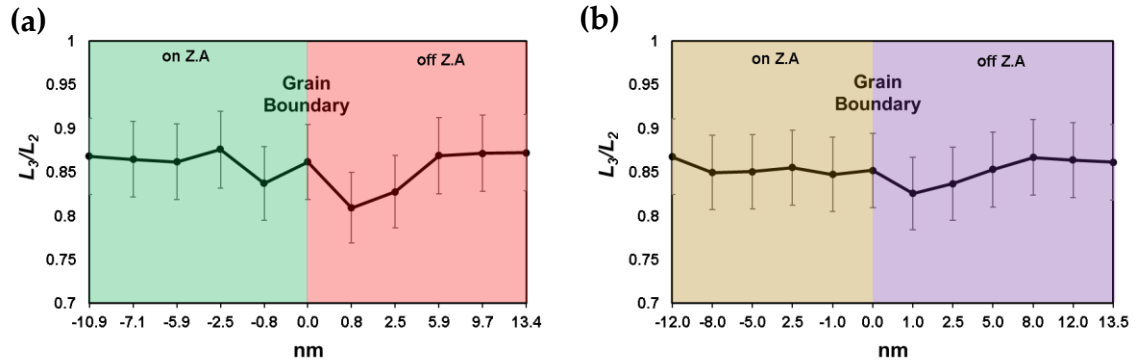
Figure 4.10: Ti L_3/L_2 ratio transitioning across the grain boundary in Figure 4.8. The L_3/L_2 ratio was measured at two different positions (a) and (b); the grain boundary is labelled by the interface between the two blocks of colour (representing grains), and the grains on zone axis (Z.A) and off zone axis are labelled.

4.6 Relating the chemical heterogeneity to polar discontinuities at grain boundaries

Even though BaTiO$_3$ and PbTiO$_3$ share a similar perovskite structure, they show drastic differences in spontaneous polarisation, BaTiO$_3$ having a magnitude of 26 μC/cm^2 and PbTiO$_3$ > 50 μC/cm^2 [40]. Therefore, it can be expected that PbTiO$_3$-like grain boundaries will have a higher net polarisation normal to the grain boundaries compared to the more BaTiO$_3$-like grain interior, creating a localised polarisation gradient. According to the modified Heywang-Jonker model [10], the barrier potential observed at the grain boundary is given by:

$$\phi = \frac{e^2 n_s^2 - (\Delta P_n^2 + \Delta P_z^2)}{8\,\varepsilon_r \varepsilon_0 n_0} \tag{4.3}$$

where n_s is the concentration of surface acceptor states, n_o is the concentration of charged species in the depletion layer, ΔP_n is the component of spontaneous polarisation normal to the grain boundary and ΔP_z represents the polarisation generated due to stresses at the grain boundaries as considered by Kulwicki and Purdes [14]. Crucially, it is the square of these changes in polarisation that matters in determining the effective grain boundary barrier height. Hence, for the same magnitude of polarisation discontinuity, the expected alteration in overall barrier potential would be the same irrespective of whether head-to-head (H-H) or tail-to-tail (T-T) domain configurations were present.

The reason why the magnitude of the polar discontinuity is accounted for in equation (4.3) would appear to be subtle: the barrier potential will vary across the area of the grain boundary and hence it will increase in some domains and decrease in others. However, the majority of the current will flow across the lowest barrier regions [2]. Therefore, the effective barrier across the grain boundary will be dominated by the lowest values of barrier potential and the regions of raised barrier height will be bypassed by the current. This is analogous to the net resistance in a bank of parallel resistors being dominated by the lowest individual resistant value. Polar discontinuities in polydomain grain boundaries will hence always act to lower the effective barrier across the boundary as a whole, resulting in the "$-(\Delta P)^2$" term in equation (4.3). Certainly, this analogy is only the case for ceramics which are strongly polydomain in nature. The PFM and STEM images in section 4.2 show that this is unquestionably the case for this ceramic.

Furthermore, the presence of a PbTiO$_3$-like phase approaching the grain boundary will contribute an increased magnitude of polarisation compared to the bulk, and hence further bring down the potential barrier at the grain boundary. In turn, this decrease in the potential barrier will result in a reduction of the resistivity as described by the equation:

$$\rho = A\exp\left(\frac{\phi}{k\mathrm{T}}\right) \qquad (4.4)$$

Upon undergoing the ferroelectric to paraelectric phase transition at T$_c$, where the spontaneous polarisation no longer exists, depletion regions and resistive barriers at the grain boundaries are restored leading to a high resistive grain boundary state. Thus, the existence of a PbTiO$_3$-like phase would suggest an enhanced spontaneous polarisation at the boundary, fully justifying the existence of the optimised PTCR effect in this commercially available ceramic.

4.7 Conclusion

Nanoscale microscopy techniques have been employed to establish the link between chemical heterogeneity and spontaneous polarisation across grain boundaries in a BaTiO$_3$-based commercially available PTCR ceramic: BaTiO$_3$-PbTiO$_3$-CaTiO$_3$. A segregation of Pb and a corresponding depletion of Ba near grain boundaries was observed. Furthermore, a decrease in CFS suggestive of octahedral distortion was identified via changes in Ti-$L_{2,3}$ and O-K ELNES features approaching the grain boundary, thus revealing a more PbTiO$_3$-like region within 10-15nm from the grain boundary. This work links the chemical and electronic

heterogeneity of the studied PTCR ceramic to the changes in potential barrier at the grain boundary, theorised by the Heywang-Jonker model. The results shown here have been evaluated on a specific ceramic composition but are relevant to the general family of polydomain PTCR ceramics [41]. The central idea that a confined interfacial region, with higher spontaneous polarisation that reduces the grain boundary barrier potential, augments electronic transport and enhances the magnitude of resistivity jump at T_c is novel by itself. While inferring an insight into the mechanistic origin of the reduction in potential barrier at grain boundaries in the low temperature ferroelectric phase, this idea also offers a novel route towards engineering PTCR ceramics in which an interface layer of higher spontaneous polarisation could be created to produce better performing PTCR devices.

4.8 References

[1] Y. L. Chen, S. F. Yang, *Advances in Applied Ceramics.* **2011**, *110*(5), 257-269.

[2] G. H. Jonker, *Solid-State Electronics.* **1964**, *7*(12), 895-903.

[3] D. Y. Wang, K. Umeya, *J Am Ceram Soc.* **1990**, *73*(3), 669-677.

[4] J. Nowotny, M. Rekas, *Ceram. Int.* **1991**, *17*(4), 227-241.

[5] S. M. Gheno, H. L. Hasegawa, P. I. Paulin Filho, *Cerâmica.* **2007**, *53*(326), 200-204.

[6] F. D. Morrison, D. C. Sinclair, A. R. West, *International Journal of Inorganic Materials.* **2001**, *3*, 1205.

[7] D. C. Sinclair, A. R. West, *Journal of Applied Physics.* **1989**, *66*, 3850.

[8] B. M. Kulwicki, *Journal of Physics and Chemistry of Solids.* **1984**, *45*(10), 1015-1031.

[9] J. Daniels, K. H. Hardtl, R. Wernicke, *Philips Technical Review*, **1979**, *(38)*, 73.

[10] R. D. Roseman, N. Mukherjee, *Journal of Electroceramics.* **2003**, *10*, 117-135.

[11] G. Goodman, *J. Am. Ceram. Soc.* **1963**, *46*, 48.

[12] W. Heywang, *Solid-State Electronics.* **1961**, *3*, 51.

[13] J. Daniels, R. Wernicke, *Philips Research Reports.* **1976**, *31*(6), 544-559.

[14] B. M. Kulwicki, A. J. Purdes, *Ferroelectrics.* **1970**, *1*, 253.

[15] J. E. Ralph, J. P. Gowers, M. R. Burgess, *Appl. Phys. Lett.* **1982**, *41*(4), 343-345.

[16] D. Hill, H. Tuller, in *Ceramic Sensors: Theory and Practise, Ceramic Materials for Electronics* (Ed: R. Buchanan), Marcel Dekker Inc. NY **1991**.

[17] D. Voltzke, H. P. Abicht, E. Pippel, J. Woltersdorf, *Journal of the European Ceramic Society.* **2000**, *20*(11), 1663-1669.

[18] A. M. Douglas, A. Kumar, R. W. Whatmore, J. M. Gregg, *Appl. Phys. Lett.* **2015**, *107*(17), 172905.

[19] S. Cheng, N. Ho, H. Lu, *J Am Ceram Soc.* **2006**, *89*(7), 2177-2187.

[20] D. C. Sinclair, A. R. West, *J. Mater. Sci.* **1994**, *29*(23), 6061-6068.

[21] P. Fiorenza, R. Lo Nigro, P. Delugas, V. Rainen, A. G. Mould, D. C. Sinclair, *Appl. Phys. Lett.* **2009**, *95*, 142904.

[22] L. Affleck, C. Leach, *Journal of the European Ceramic Society.* **2005**, *25*(12), 3017-3020.

[23] J. Hou, Z. Zhang, W. Preis, W. Sitte, G. Dehm, *Journal of the European Ceramic Society.* **2011**, *31*(5), 763-771.

[24] M. A. Zubair, C. Leach, *Journal of the European Ceramic Society.* **2010**, *30*(1), 107-112.

[25] P. Prabhumirashi, V. P. Dravid, A. R. Lupini, M. F. Chisholm, S. J. Pennycook, *Appl. Phys. Lett.* **2005**, *87*(12), 121917.

[26] M. Arredondo, Q. M. Ramasse, M. Weyland, R. Mahjoub, I. Vrejoiu, D. Hesse, N. D. Browning, M. Alexe, P. Munroe, V. Nagarajan, *Adv Mater.* **2010**, *22*(22), 2430-+.

[27] Q. Yin, B. Zhu, H. Zeng, in *Microstructure, property and processing of functional ceramics*, Metallurgical Industry Press: Springer Verlag, Berlin **2009**.

[28] L. A. Grunes, R. D. Leapman, C. N. Wilker, R. Hoffmann, A. B. Kunz, *Physical Review B.* **1982**, *25*(12), 7157-7173.

[29] D. H. Pearson, C. C. Ahn, B. Fultz, *Physical Review B.* **1993**, *47*(14), 8471-8478.

[30] J. Graetz, C. C. Ahn, H. Ouyang, P. Rez, B. Fultz, *Physical Review B.* **2004**, *69*(23), 235103.

[31] E. Stoyanov, F. Langenhorst, G. Steinle-Neumann, *Am. Mineral.* **2007**, *92*(4), 577-586.

[32] A. Torres-Pardo, A. Gloter, P. Zubko, N. Jecklin, C. Lichtensteiger, C. Colliex, J. Triscone, O. Stephan, *Physical Review B.* **2011**, *84*(22), 220102.

[33] R. D. Leapman, L. A. Grunes, P. L. Fejes, *Physical Review B.* **1982**, *26*(2), 614-635.

[34] F. M. F. Degroot, Z. W. Hu, M. F. Lopez, G. Kaindl, F. Guillot, M. Tronc, *J. Chem. Phys.* **1994**, *101*(8), 6570-6576.

[35] R. G. Burns, *Mineralogical applications of crystal field theory*, Cambridge University Press, New York **1970**.

[36] E. Eberg, A. T. J. van Helvoort, R. Takahashi, M. Gass, B. Mendis, A. Bleloch, R. Holmestad, T. Tybell, *J. Appl. Phys.* **2011**, *109*(3), 034104.

[37] D. Park, A. Herpers, T. Menke, M. Heidelmann, L. Houben, R. Dittmann, J. Mayer, *Microscopy and Microanalysis.* **2014**, *20*(3), 740-747.

[38] J. M. Zhang, A. Visinoiu, F. Heyroth, F. Syrowatka, M. Alexe, D. Hesse, H. S. Leipner, *Physical Review B.* **2005**, *71*(6), 064108.

[39] A. S. Sefat, G. Amow, M. Y. Wu, G. A. Botton, J. E. Greedan, *Journal of Solid State Chemistry.* **2005**, *178*(4), 1008-1016.

[40] M. E. Lines, A. M. Glass, *Principles and Applications of Ferroelectrics and Related Materials*, Oxford University Press, New York **1977**.

[41] K. M. Holsgrove, D. M. Kepaptsoglou, A. M. Douglas, Q. M. Ramasse, E. Prestat, S. J. Haigh, M. B. Ward, A. Kumar, J. M. Gregg, M. Arredondo, *Apl Materials.* **2017**, *5*(6), 066105.

5. Polymorphs reversed by external stimuli in mixed-phase BiFeO₃ thin films

In this chapter polymorphs within mixed-phase BiFeO₃ thin films are explored both structurally and dynamically under the application of external stimuli. The perovskite BiFeO₃ has become subject to intense investigation over recent years with initial interest surrounding the room temperature magnetoelectric multiferroic properties seen in thin films [1]. Not long after, it was experimentally confirmed that epitaxially strained BiFeO₃ has other fascinating properties, such as, a strikingly high spontaneous polarisation (~150µC/cm²) [2], above band-gap photovoltaic properties [3] and domain walls that, at least in some orientations, behave as pseudo-2D sheet conductors [4]; all while being an environmentally benign lead-free material. Additionally, research into the effect that epitaxial constraint (from substrate misfit) has on the unit cell structure of BiFeO₃ thin films has flourished. It was found that under particular epitaxial conditions and at specific thin film thicknesses, BiFiO₃ can present a mixture of two rather different

phases [5]. The coexistence of these two stabilised phases: one being highly-strained (tetragonal-like 'T' phase) and the other being more relaxed (rhombohedral-like 'R' phase), and the fact that they are separated by a strain-driven morphotropic phase boundary opens the door to a plethora of opportunities to tune the plasticity of thin films; the relative proportion of T and R polymorphs should be able to alter in a continuous manner in response to external stimuli, making a reversible switching process highly desirable.

To date, researchers have successfully demonstrated local transformations from R to T phase through the application of localised electric field [6] and heat [7]. On the other hand, a recent report using scanning probe-based stress-induced T to R phase transformations in the reverse sense to that seen when applying electric fields has been observed [8]; analogous to studies of stress-induced switching of nanodomains in ultrathin (<5 nm) films of $BaTiO_3$ [9]. These findings point towards the viability of reversible control between phases and raises the question of whether dual control can be gained by combining different applications of external stimuli.

In this chapter, the as-grown native mixed-phase state is firstly characterised using TEM techniques. Following this, the thermal activation phase transformation is explored through in-situ STEM heat-cycling experiments demonstrating a growth of the highly-strained T phase above 400°C. In a more controllable nature, via an AFM tip, a combinatorial approach demonstrates switching of the native mixed-phase state to a pure T phase state by applying electric field, and back again to a mixed-phase state by the nucleation of R polymorphs using localised stress. The combinatorial approach involving stress-

induced writing and electric field mediated reading of these polymorphs has potential for a mechanical-write-electrical read memory device. However, for such a technological device to be achieved, a quantitative thermodynamic framework based on the dynamics of phase switching under external stimuli needs to be developed. In addition, a complete knowledge of the crystal structure post-application of external stimuli is essential. In this chapter, energy-based effective Hamiltonian simulations demonstrate the phase competition under the application of electric-field and stress, directly compared to experimental data. Furthermore, a detailed TEM investigation of cross-sectional lamellae prepared from pre-written AFM regions reveals the unit cell structure and evolution of strain across stress-written polymorphs, allowing a direct comparison to the native mixed-phase state.

This chapter features work carried out by N. Browne and D. Edwards at QUB (AFM: experiments and analysis), Hamiltonian simulations by Prof. L. Bellaiche at University of Arkansas and FEFF calculated EEL spectra by Dr. M.S. Moreno at Bariloche Atomic Centre. Work within this chapter has resulted in the following manuscripts currently under preparation:

1. "Deterministic reversible control over symmetry states in mixed-phase BiFO₃ using electrical bias and uniaxial stress towards piezoresistive applications"

D. Edwards, N. Browne, **K. M. Holsgrove**, A. Naden, S. O. Sayedaghaee, B. Xu, S. Prosandeev, D. Wang, D. Mazumdar, A. Gupta, S.V. Kalinin, M. Arredondo, R. G. P. McQuaid, L. Bellaiche, J. M. Gregg, A. Kumar

2. "Atomic structure of native and stress-written phases in mixed-phase BiFO₃ thin films"

K. M. Holsgrove, M. Duchamp, M.S. Moreno, N. Bernier, N. Browne, D. Mazumdar, J. M. Gregg, A. Kumar, and M. Arredondo

5.1 The native mixed-phase state

The room-temperature bulk phase of BiFeO₃ (BFO) is classed as rhombohedral (point group R3c) [10], with unit cell lattice parameter of 3.965Å and ferroelectric polarisation along [111]$_{pc}$ directions [11]. In this study BFO was grown epitaxially on (001)-oriented LaAlO₃ (LAO) substrates with bottom LaSrMnO₃ (LSMO) or LaSrCoO₃ (LSCO) electrodes of 5 nm thickness. Details of the sample preparation have been reported elsewhere [12]. The compressive misfit strain (-4.4 %) imposed upon the BFO thin film by the LAO substrate (LAO is also rhombohedral at room temperature but has a smaller unit cell lattice parameter of 3.79 Å) allows the structural alteration of BFO into two different phases. The highly-strained phase (known as the 'T' phase) exhibits a tetragonal-like P4mm symmetry with a c/a ratio of ~1.2. The Fe displacement towards one of the apical oxygens along [001]$_{pc}$ results in fivefold oxygen coordinated Fe, owing to an enhanced polarisation roughly 1.5 times that of bulk BFO [13]. The more relaxed phase (known as the 'R' phase) resembles more to the rhombohedral R3c bulk BFO parent phase with a c/a ratio of ~1.08. The unit cell structure of the R phase includes octahedrally coordinated Fe, a ferroelectric distortion consisting of ionic

displacements along the [111]$_{pc}$ axis, and antiferrodistortive rotations of the FeO$_6$ octahedra around [111]$_{pc}$.

The native mixed-phase state in a 35 nm thick BFO thin film can be observed in the low-magnification STEM image of Figure 5.1a where the contrast variation between individual polymorphs can be used to identify the different phases. The unit cell structure of the R and T phase is shown schematically along with the schematic polarisation directions (black arrows) in Figures 5.1b and c, respectively. Identification of which polymorph contrast corresponds to the R phase (and the T phase) is routinely characterised by diffraction or HRTEM [14].
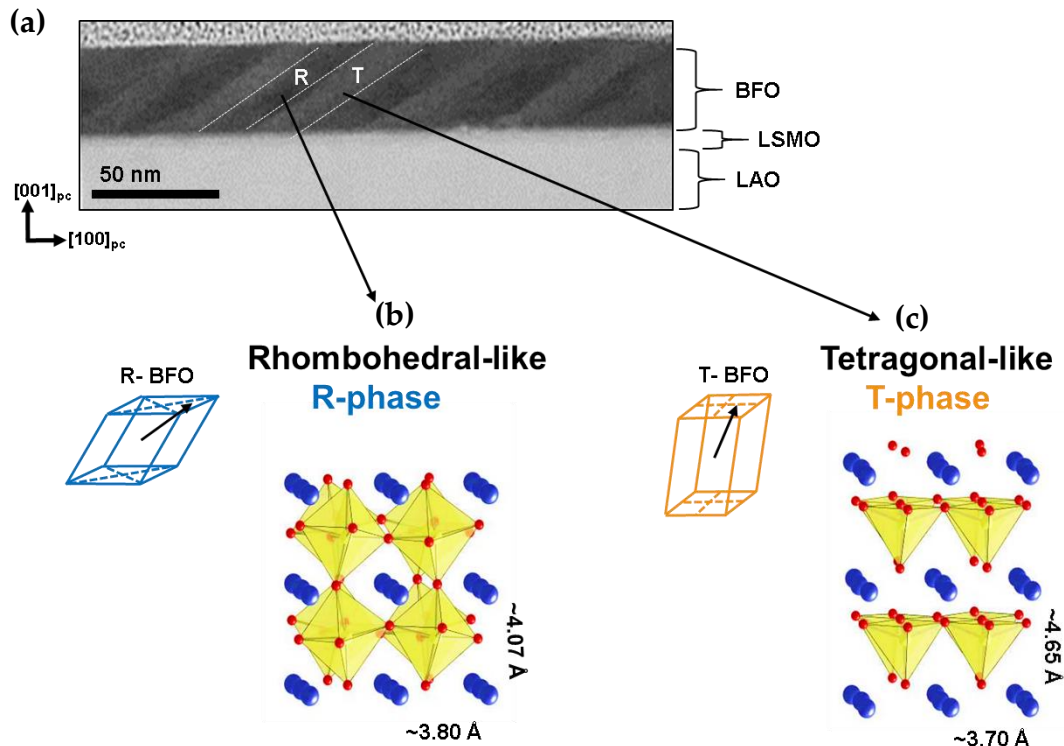
Figure 5.1: STEM-DF image of mixed-phase BFO in the native state (a). Schematic unit cell structure and polarisation directions of the R (b) and T (c) phases. (b) and (c) from [15].
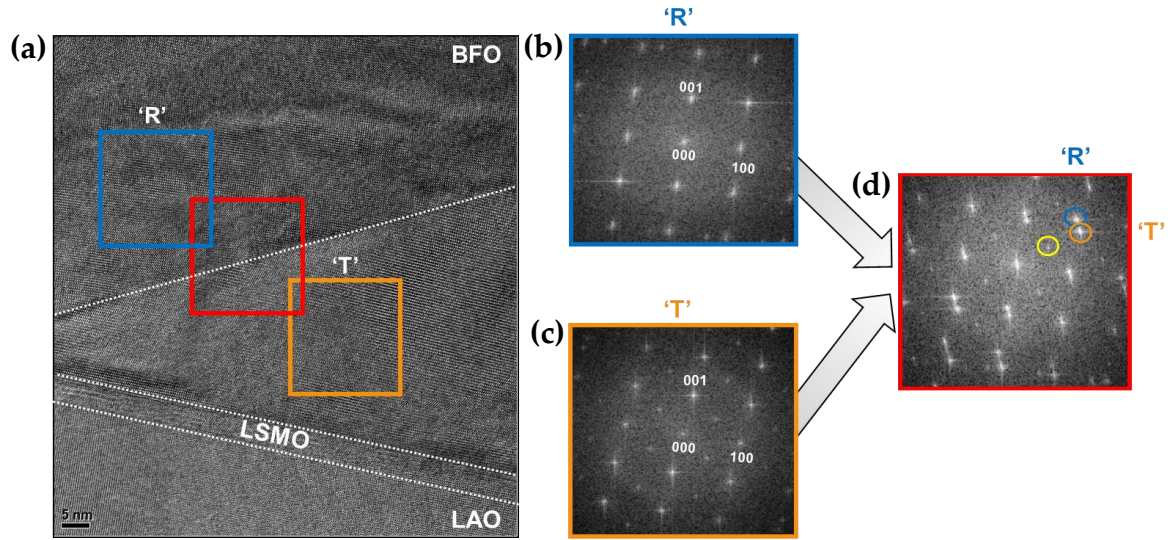
Figure 5.2: HRTEM image of a boundary between a R polymorph and T polymorph (a). Corresponding FFTs for R (b), T (c) and the boundary between R/T (d).

Figure 5.2a shows a HRTEM image of an R and T polymorph separated by a morphotropic phase boundary. The site specific fast Fourier transforms (FFTs) from the R phase (Figure 5.2b) and T phase (Figure 5.2c) display the structural identity of the respective unit cells. The FFT selected across the boundary (Figure 5.2d) highlights the reflections circled in blue and orange corresponding to the R and T phase, respectively. The reflection circled in yellow also belongs to the T phase, it is a half-integer spot in the FFT pattern, indicative of a unit cell doubling within the image plane [7].

The R and T phases can be further characterised by analysing their local strain. Figure 5.3 shows the strain analysis of the respective phases in their native state using geometrical phase analysis (GPA), based on the HRTEM image shown
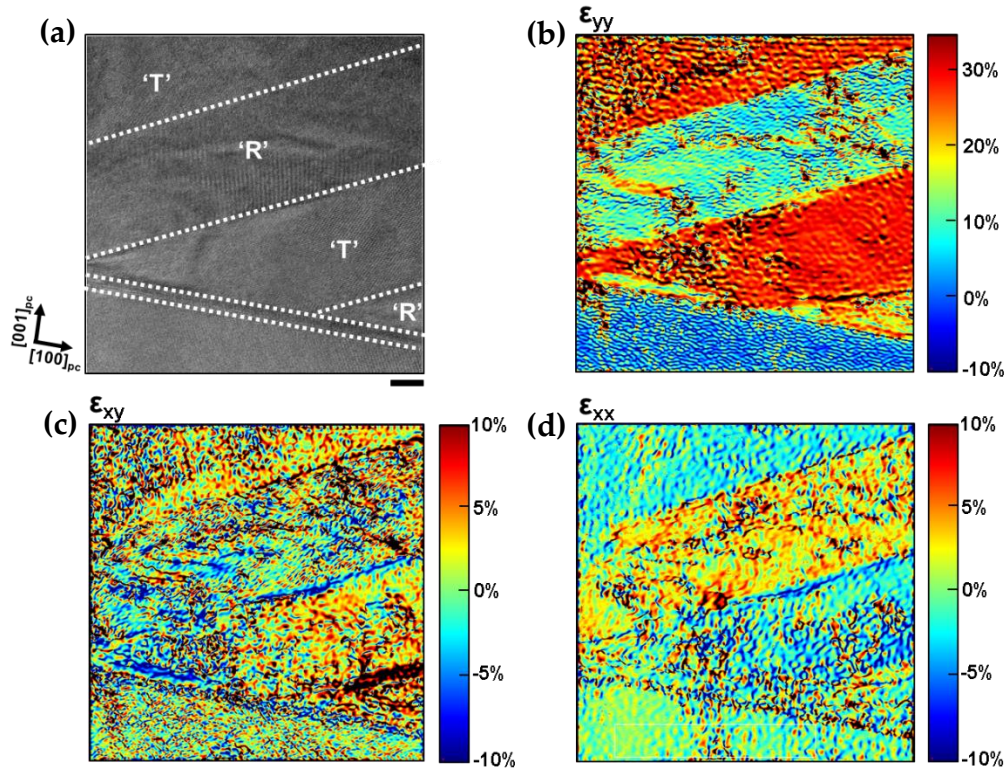
Figure 5.3: Local strain by GPA analysis. HRTEM image of several R and T polymorphs (a). ε_{yy} strain (along $[001]_{pc}$) (b), ε_{xy} shear strain (c) and ε_{xx} strain (along $[100]_{pc}$) (d). Scale bar in (a) represents 10 nm.

in Figure 5.3a. The strain was mapped out with respect to the LAO substrate, for ε_{yy}: along the thin film $[001]_{pc}$ direction (shown in Figure 5.3b), ε_{xy}: the shear strain (shown in Figure 5.3c) and ε_{xx}: along the $[100]_{pc}$ direction (shown in Figure 5.3d). It can be confirmed that the T phase has an enormous ε_{yy} strain (22 %) compared to the R phase (8 %). Whereas, both T and R phases have low ε_{xx} strain values, (-2 % and 0.3 % respectively). The shear strain demonstrates moderate values (±10 %) at the T/R and R/T boundaries respectively.

Typically for thin films grown epitaxially, the interface between the thin film and substrate, or in this case the two interfaces between BFO-LSMO-LAO,
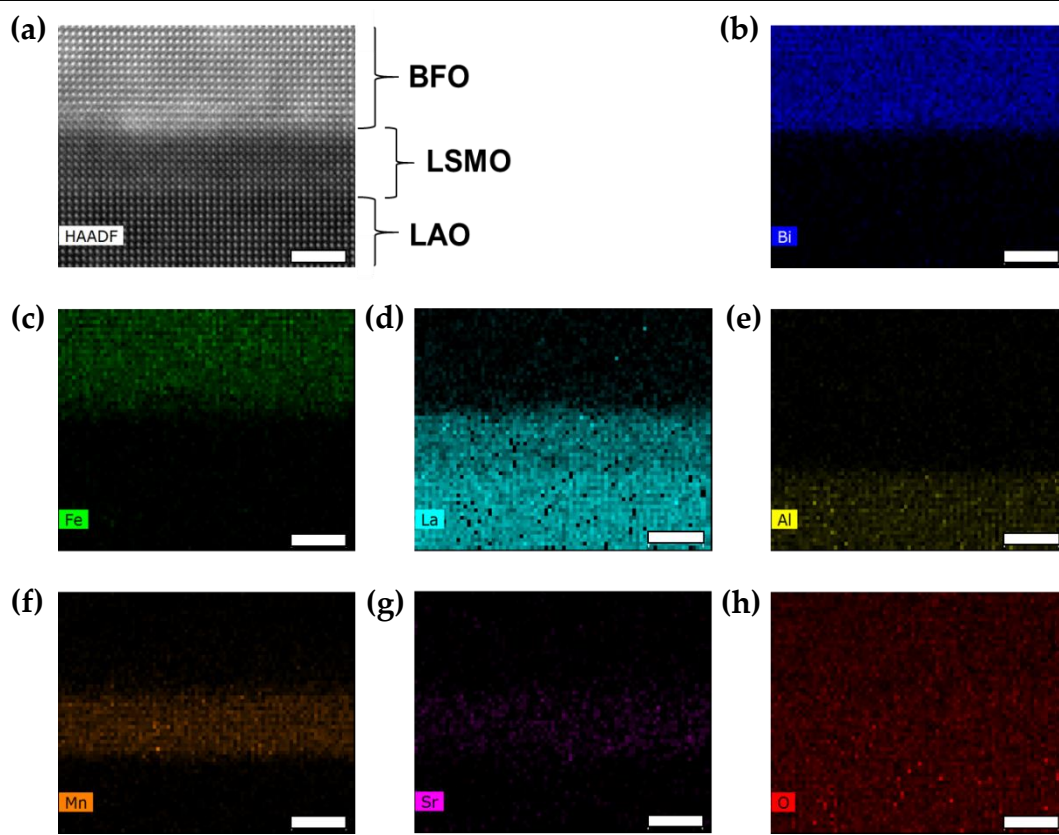
Figure 5.4: STEM-HAADF image of a representative BFO-LSMO-LAO interfacial area. Corresponding EDX maps for: Bi-Lα (b), Fe-Kα (c), La-Kα (d), Al-K (e), Mn-Kα (f), Sr-Kα (g) and O-Kα (h). Scale bars represent 3 nm.

can be prone to dislocations or chemical diffusion [16]. To investigate the nature of the BFO-LSMO-LAO interfaces, high resolution STEM images were acquired (example shown in Figure 5.4a) along with corresponding EDX maps for: Bi-Lα (b), Fe-Kα (c), La-Kα (d), Al-K (e), Mn-Kα (f), Sr-Kα (g) and O-Kα (h). In Figure 5.4 (and all similar data acquired on the BFO native state) no dislocations or chemical diffusion was observed either at the BFO-LSMO-LAO interfaces or at the R/T boundaries.

5.1.1 Effect of thin film thickness

Due to the presence of a morphotropic phase boundary (and hence plasticity) of mixed-phase BFO it should be possible to tweak the R:T phase ratio in several ways. An obvious way exists at the growth stage: varying the thin film thickness [17, 18]. Figure 5.5 demonstrates the R: T phase ratio transformation between a 35 nm thick and 80 nm thick BFO thin film. It is apparent that the density of the highly-strained T phase has decreased in the 80 nm thick thin film (Figure 5.5b and d) compared to the 35 nm thick thin film (Figures 5.5a and c). By increasing the thin film thickness, the thin film has become more relaxed (i.e. less constrained by the epitaxial strain imposed by the LAO substrate) and in doing so the ratio of the phases has been altered so that the more relaxed R phase is in a more stable position, with a higher density of polymorphs. It should be noted that of course the TEM sample preparation can further affect this ratio by relaxing the thin film.
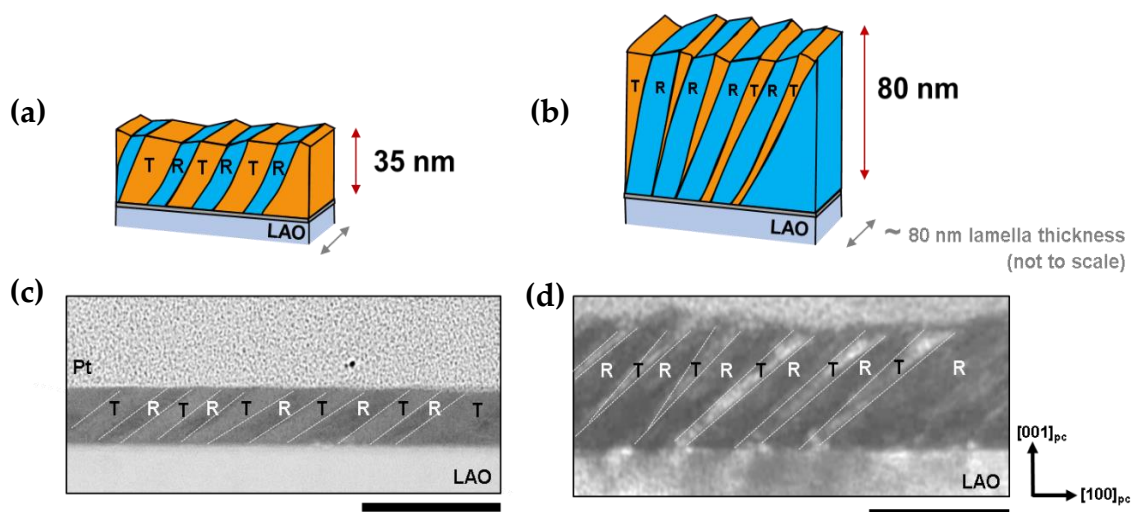
Figure 5.5: Schematic of the T to R phase ratio for a 35 nm thick (a) and 80 nm thick (b) thin film. STEM-DF image of the 35 nm thick (c) and 80 nm thick (d) thin film. Scale bar represents 100 nm.

It was found that an ideal lamella thickness was 80 nm; at this thickness, the polymorph ratio of the lamellae was comparable to that observed by AFM, so that the results obtained by TEM could be representative of the bulk sample.

5.1.2 Proposed external-stimuli applications

The other way to tune and switch the phases in mixed-phase BFO, is through the application of external stimuli. Figure 5.6 presents a schematic overview of the external stimuli applied to mixed-phase BFO in the following sections (5.2 and 5.3): heat-cycling and a combination of electric field and stress. The questions to be answered are: (i) is the phase switching fully reversible? (ii) if so, how does the new mixed-phase state compare to the native mixed-phase state?
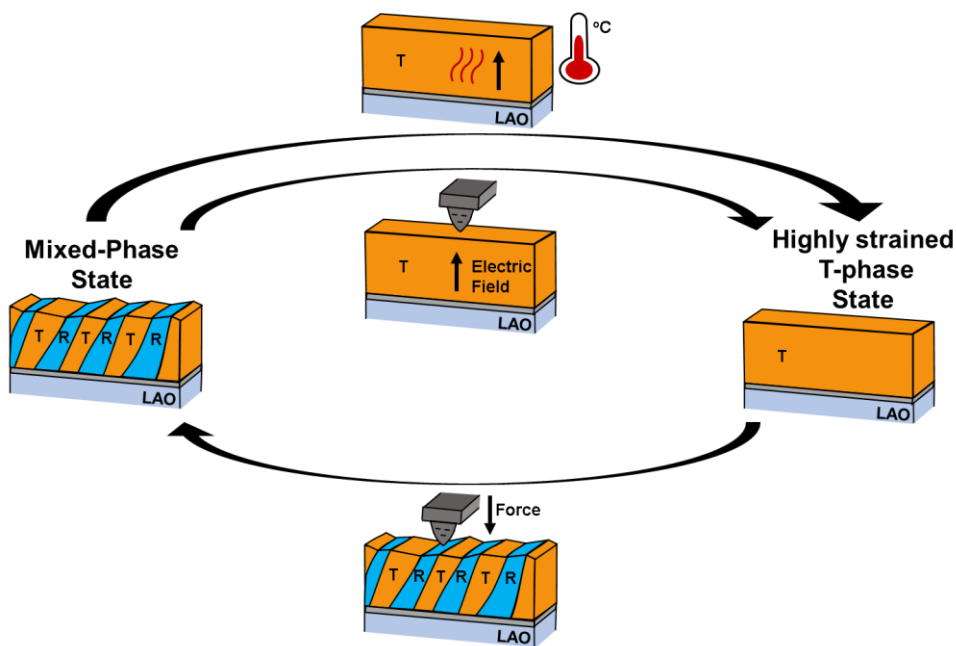
Figure 5.6: Schematic overview of the external stimuli applications investigated in the sections to follow: heat cycling and a combination of electric field and localised stress.

# 5.2 Application of heat

The expected thermal phase transitions, from literature, involve a first-order transition from the mixed-phase state to a polar T state at ~400 °C [7, 14, 19], and a melting point of BFO (observed in bulk BFO) at around 900 °C [20]. The phase transition of interest in this investigation is that of the mixed-phase state to a polar T state in an 80 nm thick mixed-phase BFO thin film. Figure 5.7a displays a high-resolution STEM image of an area of native BFO at room temperature (23 °C). In the middle of the image there is a T polymorph (dark contrast) surrounded by two larger R polymorphs.

The in-situ heating experiment began at room temperature, capturing an area with two needle shaped T polymorphs (bottom of Figure 5.7b). The images above the 23 °C panel display the dimensional change in the two T polymorphs as the thin film was heated up to 460 °C and back to room temperature, where a clear lateral growth of the T polymorphs can be observed. The temperature was changed in 5 minute intervals allowing the thin film time to stabilise before raising/lowering the temperature further. Figure 5.7c summarises the heat-cycle results in a plot of T polymorph width (measured half-way down the T polymorph on the right hand-side of the image) and percentage area occupied by the T polymorphs within the image, as a function of temperature. The results demonstrate that as the thin film was heated, the T polymorphs began to grow laterally across the thin film width at ~250 °C. The T polymorphs continued to grow until 460 °C when the percentage area occupied by the T polymorphs had increased by ~8 %. At 460 °C the sample began to degrade due to bismuth seeping out (observed by the presence of a large bubble at the top of the thin film image
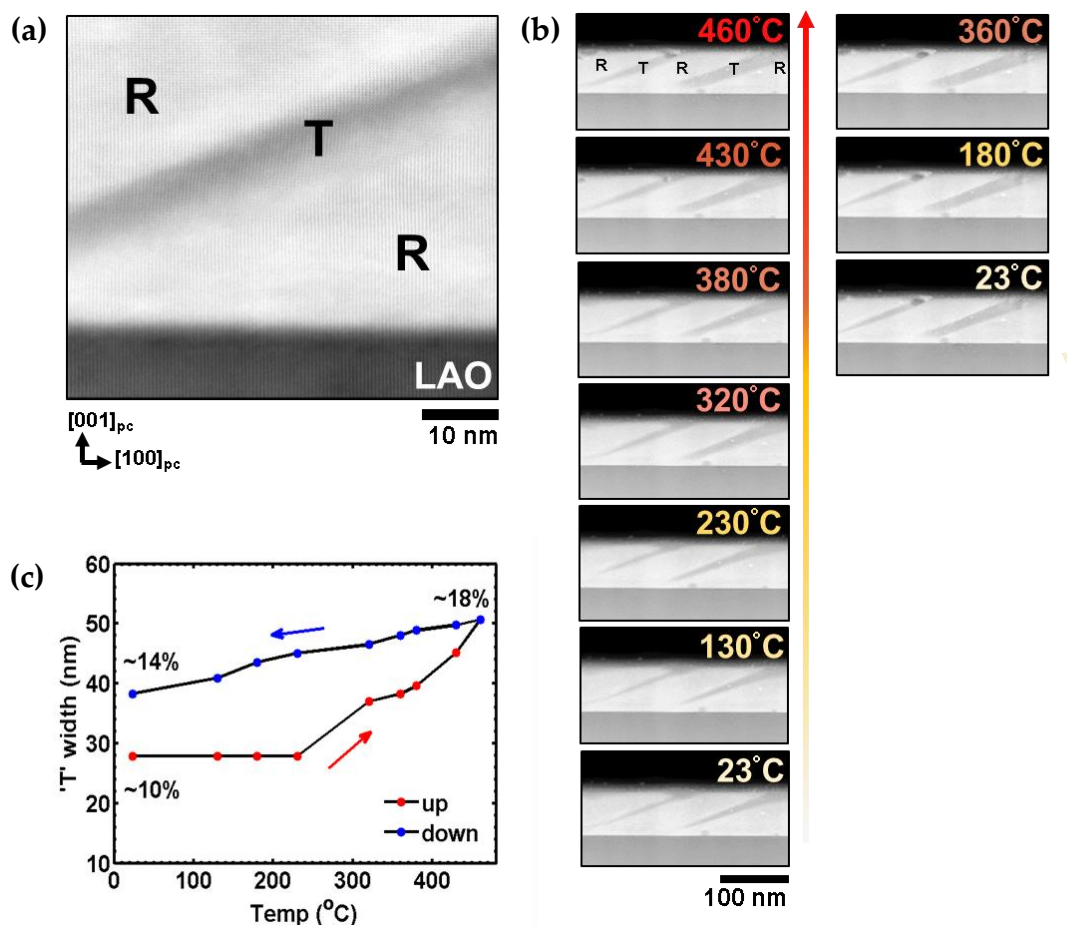
Figure 5.7: STEM-HAADF image of an area before the in-situ heat cycling experiment began (a). Images acquired throughout the heat-cycle at temperatures: 23 °C, 130 °C, 230 °C, 320 °C, 380 °C, 430 °C, 460 °C, 360 °C, 180 °C and 23 °C (b). Evolution of T polymorph width (measured half-way down the right hand-side T polymorph in the images of (b)) and percentage area occupied by the T polymorphs in the area of thin film imaged, as a function of temperature (c).

labelled 460 °C) and therefore the temperature was thereafter decreased to 360 °C, 180 °C and back to 23 °C. On cooling back to room temperature, the width of the T polymorphs decreased (as shown in Figure 5.7c) however, a full transformation back to the original polymorph width was not achieved. The lack of full reversibility under the application of heating is believed to be influenced by the

initial phase ratio of the thin film: due to the relatively large thin film thickness (80 nm) the R phase was the most stable, dominating ~90 % of the thin film. Therefore, the thermal energy gained in the heat-cycle was not enough to transform the dominant R phase into a dominant T phase state. Instead, a small expansion in the width of the T polymorphs was observed but the thin film stayed primarily in an R phase state. In recent reports, a fully reversible thermal transformation was observed in BFO thin film thicknesses of 35 nm [19] and 40 nm [7] where the phase ratio of R:T was closer to 50:50 in the native state. This confirms the proposed conclusion that the initial phase ratio is crucial for a fully reversible thermal phase transformation between a mixed-phase state and polar T state. It also important to notice the limiting factor of temperature; it could be that a higher temperature would have promoted a full transformation but not without degrading the sample, thus compromising the results. For the experiments which follow, a thinner thin film (ranging from 35-50 nm thickness) is investigated using more controllable applications of external stimuli: electric field and stress.

5.3 Application of E-field and stress

To experimentally demonstrate how electric fields and localised stress can be used to alter the mixed-phase native state in a reversible and complementary manner a 50 nm thick BFO thin film was studied. To illustrate the change in phase behaviour, Figure 5.8 shows the AFM topography of a 2.5 μm x 2 μm region (white dashed box) in the native state (Figure 5.8a), after the application of local

bias (Figure 5.8b) and localised stress (Figure 5.8c). In the native state, it can be seen that the initial microstructure comprises of an approximately equal phase ratio of R:T. The dark contrast needle-like structures correspond to the R phase within a T phase matrix. Application of -4 V dc bias through a conducting AFM probe (Figure 5.8b) triggers switching of the ferroelectric polymorph structure into a locally T phase dominated region. Subsequent application of a force of 750 nN (corresponding to an estimated 1.8 GPa of stress) to the same area, causes the affected region to again become inundated with needle-like polymorphs comprising of the R phase. PFM response (amplitude x cos(phase)) images confirm the ferroelectric nature of the native (Figure 5.8d), electrically-written (Figure 5.8e) and mechanically-written (Figure 5.8f) regions. Crucially, the
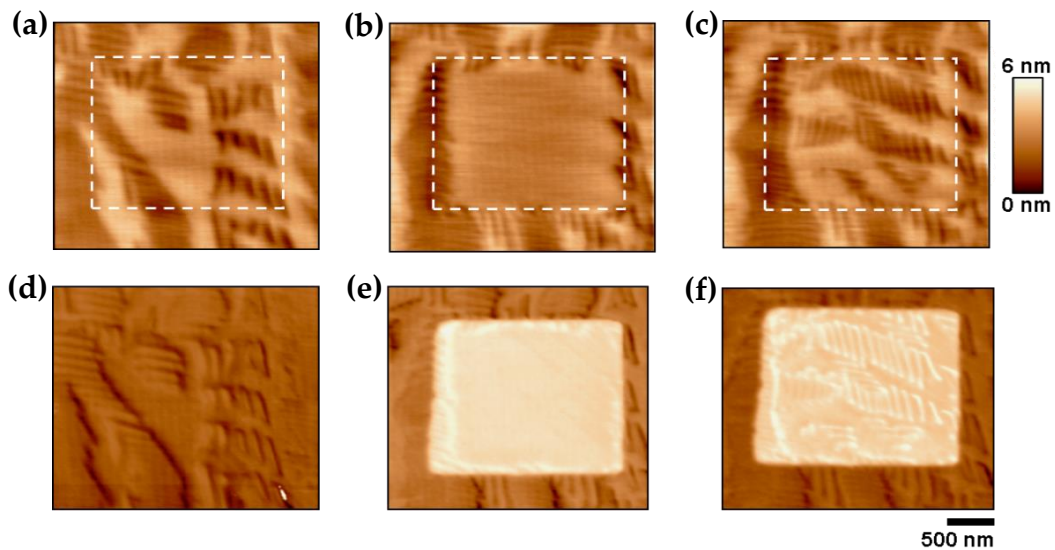

Figure 5.8: Topography of the native mixed-phase state (a). Topography after -4 V dc from the AFM tip was applied to a 2 μm x 2 μm region (white dashed box) (b) and subsequent tip-application of a 750 nN loading force to the same region (c). PFM response (amplitude x cos(phase)) of the native (a), electrically-written (b) and stress-written (c) region.

observed transformation behaviour is seen to be reversible with further applications of electric field and stress. It would seem, therefore, that the next challenge to overcome in this investigation involves the controllable competition between T and R dominated phases by appropriate choice of electric field or stress application, to fully exploit the transformation plasticity. Two requirements must be met for achieving control of the resulting phase competition under electric field and stress: firstly, a predictive theoretical analysis of the alterations in mixed phase microstructure under applied stimuli needs to be developed. Secondly, these predictions should be directly compared to experiments to assess their validity.

5.3.1 Predicting the phase competition

Density functional calculations and phase field simulations have previously been used to suggest that a critical misfit strain separates the T and R phases in epitaxially strained BFO thin films [15, 21, 22]. The dependence of heterophase polydomains in epitaxial BFO thin films on misfit strains, determined by the substrates, has been investigated in the theoretical framework of elastic domains [23]. Along similar lines, density functional calculations have been used to evaluate competition between two phases with increasing misfit strains [24]. These calculations can predict the equilibrium mixed phase states that develop but the extent to which external field variables and their combinations can alter the phase distribution has not yet been analysed. To this end, the first-principles-based effective Hamiltonian technique developed by Prosandeev *et al.* [20] was used to consider the energy of separate cells of the T phase and R phase under the

influence of different variables. The simulations calculate the energy of each phase at 10 K as a function of misfit strain (the simulations worked best at low temperatures but are considered to be representative of room temperature BFO since no thermal phase transition occurs within this temperature range [20]) demonstrating a competition between the two phases in a BFO thin film under external stimuli, shown in Figure 5.9a.
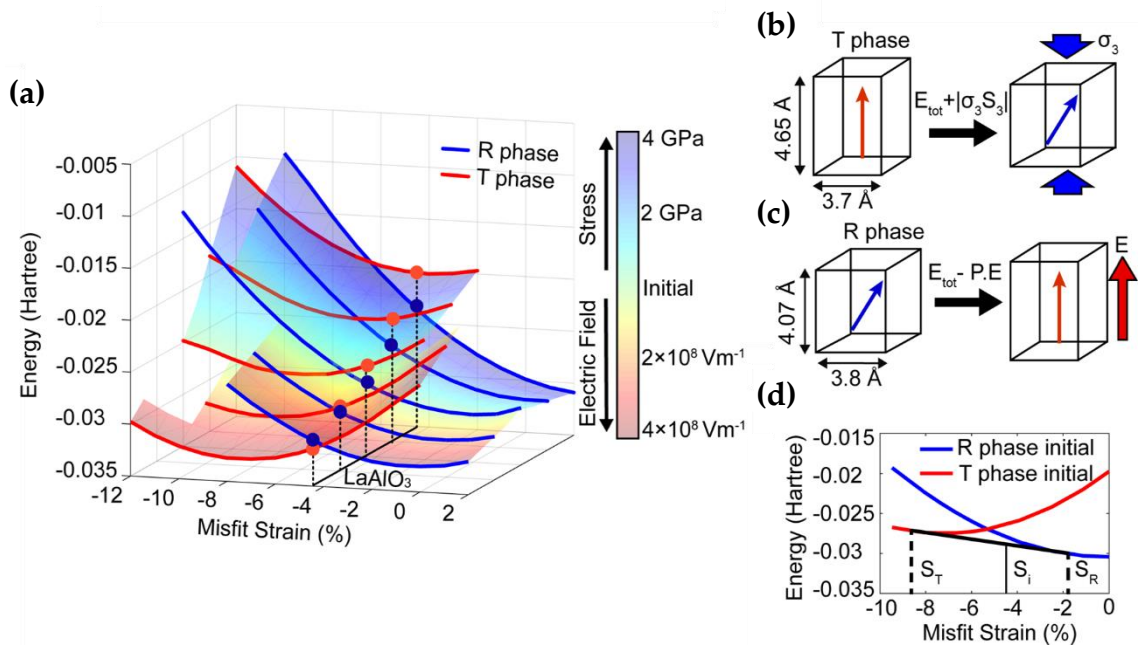
Figure 5.9: Effective Hamiltonian energy curves as a function of misfit strain under varying electric field and uniaxial stress applied along the [001]pc axis (a). The black line corresponds to a constant misfit strain of -4.4 %, equivalent to BFO on LAO, with the red and blue dots highlighting the energy of the T phase and R phase, respectively. The overlaid colour on the energy curves corresponds to the stresses or fields under which the energy curves were calculated. Schematic illustration of the unit cell transformation from T phase to R phase under stress (b) and R phase to T phase under field (c). Example of a common tangent which can be drawn between the R phase and T phase energy curves, along which it is energetically favourable for the two phase to co-exist (d). Figure courtesy of D. Edwards.

At the highest misfit strains, the calculations confirm that the highly-strained T phase has lower energy (as expected) and is thus stabilised, while at intermediate strains the energy of the two phases becomes comparable leading to a coexistence of the two phases. The energy curves were then calculated under varying combinations of applied stress and electric field to estimate the phase competition under the different external stimuli. For the studied film grown on (001)-LAO, the energy of the T and R phases are in relative proximity, with the R phase slightly lower when no external fields are applied. Under applied stimuli the calculations are seen to agree with the experimental results observed in Figure 5.8, reproducing the observed stabilisation of T phase by electrical writing and R phase by mechanical writing.

To understand how the behaviour in Figure 5.9a can be appreciated qualitatively, the terms that formulate the Hamiltonian were considered in the situation of applied stress (Figure 5.9b) and electric field (Figure 5.9c). The application of uniaxial stress (σ_3) along the [001]$_{pc}$ direction of the film results in an *increase* of the total energy by a term of the form $|\sigma_3 S_3|$, where S_3 corresponds to the strain component along the [001]$_{pc}$ direction of the simulated cell. In this case, the R phase becomes the energetically favoured state due to its smaller axial ratio in comparison to the T phase. In an analogous manner, under an applied electric field E, the energy (E_{tot}) is reduced by a term of the form $P.E$, where P refers to the polarisation. As T phase possesses higher spontaneous polarisation, the increase in P from the R phase to the T phase results in a net reduction in total energy and therefore stabilises T phase under applied electric field.

An appealing feature of these calculated energy curves is that they can also enable prediction of the relative phase occupancy under varied values of electric field and stress. For this prediction, guidance was given by the study of solid solutions where common tangents to free energy curves are employed to identify regions of chemical composition where phases coexist to lower the overall free energy [25] The mechanical lever rule can then be applied to estimate the relative amounts of each phase for a given composition as done in Chen at al. [24]. Similar approaches have also been used to calculate the fraction of phases within the morphotropic phase boundary region of PZT [26, 27]. For the present study, the relative proportion of R and T phase can be calculated by drawing a common tangent for each pair of energy curves (Figure 5.9d) and then applying the lever rule, in the form

$$S_i = x_T S_T + x_R S_R, \tag{5.1}$$

where S_i is a strain value chosen between limiting values of S_t and S_r (the strains where the tangent intersects the energy curves) and x_T and x_R are the fractional phase populations (summing to unity). The calculations were expanded to a broader range of applied stresses, electric fields and misfit strains where each set of energy curves allows estimation of the mixed phase population under the chosen set of variables. The results are depicted graphically in the form of a 3D diagram with three axes defined by misfit strain, uniaxial stress and electric field respectively, as shown in Figure 5.10a. Note that the stress and electric field are external variables that can be manipulated freely while the misfit strain remains fixed by choice of the substrate. Every point in this diagram represents the relative proportion of the R phase for the selected variables. The limiting cases seen at the

(a)

(b)
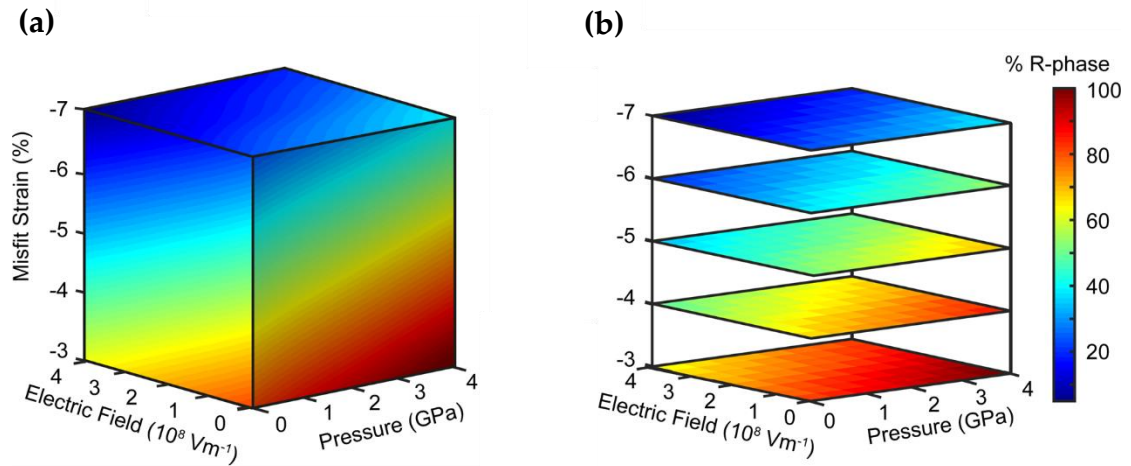
Figure 5.10: 3D diagram predicting the continuous variation in the proportion of R phase with misfit strain, electric field and uniaxial stress (a). Discrete slices at selected values of constant misfit strain (b). Figure courtesy of D. Edwards.

two extremes of the diagram which predict mostly R phase at low values of misfit strain and high stress while mostly T phase is expected to dominate at large misfit strains and large electric fields. Discrete 2D sections of the diagram taken perpendicular to the vertical axis, shown in Figure 5.10b, map the relative phase distribution for constant values of misfit strain and represent the behaviour predicted for the mixed phase microstructures when grown on different substrates. For the specific case of a 50 nm thick BFO thin film grown on LAO, a mixed phase microstructure with 52 % R and 48 % T phases is expected.

This model makes clear predictions that the mixed-phase population, and therefore its associated functionality; can be manipulated by applying external fields: the proportion of R phase can be subsequently reduced to a predicted 33 % through application of an electric field of 4×10^8 Vm^{-1}, or conversely increased to 70 % under 4 GPa of uniaxial stress. The diagram thus clearly illustrates the

flexible nature of the strain enabled morphotropic-like phase boundary in BFO where each variable can be used as an effective handle to control population of the phases; application of uniaxial stress is seen to cause a monotonic increase in the proportion of R phase, while conversely, increasing electric field causes a monotonic increase in the proportion of T phase.

5.3.2 Direct comparison between experimental and theoretical predictions of phase competition

The theoretical predictions were put to the test by making a direct comparison to experimentally observed phase population ratios for a 50 nm thick thin film, under a set of uniaxial stress and electric field values. Figure 5.11a shows a large representative area of the native thin film (18 μm x 18 μm) chosen and further subdivided into a grid (3 μm x 3 μm squares) such that the initial phase proportion within each square sub-region was similar. Starting from one end, the electric field and uniaxial stress were increased in discrete steps from one sub-region to the next along the two axes of the grid and the resulting topography of each square sub-region was recorded (as shown in Figure 5.11b). The topography for each sub-region was numerically analysed and the resulting R phase content was estimated. Under initial examination, high levels of new R phase polymorphs as well as enlargement of pre-existing polymorphs are observed under large uniaxial stress (and zero applied electric field), as evident in the enlarged topographic region shown in Figure 5.11c. For intermediate values of stress and electric fields, monotonic competition between the two phases is experimentally

observed and is consistent with the theoretical predictions. However, under further increased electric field, the effect of applied stress appears to diminish until the resulting topography becomes mostly T phase dominated (Figure 5.11d).
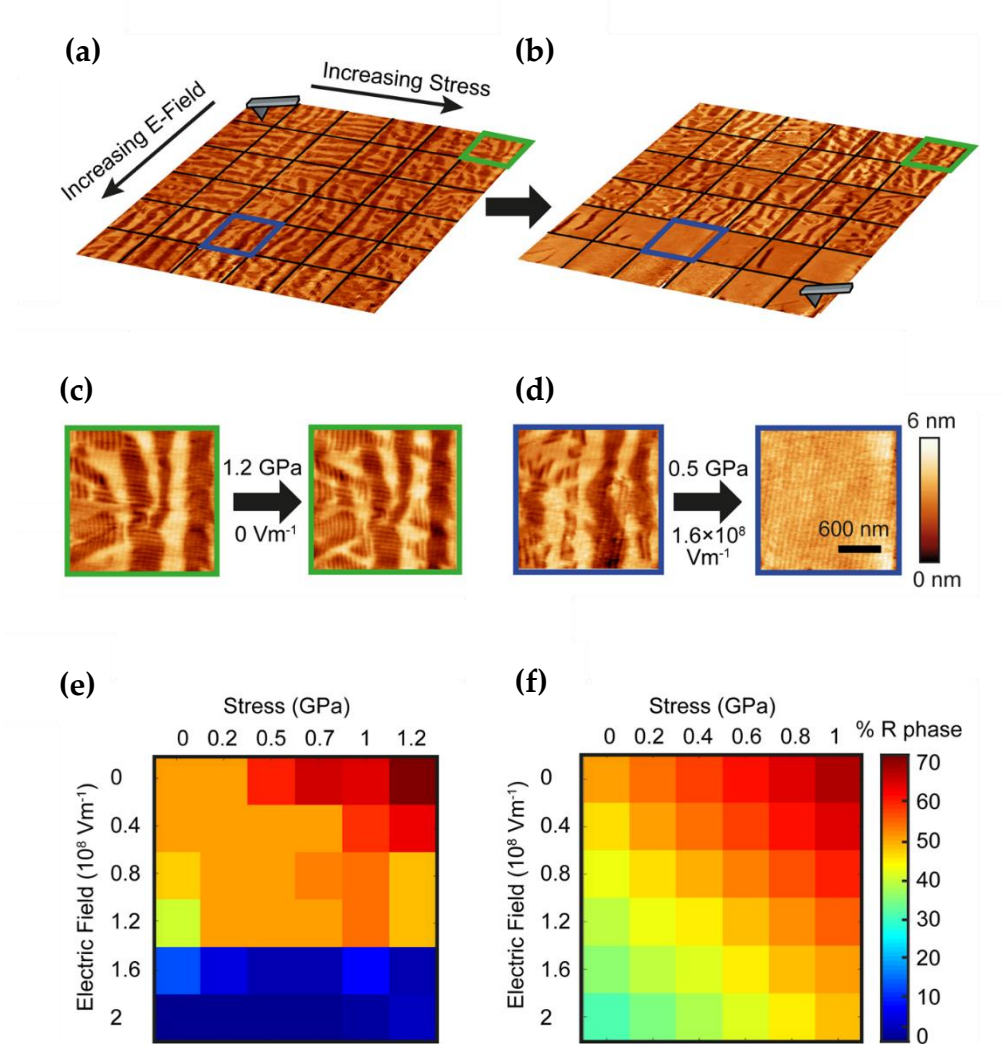
Figure 5.11: Topography BFO before (a) and after (b) carrying out the dual control experiment where varying levels of stress and electric field were applied simultaneously in a (3 μm x 3 μm) step-wise fashion. Highlighted panels are enlarged in (c) and (d) with the experimental values of stress and electric field labelled. Numerical estimations of the R phase population resulting in an experimental map with stress and electric field applied values along the two axes (e), and corresponding theoretical predictions (f). Figure courtesy of D. Edwards.

The R phase proportional results are plotted on a 2D grid plot in Figure 5.11e where the stress is stepwise varied between 0 and 1.2 GPa and the electric field is increased simultaneously in steps between 0 to 2x10^8 Vm^{-1}. This plot is then compared to the theoretical estimates calculated from effective Hamiltonian calculations for a similar range of variables, shown in Figure 5.11f. A good overall match between the experiments and energy based analysis is observed in the two plots compared directly in Figures 5.11e and f. The comparison is especially effective in evaluating monotonic increase in the proportion of R phase in the intermediate regions of electric field and stress. The good correlation between theory and experiment is promising for the general validity of this approach in evaluating dual control of such mixed phase polymorphs.

It should be noted that the experimental estimates of local applied stress are made by assuming a certain tip radius and can potentially deviate from the actual values due to tip contact area variations. Similarly, while surface area based estimations of R/T phase content may differ slightly from volume estimations [5], it is expected that such discrepancies are small and scale consistently with each variable. Inevitably, deviations may also occur due to factors governed by kinetics such as polymorph wall propagation and potential barriers to polymorph nucleation. This may go some length to explain why applied stress appears to be ineffective in stabilizing the R phase when a high electric field is simultaneously applied; and also, the strongly non-linear increase in T phase observed with electric field. On the other hand, achieving a fully R phase thin film with increased stress can be rationalised as being prohibited by the need for the film to dislocate from the substrate and relax to a bulk rhombohedral state. One of the observations worth mentioning is that, as expected from a pure thermodynamics

perspective, the removal of local stresses from the film does not revert the film back to its previous T state (no change observed over several days). Thus, the stress induced mixed phase with enhanced R phase exists in a state of pseudo-equilibrium (it is metastable) and is expected to relax back given sufficient excitation. Some of these deviations can be accounted for through both scaling and more precise estimates of field values, as well as constraining the analysis to intermediate ranges of the applied variables. Nonetheless, the good overall agreement between the experimental observations and theoretical calculations demonstrates obvious potential for the approach of controlling phase competition under externally applied electric field and stress.

5.3.3 Stress mediated control of the conductive states

Demonstration of wall conductivity in thin films of BFO (grown on $SrTiO_3$ substrates) was first realised by Seidel et al. in 2009 [4] and since then researchers have been keen to find and control conducting interfaces in other systems as a means of incorporating such structures in functional devices [28-34]. Conducting atomic force microscopy (c-AFM) measurements following both electrical-writing and local stress application were carried out through the application of a dc bias below the coercive threshold of the BFO thin film studied here, the results are presented in Figure 5.12. AFM topography of the native mixed-phase state can be seen in Figure 5.12a, likewise the topography of the electrically-written and stress-written state in Figures 5.12b and c, respectively. Comparison of the conductive response following the application of electric field (Figure 5.12d) and local stress (Figure 5.12e) shows evidence of negligible current registered within the

electrically driven T-phase (T'), while substantially increased current is observed in the regions of newly formed R-phase polymorphs nucleated following localised stress application. Importantly, the magnitude of this increased current extends beyond the conventional values that would be associated with the accumulation of leakage current over such a localised region. Furthermore, the increased current is unique to the stress-written R-phase (R') since negligible currents were observed for the native as-grown film. This therefore suggests that the R-phase in the as-grown film is distinct from that in stress-written regions. Moreover, it is likely that the enhanced conductivity is mediated between the R' and T' polymorphs since enhanced current has previously been observed in similar interfacial systems [35, 36]. The discovery of enhanced conductivity in the stress-written regions raises the question as to how the crystal structure compares between the native and the stress-written mixed-phase state, and whether the localised strain distribution has been altered.
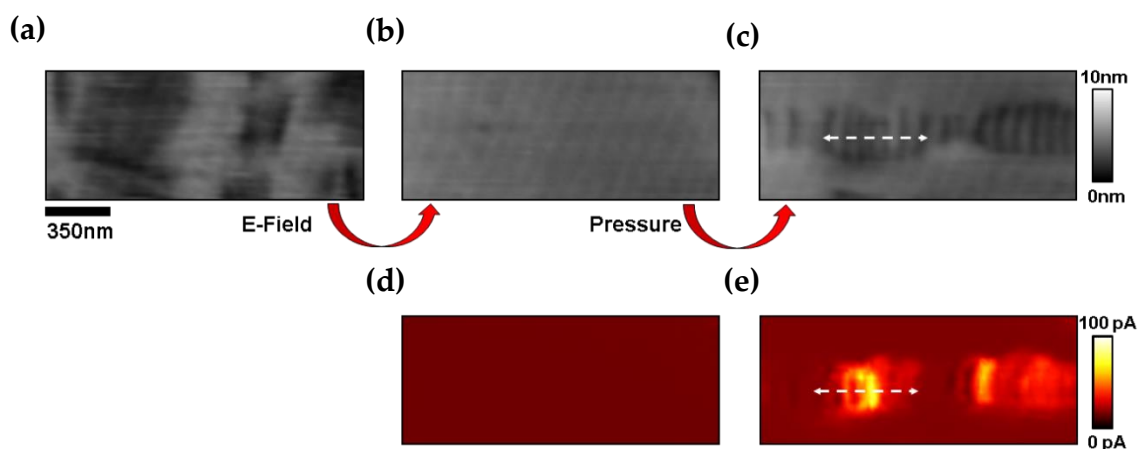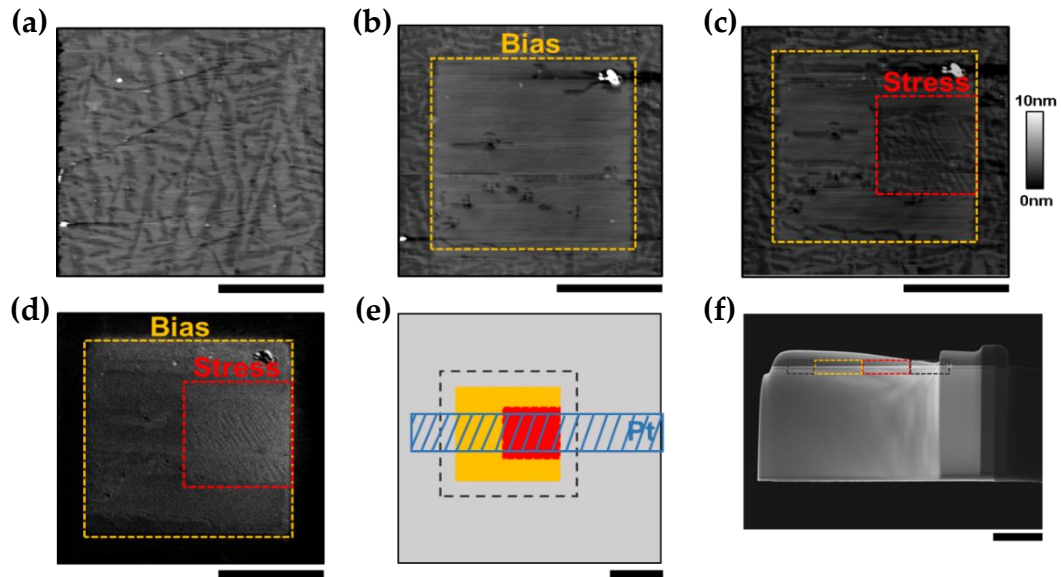

Figure 5.12: AFM topography of a native mixed-phase BFO state (a), after application of -4 V DC electric field (b) and after 750 nN of tip-induced force (c) Corresponding c-AFM measurements of the electrically-written (d) and stress-written (e) states. Figure courtesy of N. Browne.

In other words, where does the stress-written enhanced conductivity originate from? To answer this, a detailed TEM investigation was considered crucial.

## 5.4 Revealing the stress-written mixed-phase

For a detail investigation of the crystal structure of the stress-written mixed-phase state, cross-sectional lamellae were prepared from pre-written AFM regions in a 35 nm thick BFO thin film. An example is shown in Figure 5.13 where a 6 μm x 6 μm region was poled from the native mixed-phase state (Figure 5.13a) to a 'T' state (Figure 5.13b) by applying -5 V DC electrical bias, followed by the application of 800 nN of tip-induced force within a 3 μm x 3 μm region (Figure 5.13c) via an AFM tip, for the creation of stress-written R' polymorphs. These electrically-written and stress- written regions were then located using the SEM (Figure 5.13d), followed by the careful FIB preparation of a lamella which enclosed all three regions (native mixed-phase, electrically-written T state and stress-written mixed-phase). A schematic of the lamella Pt-strip position prior to milling is shown in Figure 5.13e along with an SEM image of the prepared lamella indicating the three regions of interest in Figure 5.13f.

A typical native region of a lamellae described in Fig. 5.13 displaying R and T polymorphs is shown in the STEM image of Figure 5.14a, where the bright contrast corresponds to the T phase (while dark contrast represents R). Two stress-written regions are displayed in Figures 5.14b and c, where R and T polymorphs are also present. The most obvious difference when comparing the

Figure 5.13: AFM topography of the native mixed-phase state (a), after application of -5 V dc electric field (b) and after 800nN of tip-induced force (c) SEM image of the electrically-written and stress-written regions identified for lamella preparation (d). Schematic of the lamellae Pt-strip position, the grey, yellow and red boxes refer to the AFM scanned, electrically-written and stress-written regions, respectively (e). SEM image of the prepared lamella with the three regions of interest indicated (f). Scale bars represent 3 μm.

three regions is the mixed-orientation of R′ polymorphs in the stress-written regions compared to the one-directional R polymorphs in the native region (trend verified across various lamellae). Furthermore, the density of the R′ nucleated polymorphs in the stress-written regions (Figure 5.14b and c) differ from each other and from that typical of the native mixed-phase state (Figure 5.14a). The stress-written region in Figure 5.14b is heavily dominated by R′ polymorphs compared to the more evenly distributed phases present in the stress-written region of Figure 5.14c. Given the enhanced conductivity that was observed in stress-written R′/T′ interfaces in the c-AFM data (Figure 5.12), it was initially
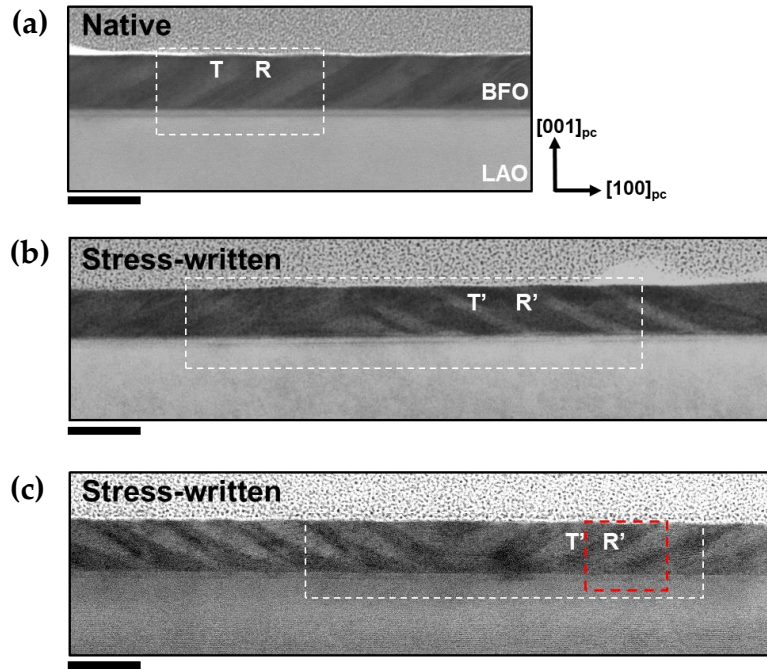
Figure 5.14: STEM-DF image of a typical native region (a), and observed stress-written regions (b) and (c) showing density and orientational differences between the native R polymorphs and the stress-written R' polymorphs. Red and white dashed boxes refer to areas investigated in Figures 5.15 - 5.17 to follow. Scale bars represent 50 nm.

thought that the stress-written interfaces could contain dislocations whereby oxygen vacancies (a common source of conduction [37, 38]) are prone to exist. A HRSTEM image of the stress-written area marked by a red dashed box in Figure 5.14c is displayed in Figure 5.15, where no evidence of interfacial dislocations or other structural defects can be observed.

For a detail structural analysis, the unit cell structure of the native (R and T) and stress-written (R' and T') phases was studied using nano-beam electron diffraction (NBED), a diffraction based technique that can be further used to measure strain. NBED (as described in Chapter 2) offers the advantage of being
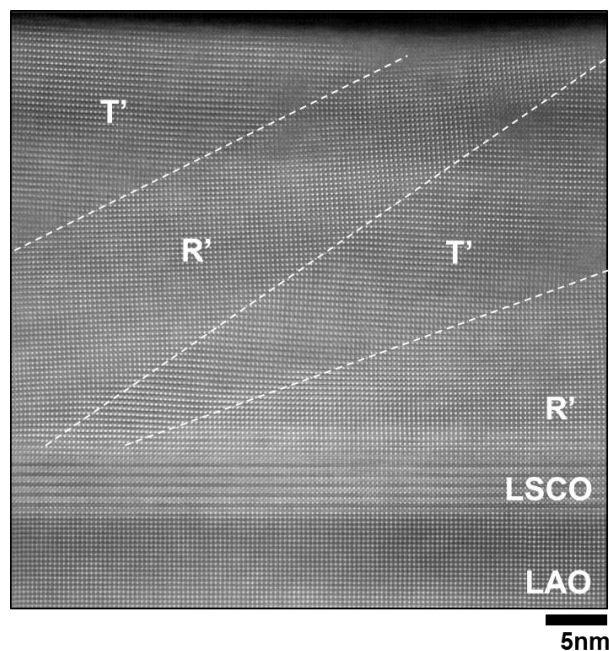
Figure 5.15: HRSTEM image of the stress-written R′ and T′ polymorphs located within the red dashed box of Figure 5.14c. The R′/T′ interfaces are marked by dashed white lines.

able to accurately map lattice spacing variation over a large area compared to similar techniques such as GPA, which maps lattice spacing in a very localised area of the specimen based on a high-resolution image. NBED patterns were acquired for areas within the native and stress-written regions of Figure 5.14, highlighted by the white dashed boxes. The processed out-of-plane and in-plane NBED maps (interpolated linearly for presentation purposes only) for the corresponding native and stress-written regions are shown in Figure 5.16 and Figure 5.17, respectively, where the colour bar refers to the lattice spacing (in Å) using the LAO substrate as reference. Notable differences across the regional lattice spacing maps include sharper R′/T′ interfaces in the out-of-plane lattice spacing (less green/yellow intermediate pixels) of the stress-written region in
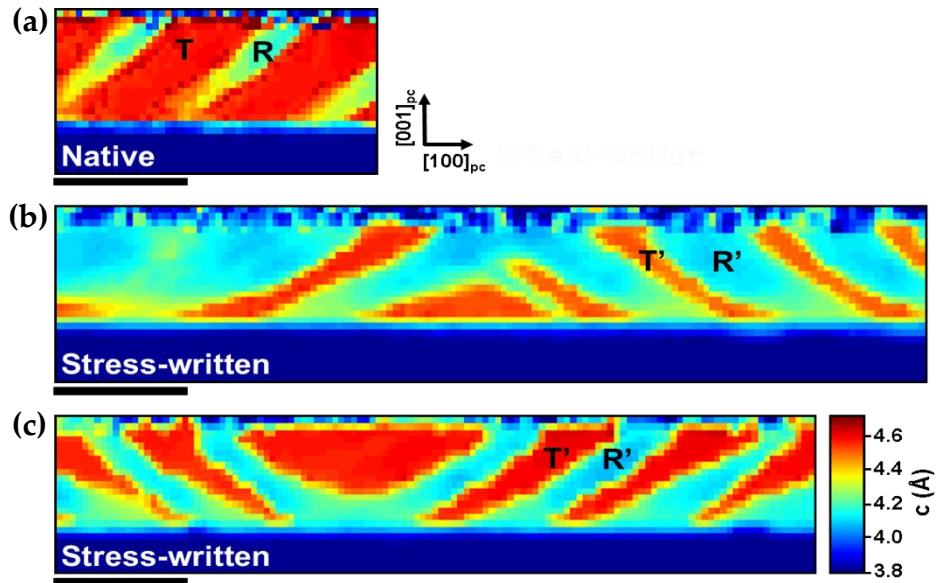
Figure 5.16: Out-of-plane lattice spacing NBED maps for the native (a) and stress-written (b) and (c) regions highlighted by white dashed boxes in Figures 5.14, using the LAO substrate as reference. Scale bars represent 50 nm.
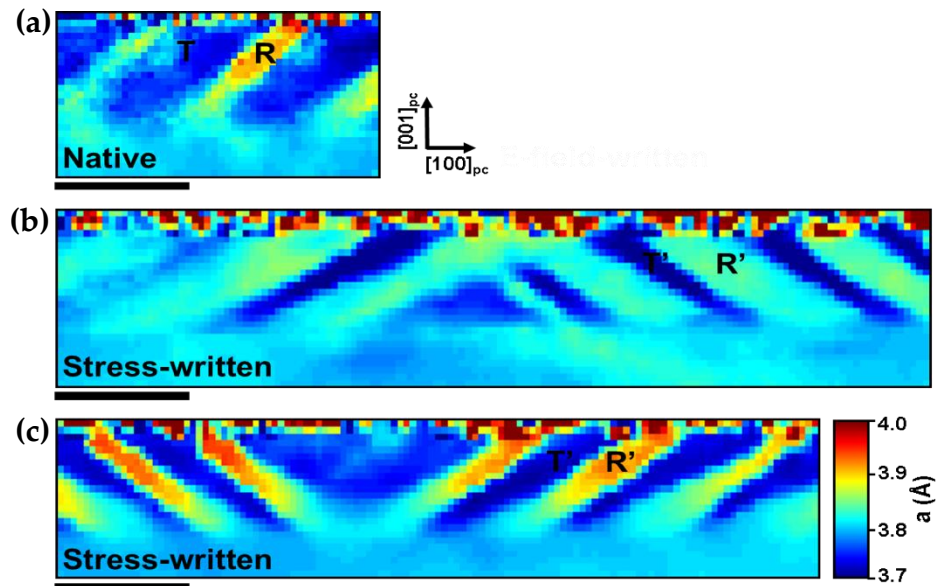
Figure 5.17: In-plane lattice spacing NBED maps for the native (a) and stress-written (b) and (c) regions highlighted by white dashed boxes in Figures 5.14, using the LAO substrate as reference. Scale bars represent 50 nm.
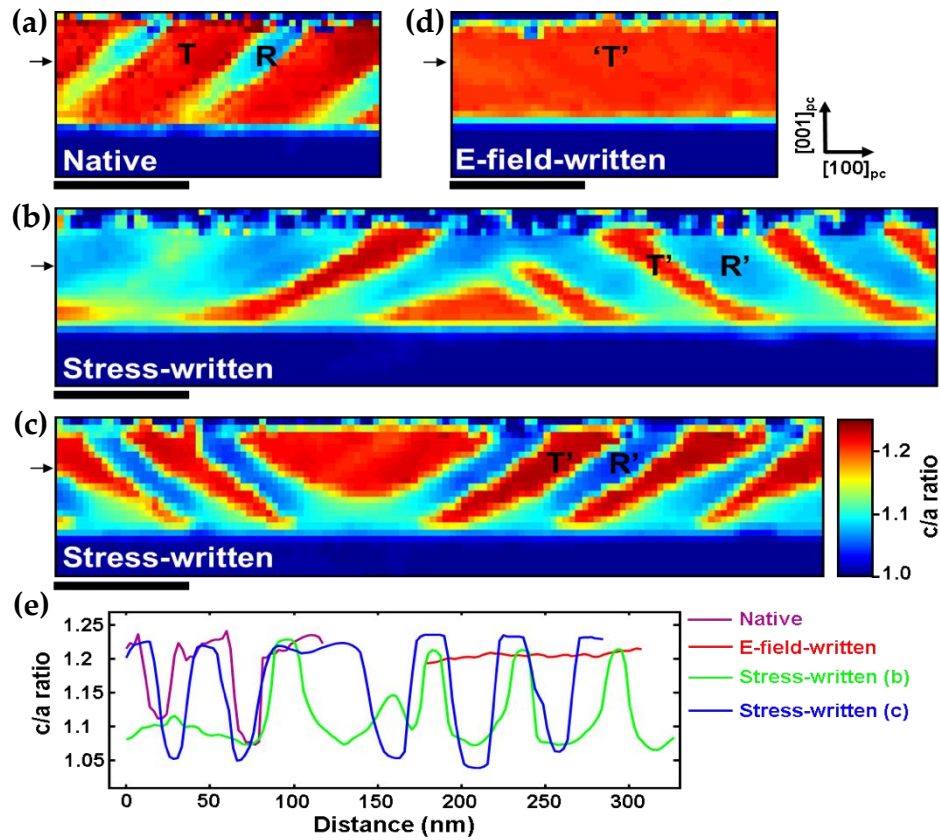
Figure 5.18: c/a ratio NBED maps for the native (a) and stress-written (b) and (c) regions highlighted by white dashed boxes in Figures 5.14, as well as an electrically-written region (d), using the LAO substrate as reference. Line profiles extracted from the horizontal line of pixels marked by black arrows (e). Scale bars represent 50 nm.

Figure 5.16c. Additionally, the in-plane spacing for this stress-written region (Figure 5.17c) displays larger values (dark orange) in the R' phase.

The out-of-plane and in-plane lattice spacing can be summarised in c/a ratio maps for the different regions, shown in Figure 5.18. In this way, the tetragonality of the respective phases can be more easily compared. Figures 5.18a, b and c show the corresponding native and stress-written regions from Figures

5.16 and 5.17, while a region which was electrically poled into the 'T' state is shown in Figure 5.18d for completeness. The line profile plot in Figure 5.18e compares the c/a ratio across the various regions, extracted from the horizontal line of pixels marked by a black arrow in the respective maps of Figure 5.18. The electrically-written region shows the expected c/a ratio of the highly-strained T state (~1.2) while the stress-written regions have a varied c/a ratios corresponding to differences in R′ and T′ phases. The stress-written region (b) appears to have more comparable values to the native region: the c/a ratio of the R′ phase is ~1.1 and the T′ phase is ~1.2 (disregarding the edge of the T′ polymorph shown around 160 nm). However, the c/a ratio of the stress-written region (c) appears to have on average a slightly larger c/a ratio for the T′ phase ~1.22 as well as a much lower c/a ratio (and hence tetragonality) for the R′ phase ~1.06.

5.4.1 Evolution of strain across stress-written boundaries

It is now clear that the newly formed R′ and T′ phases can exhibit significantly different lattice parameters, mostly in-plane, compared to their native counterparts. To investigate the influence that the modified phases have on the interfacial strain (across R′/T′), strain gradient maps were created. The in-plane (ε_{xx}) strain gradient maps for areas within the native region and latter stress-written region (showing the most significant variance in in-plane lattice spacing from the native state) are shown in Figure 5.19. STEM images of the native (Figure 5.19a) and stress-written (Figure 5.19b) regions display the areas (highlighted by white dashed boxes) where strain gradient maps (Figures 5.19c and d) were extracted from. Line profiles of the strain gradients were extracted approximately
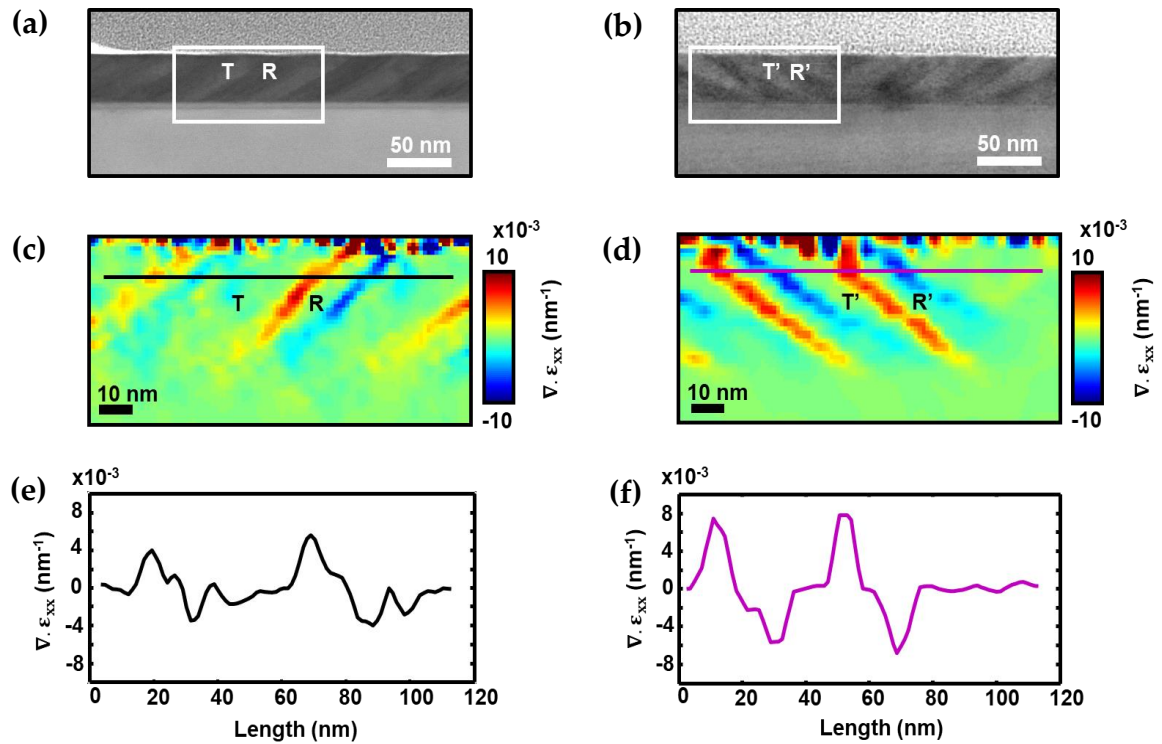
Figure 5.19: STEM images of mixed-phase BFO in a native (a) and stress-written (b) state. NBED maps of in-plane strain gradients for the native (c) and stress-written (d) regions highlighted within (a) and (b). Line profiles extracted approx. 10 nm from the BFO surface for the native (e) and stress-written (f) in-plane strain gradients.

10 nm from the BFO thin film surface (Figures 5.19e and f) to compare the evolution of strain across the respective R/T (and R'/T') phases. Maximal strain gradients can be seen at the boundaries between the two phases with average in-plane strain gradients at the stress-written (R'/T' and T'/R') boundaries ~40 % higher than those at the native (R/T and T/R) boundaries. It is clear therefore that the newly formed R' polymorphs, created via localised stress with an AFM tip, have given rise to in-plane strain gradients of almost double the magnitude of those observed in the native state. A plausible explanation for the enhanced

conductivity observed in the stress-written phases (Figure 5.12) is therefore an interfacial strain-mediated effect arising from the increased strain gradients. It is possible that the increased interfacial strain causes a localised decrease in the bandgap [39, 40], leading to increased conduction similar to the Schottky effect.

5.4.2 Electronic structure of the stress-written mixed-phase

To gain more understanding into the atomic and electronic structure of the stress-written R' and T' phases, EELS was performed at the O-K and Fe-$L_{2,3}$ edges. During EELS acquisition the electron beam was scanned across the entirety of both native (Figure 5.20a) and stress-written (Figure 5.20b) regions ensuring that all possible FeO₆ environments were measured; the stress-written region is exactly that which is displayed in Figure 5.19b. The data was treated using principal component analysis (PCA), a well-established technique for reducing noise in EEL spectra [41]. The O-K edge of the native R and T phases (measured as the integral of spectra from the respective polymorphs) in Figure 5.20c can be divided into two regions, a pre-peak region from 530 – 537 eV and a post-edge peak from 538 – 548 eV which contain the expected native spectral features [13, 42]: the pre-peak spectral shape is similar for R and T, this peak has been identified as originating from the hybridisation between the O $2p$ and Fe $3d$ states. Here, at an energy resolution of 1.5eV, the subtle sub-peaks within the pre-peak have not been resolved, however, this does not pose any limitation to our analysis because the protruding differences between the O-K edge for the R and T phases are known to arise in the post-edge peak. Within the post-edge peak there are two sub-peaks at ~541.5 eV (labelled A) and ~543.5 eV (labelled B), these peaks
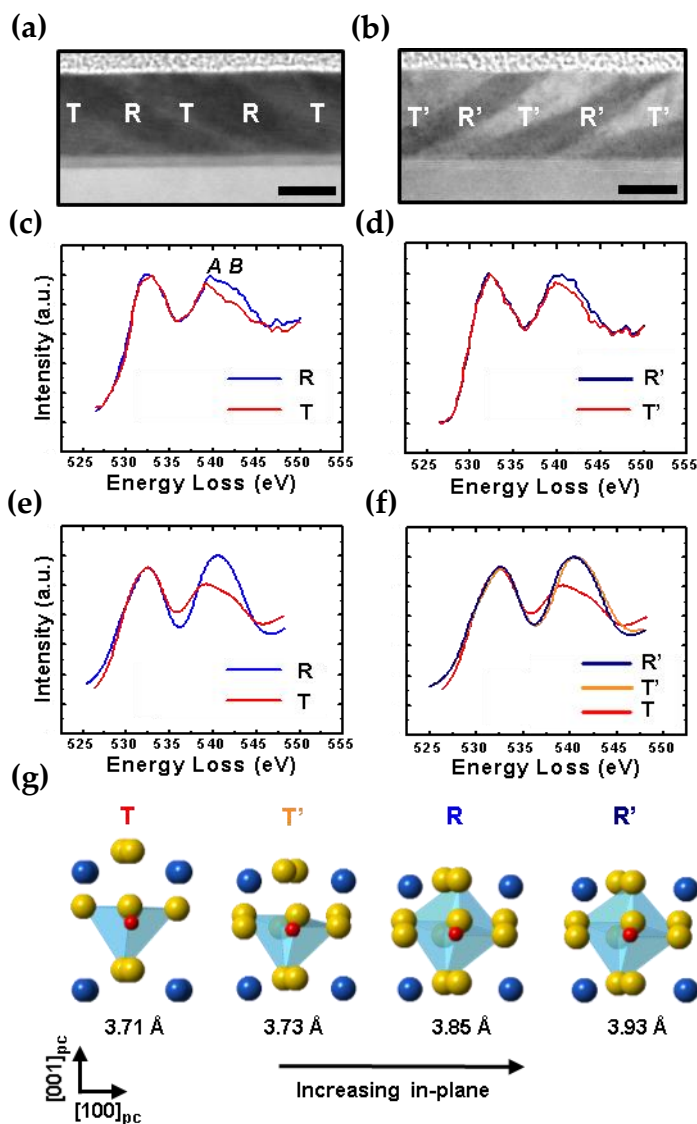
Figure 5.20: STEM-DF images of a native (a) and stress--written (b) region. O-*K* edge for the R and T phases within the native (c) and stress--written (d) regions, all spectra were normalised to the height of the pre-peak. FEFF calculated O-K edge for the corresponding R(R') and T(T') phases in the native (e) and stress-written (f) regions. Schematics of the BFO unit cells [15] used for the FEFF calculations (g) with in-plane lattice parameters labelled. Bi atoms are dark blue, Fe atoms are red and oxygen atoms are yellow in colour. Scale bars represent 25 nm.

originate from transitions of hybridised O *p*-Bi *p* orbitals. Considering that the native R and T phases have different Fe coordination (the R phase being octahedrally coordinated and the T phase having fivefold oxygen coordinated Fe), it is no surprise that the post-edge peak is different for the R and T phase. The native R phase shows evidence of both sub-peaks A and B whereas the native T phase shows only a sub-peak A.

The O-*K* edge for the stress-written R′ and T′ phases can be seen in Figure 5.20d. Again, the pre-peak looks similar for both R′ and T′ phases but the most striking variance, when comparing these to the O-*K* edge of the native spectra in Figure 5.20c, occurs in the post-edge peak. The post-edge peak for the stress-written R′ and T′ phases no longer has the same spectral differences that we saw in the native post-edge peak. Instead, the post-edge peak of the T′ phase looks strikingly similar to the post-edge peak of the R′ phase. To better understand the relation between possible changes in the crystal structure and the variation observed between the O-*K* edge of the native and stress-written spectra, a range of O-*K* edges were calculated using the program FEFF [43]. The BFO models used for the calculations are those modelled by A. Hatt and N. Spaldin [15], ranging in in-plane lattice parameter increments of 0.02Å from a highly-strained BFO unit cell (in-plane lattice parameter = 3.71 Å) to an extremely low strain unit cell (in-plane lattice parameter = 3.93 Å).

The calculated O-*K* edge for the native R and T phase are shown in Figure 5.20e, which qualitatively confirm the experimentally observed spectral features in Figure 5.20c. Figure 5.20f displays the calculated O-*K* edges which best match the experimentally observed stress-written R′ and T′ phases in Figure 5.20d. The

unit cell schematics corresponding to the BFO models used for the calculated R, T, R′ and T′ O-*K* edges are shown in Figure 5.20g. Observing the unit cell schematics, two things can be inferred: (i) the tetragonality of the unit cell decreases with increasing in-plane lattice parameter and (ii) the antiferrodistortive rotations of the FeO_6 octahedra around the $[001]_{pc}$ and $[011]_{pc}$ axes changes drastically as a function of in-plane lattice parameter: the $[001]_{pc}$ rotation which is not present at the native T phase (a = 3.71 Å) is present at the T′ phase (a = 3.73 Å), and the $[011]_{pc}$ rotation increases with in-plane lattice parameter [15]. Further analysis of the calculated spectra, indicate that the O-*K* edges for the R and R′ calculated phases have very little (if any) difference. Whereas, the T and T′ calculated phases (displayed in Figure 5.20f) show dramatically different post-edge peaks: the T′ post-edge peak (using the BFO model which is still highly-strained but with larger antiferrodistortive rotations of the FeO_6 octahedra, labelled T′ in Figure 5.20g) resembles more to that of the R′ post-edge peak, which in turn resembles the experimental T′ and R′ post-edge peaks.

It would appear that the application of localised stress to nucleate R′ polymorphs into the electrically poled T phase (creating R′ polymorphs with increased in-plane lattice parameter) has consequently altered the FeO_6 octahedra of the neighbouring T phase (termed T′ after stress). Note that this does not necessarily mean that the stress-written T′ phase has an increased in-plane lattice parameter (like the T′ model in Figure 5.20g); in fact the opposite was found to be true in the NBED data: the T′ phase in-plane lattice spacing was reduced by ~0.1 Å. However, the EELS calculations do point towards increased octahedra rotations around the $[001]_{pc}$ and $[011]_{pc}$ axes in the T′ phase.

To gain more insight into the position of the O columns in the stress-written region, BF-STEM images were acquired. Figure 5.21a shows a contrast coloured BF-STEM image acquired from within the stress-written region of Figure 5.20b. The R' phase is blue in colour while the T' phase is yellow/orange. A white dashed box encloses an R'/T' boundary, enlarged in Figure 5.21b, with the simultaneously acquired HAADF image in Figure 5.21c. The two smaller white dashed boxes (labelled 1 and 2) in Figure 5.21a enclose an enlarged BF-STEM image of the R' and T' phases, respectively, with the corresponding BFO unit cell schematics from Figure 5.20 overlaid. The oxygen column positions show good agreement to the Fe coordination given by the overlaid R' and T' models. Furthermore, a bright contrast can be seen along the R'/T' boundary in the BF image of Figure 5.21b, this type of contrast change is known to relate to areas which are highly strained and/or have some degree of mistilt; confirming the high strain-gradients observed previously by NBED at the R'/T' boundaries.

The Fe-$L_{2,3}$ edge was also investigated as it is well known that changes in the Fe L_3/L_2 ratio can be a signature of oxygen vacancies or valence change [42], which as previously mentioned are a common feature of highly strained interfaces [36, 44]. Figure 5.21d shows the Fe-$L_{2,3}$ edge extracted from the T' phase (labelled as probe position 1 in Figure 5.21c), the R' phase (probe position 7) and approximately the centre of the R'/T' boundary (probe position 4). The Fe-$L_{2,3}$ edge corresponds to excitations from the Fe 2p electrons ($2p^6 3d^5$) into empty Fe 3d states ($2p^5 3d^6$) giving the "white-lines" at 710 eV (L_3) and 723 eV (L_2). The L_3 and L_2 peaks show some variation in spectral features for the different phases, as can be seen in Figure 5.21d. These spectral changes are suggestive of the different Fe
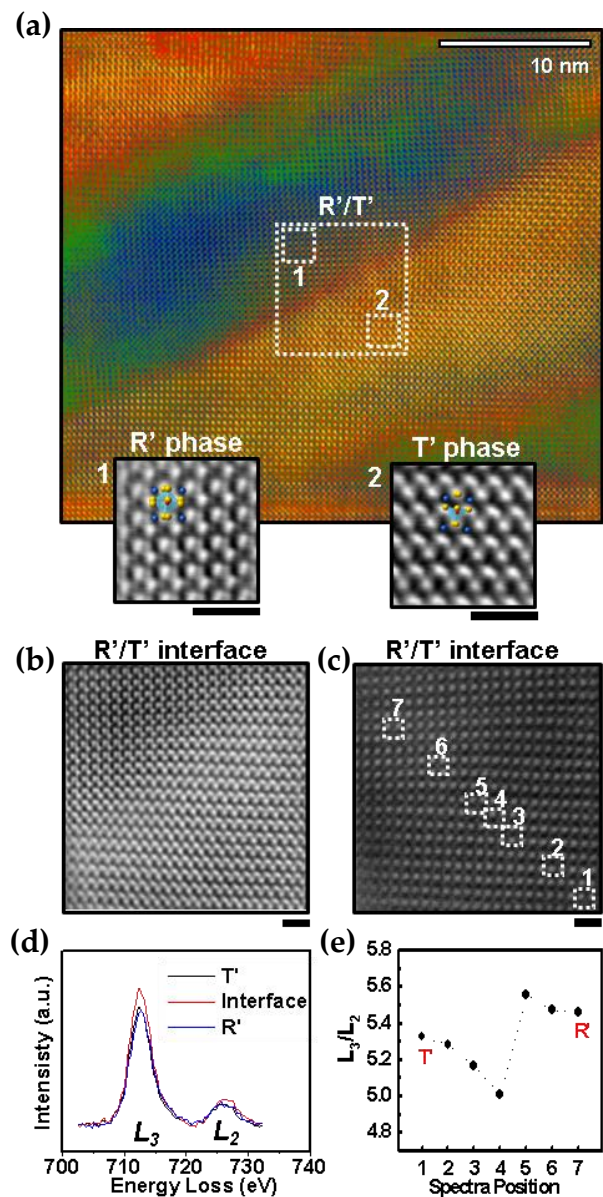
Figure 5.21: STEM-BF image of a stress-written region (a), including enlarged BF images extracted from the white dashed boxes showing the oxygen columns positions in the R′ and T′ phases, the corresponding BFO unit cells from Figure 5.20g have been overlaid. BF (b) and corresponding HAADF (c) images of the R′/T′ interface extracted from the large white dashed box in (a). Fe-$L_{2,3}$ edge extracted from the T′ phase (position 1 in (c)), the R′ phase (7 in (c)) and approximately the centre of the R′/T′ boundary (4 in (c)) in (d). L_3/L_2 ratio measured across the R′/T′ boundary (e), corresponding to the probe positions 1-7 in (c). Unmarked scale bars represent 1 nm.

coordination (the R′ phase being octahedrally coordinated and the T′ phase having fivefold oxygen coordinated Fe). In Figure 5.21e, the L_3/L_2 ratio is displayed for positions 1-7 in Figure 5.21c. A stepped continuum function under L_3 and L_2, using a double arctangent function, was used to accurately subtract the background and continuum to give an accurate estimate of the true L_3/L_2 ratio without the influence of multiple scattering effects [45]. The L_3/L_2 ratio trend shows a sharp drop at the R′/T′ boundary (lowest at probe position 4) which resembles previous reports of conducting R/T interfaces in Ca-doped BFO thin films [36] but has also been reported in (assumingly non-conducting) native R/T boundaries in mixed-phase BFO thin films [42]. The Fe-$L_{2,3}$ edge was also calculated using FEFF, however, the calculated L_2 intensity showed a higher intensity than experiment for all phases meaning that the L_3/L_2 ratio could not be accurately measured.

It is proposed based on the evidence at hand, that the Fe L_3/L_2 drop at the boundary may be purely due to the abrupt change in strain state between the T′ and R′ phases. At this stage, there is no solid evidence to prove or disapprove the existence of oxygen vacancies or a valence change at the R′/T′ boundaries. Further investigations at higher energy resolution will need to be carried out, however, this adds the complication of requiring a thinner specimen for EELS acquisition; which in turn generates the risk of altering the density and strain state of the BFO phases by relaxation of the thin film [44, 46]. Therefore, no longer resembling the initial configuration of the bulk.

5.5 Conclusion

In this chapter, the as-grown native BFO mixed-phase state was characterised using TEM/STEM techniques. Following this, the thermal activation phase transformation was explored through heat-cycling STEM experiments demonstrating a lateral growth of the highly-strained T phase above 400°C, although a fully reversible process was not observed. In a more controllable nature, via an AFM tip, a combinatorial approach demonstrated reversible switching of the native mixed-phase state to a pure T phase state by applying electric field, and back again to a mixed-phase state by the nucleation of R polymorphs using localised stress. Energy-based effective Hamiltonian simulations demonstrated phase competition under the application of electric-field and stress, directly comparable to experimental data. The stress-written phases were investigated via c-AFM which showed enhanced conductivity at the R′/T′ boundaries. Furthermore, a detailed TEM investigation of cross-sectional lamellae prepared from pre-written AFM regions revealed that the stress-written R′/T′ boundaries have higher in-plane strain gradients (due to alterations of the R′ and T′ unit cells) compared to the native R/T boundaries, rationalising the enhanced conductivity as a strain mediated effect. The control demonstrated by the application of external-stimuli to mixed-phase BFO, and the improved understanding of the phase morphology before and after external-stimuli application, serves as a motive to achieving broad implications for tuning mixed-phase BFO functional behaviour in a wider range of technologically notable applications. Beyond mixed-phase ferroelectrics, reversible control employing

electrical bias and nanoscale stress to create piezoresistive capacitor type devices looks promising.

5.6 References

[1] J. Wang, J. Neaton, H. Zheng, V. Nagarajan, S. Ogale, B. Liu, D. Viehland, V. Vaithyanathan, D. Schlom, U. Waghmare, N. Spaldin, K. Rabe, M. Wuttig, R. Ramesh, *Science.* **2003**, *299*(5613), 1719-1722.

[2] J. Li, J. Wang, M. Wuttig, R. Ramesh, N. Wang, B. Ruette, A. Pyatakov, A. Zvezdin, D. Viehland, *Appl. Phys. Lett.* **2004**, *84*(25), 5261-5263.

[3] S. Y. Yang, J. Seidel, S. J. Byrnes, P. Shafer, C. -. Yang, M. D. Rossell, P. Yu, Y. -. Chu, J. F. Scott, Ager,J.W.,III, L. W. Martin, R. Ramesh, *Nature Nanotechnology.* **2010**, *5*(2), 143-147.

[4] J. Seidel, L. W. Martin, Q. He, Q. Zhan, Y. -. Chu, A. Rother, M. E. Hawkridge, P. Maksymovych, P. Yu, M. Gajek, N. Balke, S. V. Kalinin, S. Gemming, F. Wang, G. Catalan, J. F. Scott, N. A. Spaldin, J. Orenstein, R. Ramesh, *Nature Materials.* **2009**, *8*(3), 229-234.

[5] R. J. Zeches, M. D. Rossell, J. X. Zhang, A. J. Hatt, Q. He, C. -. Yang, A. Kumar, C. H. Wang, A. Melville, C. Adamo, G. Sheng, Y. -. Chu, J. F. Ihlefeld, R. Erni, C. Ederer, V. Gopalan, L. Q. Chen, D. G. Schlom, N. A. Spaldin, L. W. Martin, R. Ramesh, *Science.* **2009**, *326*(5955), 977-980.

[6] R. K. Vasudevan, Y. Liu, J. Li, W. Liang, A. Kumar, S. Jesse, Y. Chen, Y. Chu, V. Nagarajan, S. V. Kalinin, *Nano Lett.* **2011**, *11*(8), 3346-3354.

[7] C. Beekman, W. Siemons, T. Z. Ward, M. Chi, J. Howe, M. D. Biegalski, N. Balke, P. Maksymovych, A. K. Farrar, J. B. Romero, P. Gao, X. Q. Pan, D. A. Tenne, H. M. Christen, *Adv Mater.* **2013**, *25*(39), 5561-+.

[8] Y. Heo, B. Jang, S. J. Kim, C. Yang, J. Seidel, *Adv Mater.* **2014**, *26*(45), 7568-7572.

[9] H. Lu, C. -. Bark, D. Esque de los Ojos, J. Alcala, C. B. Eom, G. Catalan, A. Gruverman, *Science.* **2012**, *336*(6077), 59-61.

[10] C. Michel, J. Moreau, W. James, *Acta Crystallographica Section B-Structural Crystallography and Crystal Chemistry.* **1971**, *B 27*(FEB15), 501-&.

[11] F. Kubel, H. Schmid, *Acta Crystallographica Section B-Structural Science.* **1990**, *46*, 698-702.

[12] V. Shelke, V. N. Harshan, S. Kotru, A. Gupta, *J. Appl. Phys.* **2009**, *106*(10), 104114.

[13] M. D. Rossell, R. Erni, M. P. Prange, J. -. Idrobo, W. Luo, R. J. Zeches, S. T. Pantelides, R. Ramesh, *Phys. Rev. Lett.* **2012**, *108*(4), 047601.

[14] J. Zhang, X. Ke, G. Gou, J. Seidel, B. Xiang, P. Yu, W. Liang, A. M. Minor, Y. Chu, G. Van Tendeloo, X. Ren, R. Ramesh, *Nature Communications.* **2013**, *4*, 2768.

[15] A. J. Hatt, N. A. Spaldin, C. Ederer, *Physical Review B.* **2010**, *81*(5), 054109.

[16] M. Arredondo, Q. M. Ramasse, M. Weyland, R. Mahjoub, I. Vrejoiu, D. Hesse, N. D. Browning, M. Alexe, P. Munroe, V. Nagarajan, *Adv Mater.* **2010**, *22*(22), 2430-+.

[17] Z. Chen, L. You, C. Huang, Y. Qi, J. Wang, T. Sritharan, L. Chen, *Appl. Phys. Lett.* **2010**, *96*(25), 252903.

[18] D. Sando, B. Xu, L. Bellaiche, V. Nagarajan, *Applied Physics Reviews.* **2016**, *3*(1), 011106.

[19] Y. Heo, B. Jang, S. J. Kim, C. Yang, J. Seidel, *Adv Mater.* **2014**, *26*(45), 7568-7572.

[20] S. Prosandeev, D. Wang, W. Ren, J. Iniguez, L. Bellaiche, *Advanced Functional Materials.* **2013**, *23*(2), 234-240.

[21] B. Dupe, I. C. Infante, G. Geneste, P. -. Janolin, M. Bibes, A. Barthelemy, S. Lisenkov, L. Bellaiche, S. Ravy, B. Dkhil, *Physical Review B.* **2010**, *81*(14), 144128.

[22] J. C. Wojdel, J. Iniguez, *Phys. Rev. Lett.* **2010**, *105*(3), 037208.

[23] W. Zhang, J. Ouyang, A. L. Roytburd, *Scr. Mater.* **2012**, *66*(7), 499-502.

[24] Z. Chen, S. Prosandeev, Z. L. Luo, W. Ren, Y. Qi, C. W. Huang, L. You, C. Gao, I. A. Kornev, T. Wu, J. Wang, P. Yang, T. Sritharan, L. Bellaiche, L. Chen, *Physical Review B.* **2011**, *84*(9), 094116.

[25] D. A. Porter, K. Easterling, *Phase Transformations in Metals and Alloys*, Taylor and Francis, London **2009**.

[26] W. Cao, L. Cross, *Physical Review B.* **1993**, *47*(9), 4825-4830.

[27] P. Arigur, L. Benguigui, *Journal of Physics D-Applied Physics.* **1975**, *8*(15), 1856-1862.

[28] J. Guyonnet, I. Gaponenko, S. Gariglio, P. Paruch, *Adv Mater.* **2011**, *23*(45), 5377-+.

[29] S. Farokhipoor, B. Noheda, *Phys. Rev. Lett.* **2011**, *107*(12), 127601.

[30] A. N. Morozovska, R. K. Vasudevan, P. Maksymovych, S. V. Kalinin, E. A. Eliseev, *Physical Review B.* **2012**, *86*(8).

[31] W. Wu, Y. Horibe, N. Lee, S. Cheong, J. R. Guest, *Phys. Rev. Lett.* **2012**, *108*(6), 077203.

[32] P. Maksymovych, J. Seidel, Y. H. Chu, P. Wu, A. P. Baddorf, L. Chen, S. V. Kalinin, R. Ramesh, *Nano Letters.* **2011**, *11*(5), 1906-1912.

[33] C. -. Yang, J. Seidel, S. Y. Kim, P. B. Rossen, P. Yu, M. Gajek, Y. H. Chu, L. W. Martin, M. B. Holcomb, Q. He, P. Maksymovych, N. Balke, S. V. Kalinin, A. P. Baddorf, S. R. Basu, M. L. Scullin, R. Ramesh, *Nature Materials.* **2009**, *8*(6), 485-493.

[34] G. Catalan, J. Seidel, R. Ramesh, J. F. Scott, *Reviews of Modern Physics.* **2012**, *84*(1), 119-156.

[35] K. Kim, B. Jang, Y. Heo, J. H. Lee, M. Jeong, J. Y. Lee, J. Seidel, C. Yang, *Npg Asia Materials.* **2014**, *6*, e81.

[36] J. Seidel, M. Trassin, Y. Zhang, P. Maksymovych, T. Uhlig, P. Milde, D. Koehler, A. P. Baddorf, S. V. Kalinin, L. M. Eng, X. Pan, R. Ramesh, *Adv Mater.* **2014**, *26*(25), 4376-4380.

[37] B. W. Veal, S. K. Kim, P. Zapol, H. Iddir, P. M. Baldo, J. A. Eastman, *Nature Communications.* **2016**, *7*, 11892.

[38] Q. Lv, S. Wu, J. Lu, M. Yang, P. Hu, S. Li, *J. Appl. Phys.* **2011**, *110*(10), 104511.

[39] S. Jain, M. Willander, V. Overstraeten, Eds, *Compound Semiconductors Strained Layers and Devices*, Vol. 7, Electronic Materials Series edn. Springer**2013**.

[40] A. Kolobov, J. Tominaga, *Two-Dimensional Transition-Metal Dichalcogenides*, Vol. 239, Springer Series in Materials Science edn. Springer**2016**.

[41] G. Lucas, P. Burdet, M. Cantoni, C. Hebert, *Micron.* **2013**, *52-53*, 49-56.

[42] P. S. S. R. Krishnan, J. A. Aguiar, Q. M. Ramasse, D. M. Kepaptsoglou, W. -. Liang, Y. -. Chu, N. D. Browning, P. Munroe, V. Nagarajan, *Journal of Materials Chemistry C.* **2015**, *3*(8), 1835-1845.

[43] J. J. Rehr, J. J. Kas, F. D. Vila, M. P. Prange, K. Jorissen, *Physical Chemistry Chemical Physics.* **2010**, *12*(21), 5503-5513.

[44] P. S. S. R. Krishnan, A. N. Morozovska, E. A. Eliseev, Q. M. Ramasse, D. Kepaptsoglou, W. Liang, Y. Chu, P. Munroe, V. Nagarajan, *J. Appl. Phys.* **2014**, *115*(5), 054103.

[45] P. van Aken, B. Liebscher, *Physics and Chemistry of Minerals.* **2002**, *29*(3), 188-200.

[46] R. Brydson, Ed, *Aberration-Corrected Analytical Transmission Electron Microscopy*, John Wiley & Sons, Ltd, U.K. **2011**.

6. Summary, conclusions and future work

In this chapter the research presented in this thesis is summarised and conclusions are presented. Additionally, ideas for future work are suggested.

6.1 Summary and conclusions

The aim of the research carried out in this thesis was to investigate domain dynamics as a function of applying different stimuli in one of the most used and studied ferroelectric materials, which is currently used for a variety of devices: polycrystalline $BaTiO_3$ ceramics, along with one of today's most promising and interesting ferroelectric materials for device applications: mixed-phase $BiFeO_3$ thin films. The investigations primarily used a variety of TEM techniques accompanied by relevant theory and AFM techniques.

For the study on the polycrystalline BaTiO₃ ceramic, the objective was to further understand the link between domains coupling across adjacent grains and to explore the domains' configuration (and re-ordering) as a function of applying external stimuli, such as heating through T_C. Specifically, two examples were explored in a static matter as first instance: the case of domains coupling across a single grain boundary, and the more complex case of the domain configuration within adjacent grains which meet around a junction (or pore), where FIB lamellae were fabricated. The analysis focuses on ferroelastic domains, mainly a-a type domains, where the theory of martensite crystallography demonstrated that in the case of domains sharing a single grain boundary, the domains on average arranged themselves in a compatible and stress-free manner. This study concluded that most likely the large dominant domain variant (named C) formed in one grain on cooling through T_C and a mixture of domain variants (A and B) formed in the neighbouring grain to accommodate the strain imposed by variant C. Since the new B domain variants mismatched the stretch of the C domain at the grain boundary, a small quantity of D domains needed to be formed to reduce stress, giving an overall elastically compatible arrangement.

For the study of adjacent grains arranged around a junction, a computational calculation was created, given the complexity of the case. The computational example demonstrated that the relaxation of the out-of-plane constraint gives rise to an undetermined set of linear equations which can be solved for compatible domain wall orientations and volume fractions of domains, indicating that groups of adjacent grains can form stress-free domain patterns. A good agreement was found between the experimental data and the solved fractional volume of domains by the computational model. It should be noted that

the discrepancies in domain wall orientations were rationalised as mainly due to the estimated Euler angles used in the calculation. Since the overall constraint in a polycrystalline lamella is much less than that of the bulk, re-configuration of the bulk domain structure during heating and cooling through T_C was hypothesised. STEM in-situ heating cycle experiments demonstrated that this was indeed the case; it was shown that the domain density increased (more than doubled) after the first heating-cycle through T_C and the presence of more intricate domain bundles increased when the temperature was cooled back to room temperature in a less continuous quench-like fashion. This type of domain density scaling is expected considering Kittel's law; however, the most interesting aspect of this study lies in observing the nucleation site of the domains (originating mostly at the grain boundary) on cooling through T_C, the change in favourable domain orientation (which changed from grain to grain) and the domain configuration changes (including bundle domains) throughout the heating cycles (where the temperature ramping seemed to make a difference).

The investigated $BaTiO_3$ ceramic was further explored with focus on the ceramic's functionality, that being a positive temperature coefficient of resistivity (PTCR) effect, related to the ferroelectric nature and chemical heterogeneity of the ceramic. The study began by using KPFM to show a direct visualisation of the resistive grain boundaries. Aberration-corrected STEM and EELS revealed new evidence of a grain boundary $PbTiO_3$-like region (spanning across ~ 10 - 15nm), in other words a Pb rich grain boundary, which was associated with an increased local polarisation in the domains adjacent to the grain boundaries. The chemical and electronic heterogeneity of the ceramic was linked to the changes in potential barrier at the grain boundary, theorised by the Heywang-Jonker model. It was

inferred that the confined PbTiO$_3$ rich grain boundary region would have a higher spontaneous polarisation (than BaTiO$_3$), thus reducing the grain boundary barrier potential further below T$_C$, and therefore augmenting electronic transport and enhancing the magnitude of resistivity jump at T$_C$, and so justifying the optimised PTCR effect exhibited by this commercially available ceramic.

The second part of the experimental work in this thesis focuses on the investigation of polymorph reversibility in BiFeO$_3$ thin films by application of external stimuli. The as-grown native BiFeO$_3$ mixed-phase state was first characterised using a variety of TEM/STEM techniques, identifying the polymorphs (corresponding to different phases) known as T and R. The highly-strained T phase and relaxed R phase were characterised, and the influence of thin film thickness on the ratio of T:R phases was explored, confirming that as the thin film thickness is increased, the density of the relaxed R phase (resembling bulk BiFeO$_3$) increases. Following this, the thermal activation phase transformation was investigated by the application of heat-cycling in the STEM experiments; demonstrating a significant lateral growth of the highly-strained T phase above 400°C, although a fully reversible process was not observed and higher temperatures could not be explored due to sample degradation. For a more controllable experiment an AFM tip was used in a combinatorial approach, which demonstrated reversible switching of the native mixed-phase state to a pure T phase state by applying electric field, and back again to a mixed-phase state by the nucleation of R domains using localised stress. Energy-based effective Hamiltonian simulations demonstrated phase competition under the application of electric field and stress, directly comparable to experimental data. The stress-written phases (R' and T') were investigated via c-AFM which showed enhanced

conductivity at the R′/T′ boundaries. Furthermore, detailed TEM investigation of cross-sectional lamellae prepared from pre-written AFM regions revealed that the newly stress-written R′ and T′ phases differ slightly in structure from the native phases and more importantly, the R′/T′ boundaries have higher in-plane strain gradients (due to alterations of the R′ and T′ unit cells, primarily the R′ unit cells having a reduced c/a ratio) compared to the native R/T boundaries, rationalising the enhanced conductivity as a strain mediated effect.

6.2 Future work

The work presented in Chapter 3 of this thesis, investigating domains in polycrystalline BaTiO$_3$, involved the understanding of domain compatibility across grain boundaries and the reorganisation of domains as a function of heat-cycling through T$_C$. It would be of interest to expand these experiments to a wider set of lamellae involving different neighbouring grain rotations and different heating/cooling rate cycles. For a more comprehensive study, work should be directed to gain complete knowledge of the Euler angles between neighbouring grains in order to achieve a more accurate solution in the computational compatibility calculation. Furthermore, given the chemical heterogeneity of the studied PTCR ceramic, and considering the role that this could have in the local polarisation and domain pattern, future work should include a study on pure BaTiO$_3$, for comparison purposes. It would be important to discern between a more general phenomenon caused by elastic conditions and the effect caused by the presence of segregates such as PbTiO$_3$. Work has already been started to
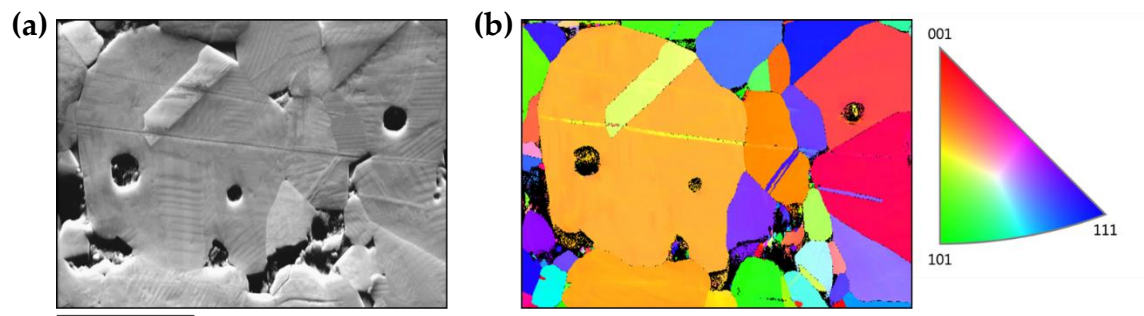
Figure 6.1: SEM image of a polycrystalline pure BaTiO₃ ceramic (a) and corresponding EBSD map (b) showing the out-of-plane grain orientation in the form of a colour map with the main zone axes corresponding to the most extreme colours (red, green and blue). Scale bar represents 10 μm.

investigate a pure BaTiO₃ ceramic and plans have been made to carry out further investigations at the University of Manchester in the coming months. Figure 6.1 shows an EBSD map where lamella with known grain orientations will be cut from.

The work presented in Chapter 4, chemical analysis of the grain boundary region, could be further improved by attempting to map the local polarisation across the grain boundary. This would involve using specialised techniques such as negative spherical aberration (NCSI), which requires an extremely thin lamella (~10 nm thick) cut from a suitable orientation ([100] or [010] zone axis). This is however, not a trivial task considering how difficult FIBing moderate thickness lamella from a polycrystalline sample can be, due to grain boundary preferential milling; and the intrinsic disordered nature of the grain boundaries.

The final experimental chapter focused on polymorph reversibility in mixed-phase BiFeO₃ thin films. It was shown that the highly-strained T phase

grew by the application of heat, however, a fully reversible transition between the mixed-phase and polar T state was not observed. Since full reversibility has only been reported previously (mostly using AFM) for specific thin film thickness, and hence T:R ratio, potential future work would be to investigate a range of different thin film thicknesses using in-situ TEM to determine how the initial T:R ratio affects the thin film's ability to switch as a function of heating; while simultaneously characterising the strain and possible structural changes in the phases. Similarly, since it was demonstrated that mixed-phase $BiFeO_3$ thin films can be reversibly switched between a mixed-phase state and a polar T state using electric field and localised stress via AFM; it would be of interest to repeat these experiments using the recently available in-situ TEM biasing holder and an in-situ TEM nano-indenter holder to avail of live imaging and characterisation of the $BiFeO_3$ phases whilst applying the respective external stimuli. An in-situ TEM experiment using a nano-indenter to apply localised stress was attempted, however, due to time constraints and some initial difficulties involved with this new technique, the right configuration for the experiment has yet to be explored.